Understanding Subsurface Void Formation and Detection during Friction Stir Welding of Aluminum Alloys

By

Daniel J. Franke

A dissertation submitted in partial fulfillment
of the requirements for the degree of

Doctor of Philosophy
(Mechanical Engineering)

at the
UNIVERSITY OF WISCONSIN – MADISON
2021

Date of final oral examination: 8/19/2021

The dissertation is approved by the following members of the Final Oral Committee:

Frank Pfefferkorn, Professor, Mechanical Engineering
Michael Zinn, Associate Professor, Mechanical Engineering
Shiva Rudraraju, Assistant Professor, Mechanical Engineering
Melih Eriten, Associate Professor, Mechanical Engineering
Kumar Sridharan, Professor, Engineering Physics

ACKNOWLEDGEMENTS

Prof. Frank E. Pfefferkorn

Prof. Michael Zinn

Prof. Shiva Rudraraju

Prof. Melih Eriten

Prof. Kumar Sridharan

Dr. Kamel Fezzaa

LAMSML Lab Members

Family and Friends

National Science Foundation Grant 1826104

US Department of Energy

University of Wisconsin Madison Department of Mechanical Engineering

Table of Contents

List of Tables

List of Figures

Nomenclature

FSW	=	Friction Stir Welding
AS	=	Advancing Side
RS	=	Retreating Side
APR	=	Advance Per Revolution
APS	=	Advanced Photon Source
m	=	Effective mass of the system
b	=	Damping coefficient
k	=	Stiffness of the system
F	=	Force applied to the system
k_{eq}	=	The equivalent combined stiffness of two springs in series
k_1	=	Stiffness of the toolholder
k_2	=	Stiffness of the machine spindle
f	=	Natural frequency of the system

Abstract

The formation of subsurface voids during friction stir welding has limited process adoption in high-reliability applications and high-volume production. Process adoption can be increased by developing robust methods of in-process void monitoring, as well as designing the process for higher travel speeds while avoiding void formation. A fundamental physical understanding of how sub-surface voids form during friction stir welding of aluminum alloys must be developed in order to advance the state of the art in these two areas. The objective of this work is to develop said fundamental physical understanding of how voids form, as well as how they alter process interaction forces and subsequent tool motions during void interaction. This fundamental understanding will form the basis for more robust methods of defect monitoring that are transferable across changes in process parameters and will help drive more accurate numerical simulation of the sub-surface defect formation process.

An advanced experimental setup allowed for the synchronization of the tool-workpiece interaction forces with the angular position of features on the tool probe such as the flats and the most eccentric point of the tool due to its natural runout. This led to the observation that it is the geometric imperfections (tool runout and shoulder levelness with respect to rotational axis) that drive the oscillatory forces at the tool rotational frequency in friction stir welding. During void formation, there are two distant interactions between two of the peaks on the tool probe and the void volume that create a momentary reduction in the oscillatory forces due to the lack of contact between the probe features and the workpiece material. The distortions in the force signals were enhanced by isolating the probe runout as the major driving feature by eliminating the unlevel nature of the tool shoulder with respect to the rotational axis. This led to a more direct relationship between the amplitude at the third harmonic in the force signals and the size of voids in the weld. It was found that a void will remain in the weld once the amplitude of the third harmonic exceeds 30% of the amplitude at the rotational frequency in a full-contact condition. Additionally, the

amplitude at the third harmonic will saturate at 70% the full contact amplitude since the third harmonic is generated by a reduction in contact pressure. These results show that even a small amount of tool runout must be considered when developing a force transient based void monitoring method.

Tool motion measurements during welding were captured via a laser vibrometer in order to complement the observations from the force measurements. It was determined that the eccentric motion of the tool is constrained during welding, which supports the observation that the eccentric motion of the tool applies the oscillatory force because the equal and opposite reaction force will constrain the tool. Additionally, it was observed that the tool momentarily deflects into void volumes during feature interaction. This deflection generates an amplitude at the third harmonic in the motion signal that matches the third harmonic in the force signal. This suggests that an accelerometer instrumented toolholder holds the potential to be used in a void monitoring method. In order to develop a physical understanding of the tool motion during void interaction, a simple mass-spring-damper model was used to describe the motion of the tool side of the system. Good agreement between the modeled and experimentally measured tool acceleration at three times the tool rotational frequency was shown. The modeling led to the observation that the dynamics of the system at three times the tool rotational frequency are driven by the stiffness of the system and that the stiffness is driven by the stiffness of the toolholder itself. Damping does not appear to be relevant because the frequency of interest is significantly lower than the natural frequencies of the systems studied. Also, the effective mass of the system is too small to play a role. This understanding will expedite the development of the accelerometer instrumented toolholder based void monitoring method that is currently under investigation. Additionally, substantial progress has been made towards developing the capabilities of capturing in situ void imaging using the high-speed X-ray beamline at Argonne National Laboratory’s Advanced Photon Source.

Chapter 1: Introduction

The friction stir welding (FSW) process (Figure 1) consists of plunging a rotating non-consumable tool into two metallic workpieces and traversing the tool along a joint line in order to mechanically intermix the two workpieces [1]. The plastic deformation of the workpieces generates heat which produces temperatures on the order of 80-95% of the solidus temperature of the alloy. The elevated temperature is instrumental in facilitating plastic deformation of the workpieces but with the key aspect that the process does not melt the material. The solid-state nature of the process provides distinct advantages over fusion-based welding processes. These advantages include a less severe heat affected zone, minimal distortion and residual stresses, avoidance of hot cracking, reduction/elimination of shielding gas, energy efficiency, and grain refinement within the stir zone due to dynamic recrystallization. A significant amount of research has shown that FSW can be used as an energy efficient method of creating high-quality joints in lightweight alloys such as aluminum and magnesium [2, 3].

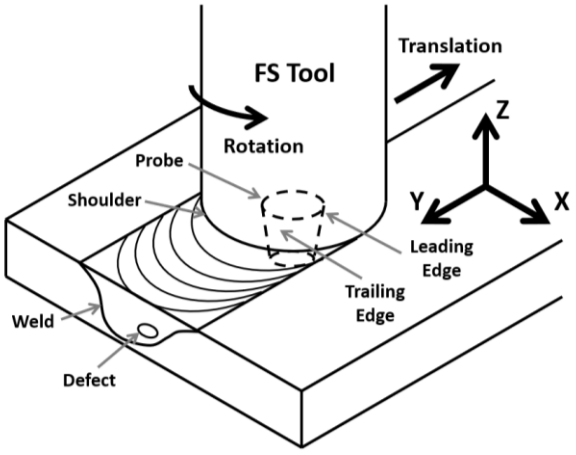

Figure 1: Schematic of friction stir welding process defining 3-axis coordinate system

However, specific limitations have hindered process adoption in certain applications. These limitations include the need for updated design of components for friction stir welding, lack of standardization, more robust fixturing, and higher capital costs of equipment. Currently, the process is limited in terms of travel speed, which has hindered its adoption in high volume

production settings. An increase in travel speed is more likely to result in an inadequate thermomechanical state which prevents the material from successfully deforming around the tool probe to be deposited in the weld. The breakdown in material flow results in volumetric voids within the weld which are detrimental to joint performance. Voids tends to form in the probe driven region of the weld resulting in sub-surface defects which cannot be detected visually and therefore require a post-process non-destructive evaluation technique (*e.g.* ultrasonic testing [4, 5], eddy current testing [6, 7]) to determine if the weld is compromised. In many cases, the additional step of applying a post process non-destructive evaluation technique is cost prohibitive. Development of a robust *in situ* void detection method based on a measured process output has the potential to address this limitation. Additionally, real time detection will provide the opportunity for in-process corrective action, which can prevent a part form being scrapped. The goal of this work is to both further the fundamental understanding of how sub-surface voids are formed as well as advance the development of process measurement-based void detection methods and process design for void avoidance.

1.1 Intermittent Flow of Material during Friction Stir Welding

One of the more prominent features observed in the microstructure of most friction stir welds is the layers (or bands) of material that form in the cross sections of welds in the plane of welding (X-Y plane in Figure 1). The banded features that form at the distance that the tool advances in one revolution (Figure 2), are resultant of material flow around the tool probe in an intermittent manner per revolution. The mechanisms driving this intermittent flow are not completely understood. Researchers have proposed that it stems from a change in contact condition (sticking vs. sliding) between the material and the tool [8, 9]. Abergast [10] initiated a hypothesis, which was later articulated by Boldsaikhan *et al.* [11], involving the opening and filling of a cavity once per revolution in the wake of the tool probe. Nunes [12] proposed that strain localization propagates a batch-wise flow of material around the tool similar to the shear banding

process observed in machining chips. Fonda *et al.* [13], measured a change in shear textures within a single band which led the researchers to propose that the banded nature comes from an oscillatory motion (precession) of the tool due to the natural eccentricity (*i.e.,* tool runout) as well as an oscillatory deflection of the tool due to the oscillation in process forces during friction stir welding. Gratecap *et al.* [14], tested tools with different levels of eccentricity (runout) and showed that tools with larger runout moved more material around the tool per revolution, leading the researchers to propose that the banded structure stems primarily from tool runout. Reynolds [15] proposed that even small amounts of tool runout can create differences in strain rates from one side of the tool to the other (most eccentric side to least eccentric side). The difference in strain rates can then produce the difference in the microstructure seen once per revolution. Chen *et al.* [16], have proposed that each band is formed by the threads on a threaded tool probe, *i.e.*, within one revolution each thread groove creates a layer of material that is deposited in the wake of the tool. It is also possible that the banded structure is formed through a combination of several of the previously listed hypothesis, *i.e.*, tool runout could initiate strain localization and/or an opening and closing of a cavity in the wake of the tool probe. A fundamental understanding of the intermittent nature of material flow is important because significant research has shown that breakdown in intermittent flow around the probe is what causes sub-surface voids [11, 17, and 18].

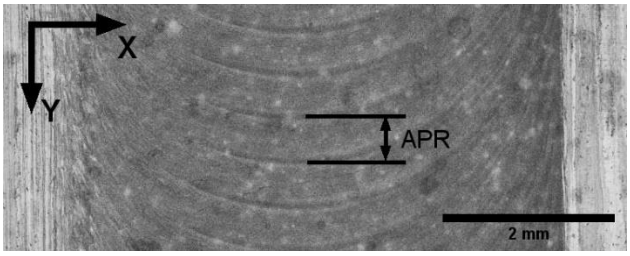

Figure 2: Microstructure resultant of intermittent flow once per tool revolution

1.2 Oscillatory Component of Process Forces

Significant research has shown that the process forces during friction stir welding tend to oscillate at the tool rotational frequency [11, 15-25, 33, 34]. Since the intermittent flow of material occurs once per tool revolution, and the process forces oscillate once per tool revolution, researchers have concluded that the two are fundamentally linked [11, 15-18, 22, 23, 33, 34]. Either the intermittent movement of material initiates the application of the oscillatory component of the force onto the tool, or the eccentric motion of the tool initiates the application of the force onto the material. Boldsaikhan *et al.* [23], developed a two-dimensional model that involved a prevailing pressure field due to the translation of the tool and a revolving pressure field due to the intermittent shear layer. The simulation of these two pressure fields produced similar force components compared to the average and oscillating components of the force signals that were captured during actual welding. This model was based on the concept that the formation of the shear layer initiates the force onto the tool. Other researchers have suggested that the eccentric nature of the tool (*i.e.*, runout) initiates the oscillatory component of the forces [15, 22, 24, 25]. Zaeh *et al.* [24], have shown that for two different tool setups with different amounts of runout, the greater runout results in a significantly larger amplitude of the oscillating component of the forces. In addition, both Zaeh *et al.* [24], and Panzer *et al.* [25], have proposed that the oscillating components of the process forces are affected by the complex dynamics of the machine and that modeling the whole machine/process system is critical to the modeling of the process forces.

1.3 Void Monitoring Literature Review

Assuming that the oscillatory nature of the process forces is directly related to the flow of material around the friction stir tool probe, then a breakdown in the material flow should produce a change in the measured forces. If a change in force can be captured while welding and correlated to the presence of volumetric voids within the weld, then the need for post-weld inspection can be reduced/eliminated. A growing number of studies have focused on the

development of online defect monitoring techniques due to the potential for elimination of post process inspection as well as in-process corrective action. Mishra et al. [26] have prepared a review on sensor-based monitoring and control of the friction stir welding process. A range of signals have been examined as part of the development of defect monitoring methods. These signals include force, torque, electrical current, temperature, vibration, and acoustic emission [26]. Most prior studies use a form of frequency analysis in combination with a machine learning algorithm to correlate changes in measured outputs to the presence of defects. In the scientific literature, this has only been performed in experimental settings with a very specific combination of a tool geometry, workpiece material, parameter space, and welding machine. Additionally, there is a lack of significant discussion on the physical understanding of what is occurring within the measured output. It has been hypothesized that the limited nature of the algorithm development will present challenges in accurately sensing void formation when any process setting, e.g., tool geometry or workpiece material, is altered. Therefore, there exists a potential to build a more robust and transferable method of void monitoring through the development of a fundamental physical explanation of what is producing changes in measured process signals.

Within the literature concerning void monitoring in friction stir welding, a large portion of the studies focus on the utilization of force and torque measurements due to their high sensitivity to the changes in stresses and pressures associated with the severe plastic deformation characteristic of the friction stir welding process. More specifically, a force-based measurement is the most directly related to the change in pressure at the interface between the tool and void during interaction and is not subject to the transient nature of thermal measurements. This had led researchers to propose that force and torque measurements are best suited for void monitoring [26]. Since a change in force will produce an acceleration, accelerometers also hold potential for capturing interactions between friction stir tools and defects. Accelerometers are attractive for this application due to their low cost and ease of implementation.

1.3.1 Force and Torque based Void Monitoring

In terms of force and torque-based methods, Jene *et al.* [27], examined the frequency content of welding forces using a short time Fourier transform and observed a distinct change in the frequency content of the force signals during defective regions of the weld. Fleming *et al.* [28], investigated methods for implementing in-process fault avoidance due to workpiece gaps in robotic FSW. Through frequency analysis of the axial force signal, the authors showed that statistical methods can be used as a pre-step to derive representations of force data that provide insight into the state of the weld. Ramulu *et al.* [29], analyzed the effect of welding speed, rotation speed, plunge depth, and shoulder diameter on the formation of sub-surface defects during FSW. A criterion was developed for predicting the onset of defect formation by examining the changes in axial force and torque as a function of welding parameters. Kumar *et al.* [30], examined defect detection of the friction stir welding process by using a discrete wavelet transform of force and torque signals. Their work showed that defect formation produced sudden changes in the force signals which were best captured using the discrete wavelet transformation and a square of errors statistical tool. Kumari *et al.* [31], applied a continuous wavelet transformation on the measured axial force and a statistical feature using the variance of scale 1 to localize defects in friction stir welds. They suggested that a continuous wavelet transform can provide better resolution than a discrete wavelet transform when it comes to defect localization. Das *et al.* [32], used a combined wavelet packet and Hilbert-Huang transform to correlate measured axial loads to the formation of defects. They showed that the axial load has distinct undulations at frequencies lower than the tool rotational frequency due to a breakdown in material flow. Boldsaikhan *et al.* [33], utilize a multilayer neural network and discrete Fourier transform to correlate changes in the frequency content in the feedback forces and wormhole defect occurrence. They observed an increase in the amplitude of the signals at frequencies both lower than and higher than the tool rotational frequency. However, a physical description of what is occurring at those frequencies was not presented. In general, one of the major limitations of prior studies is that they do not provide

explanations as to what is physically occurring that produces the changes in process forces when defects are forming. They often apply a “black box” approach of correlating inputs (feedback forces/torques) to outputs (defect occurrence). This limits the method when altering the process inputs because it is difficult to know when and how a “black box” correlation approach will translate. It is not even known if a method that was developed based on data from 6061-T6 aluminum welds can be applied to a different aluminum alloy. A fundamental understanding of what is physically occurring is crucial to developing a robust method that can be generalized and applied more broadly without limiting it to a specific machine, tool, weld configuration, workpiece alloy, and parameter space combination.

The current work is an expansion on the work by Shrivastava *et al.* [18, 34], in which evidence was shown that voids created with tools consisting of various numbers of flats on the tool probe can distort the oscillating component of the force signal. The distortion generates an amplitude at the frequency equal to the tool rotational frequency multiplied by the number of flats (harmonics of rotational frequency). In [18], the researchers used a tool with a three flat probe and quantified the amplitude of the force signal at the third harmonic of the tool rotational frequency using a discrete Fourier transform. The amplitude of the third harmonic was used to develop a correlation between the process forces and the volume of voids within welds measured through X-ray imaging. The physical explanation of the force oscillation at the tool rotational frequency is described as a cavity opening and filling in the wake of the tool. The explanation of the third harmonic is stated as an interaction between the flats on the tool probe and the voided region. However, a detailed physical description of said interaction is not provided. One focus of the current work is to provide a fundamental explanation of what is physically occurring in terms of the interaction between the tool and workpiece at both the tool rotational frequency and at the third harmonic. This fundamental understanding is critical when expanding the method to different tool geometries, fiction stir welding machines, and workpiece alloys.

1.3.2 Accelerometer based Void Monitoring

It has been hypothesized that an accelerometer inseminated toolholder holds potential to serve as the hardware for a void monitoring method since the distinct changes in process forces should lead to accelerations during the void interaction process. Therefore, another objective of the research is to advance the knowledge that forms the basis of utilizing an accelerometer-based measurement for sub-surface void monitoring. Several prior researchers have utilized accelerometer measurements in void monitoring schemes. Rabi et al. [35] developed a method of sensing void formation during friction stir welding by attaching an accelerometer to the workpieces fixture. The researchers developed a signal processing scheme to extract features from the accelerometer signal corresponding to void formation. It was determined void formation generates disturbances in the signal that can be extracted as frequencies near to and lower than the tool rotational frequency. A fundamental physical understanding of what was occurring at these low frequencies was not presented. Hartl et al. [36] also utilized an accelerometer fixed to the workpiece in combination with force and temperature measurements to develop a process monitoring method. The objective of the work was to examine if convolutional neural network is a superior to a Fourier convolutional network or recurrent neural network for defect predicting in friction stir welding. One important conclusion from the work was that the force measurements produce higher classification accuracy when used as the input as compared to using vibration or temperature as the input. Additionally, it was determined that the classification accuracy plateaued once the sampling rate of the measurements exceeded 600 Hz. This suggests that the frequencies of interest were relatively low (less than 600 Hz). The frequencies of interest were not discussed because a physical description of what occurs within the measured signals was not provided.

1.4 Objective

The overall objective of this body of work is to develop fundamental knowledge of how sub-surface voids form during friction stir welding of aluminum alloys. This fundamental knowledge will be developed through novel methods of measuring process forces, measuring FS tool motion during welding, and capturing real-time X-ray images of the defect formation process. This body of works seeks to explain what occurs at the frequency of the tool rotational rate that generates the oscillations in process forces, as well as what occurs during process force distortions during void interaction. Additionally, this body of work seeks to explain the nature of the microscale motions of the friction stir welding tool during welding and void interaction and how they relate to the process forces. Lastly, a significant effort has been put towards developing the process of real-time imaging of the subsurface void formation process within aluminum alloys in order to physically observe the void formation process. The fundamental knowledge gained will be moved toward application through two avenues. First, it will be used to develop more robust and transferable methods of void detection, which will help address the issue of costly post weld inspection and will allow for in process corrective action. Second, the fundamental knowledge will drive numerical simulation of the defect formation process that will help advance process design for void avoidance. This will help address the process speed limitations that have prevented the friction stir welding process from being adopted in high volume production. Advances in these two areas will lead to increased process adoption, which may benefit various manufacturing sectors of the United Sates economy.

Chapter 2: Understanding Process Force Transients

The fundamental basis of the force-based defect detection method is rooted in the hypothesis that the oscillatory process forces are linked to the intermittent flow of material around the tool probe, and that a breakdown in material alters the force oscillation. Therefore, the development of a robust method requires a fundamental understanding of the mechanisms driving the force oscillations. It was hypothesized that the geometric imperfections (slant and runout) in the friction stir tool depicted in Figure 3 drive the oscillation. This was examined by performing welds with several tools that were nominally the same (all manufactured by Friction Stir Link Inc. with three flats and a threaded tapered probe) but had differences in the shoulder slant and tool runout due to variations during manufacturing. The variations (reported in Table 1) were measured by rotating the tools freely in the machine spindle while measuring runout and slant with a dial indicator. The in-depth examination of force transients contained in this chapter was enabled through a novel experimental setup that was developed by previous researchers at UW-Madison. The setup consisted of a force dynamometer below the workpiece that measured the process forces within the same timing scheme as a magnetic angular encoder mounted to the tool spindle which measured the angular position of the friction stir tool. This provided the ability to resolve the force that the tool applies to the workpiece at a given point in time with the angular position of features on the FS tool (*e.g.* flats on tool probe, most eccentric point of the tool).

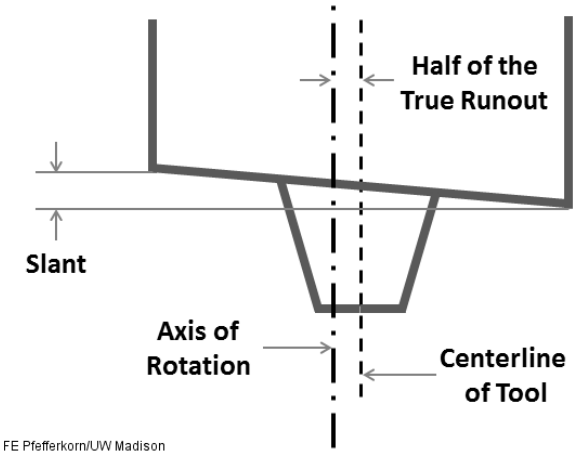

Figure 3: Depiction of the two primary tool imperfections studied

Table 1: Values of kinematic tool runout and shoulder slant measured via a dial indicator

	Tool 1	Tool 2	Tool 3
Runout	46 μm (0.0018 in)	74 μm (0.0029 in)	183 μm (0.0072 in)
Slant	10 μm (0.0004 in)	5 μm (0.0002 in)	15 μm (0.0006 in)

2.1 Methods

2.1.1: Experimental Apparatus

Friction stir welding was performed on a 3-Axis CNC Mill (HAAS, TM-1). A magnetic angular encoder (HAAS, Part #: 30-30390, 1024 pulses per revolution) mounted on the top of the spindle was used to measure the angular position of the friction stir tool during welding. Differential signals from the magnetic encoder were fed to an optical isolator (AutomationDirect, FC-ISO-C) for noise rejection. The optical isolator serves to isolate the electrical grounds between the data acquisition system and the CNC mill, as well as convert the differential encoder signals to single ended signals. Workpieces were mounted on a three-axis piezoelectric force dynamometer (Kistler, model 9265). Charge signals from the dynamometer were fed to charge amplifiers. Outputs from the optical isolator and charge amplifiers were connected to the data acquisition system (National Instruments, BNC-2090A, PCI-6014, PCIe-6320). The system provided the ability to measure the net forces that the friction stir tool applies

to the workpiece (in the X, Y, and Z directions in Figure 1) in conjunction with the angular position of the friction stir tool. This provided the capability of resolving the angular position of features on the tool (e.g., flats, eccentric points) at a given point in time with measured force values. The data acquisition system was triggered to sample the force signals at every pulse of the encoder, which produces 1024 data points per revolution. A full schematic of the data acquisition system can be found in the Appendices.

2.1.2: Experimental Procedure

All welds were performed as bead-on-plate welds in aluminum 6061-T6 workpieces that were 203 mm (8 inches) long, 102 mm (4 inches) wide and 6.35 mm (0.25 inches) thick. All welds were performed at a length of 150 mm, at a 3-degree travel angle, and with a backing plate made of 6.35 mm thick mild steel. To set the reference point for the tool plunge depth, a preload of 20 N was applied to a precision ground gage block placed at the trailing edge of the tool shoulder. All welds were performed with a commanded shoulder plunge depth of 0.2 mm at the center of the tool. However, the machine compliance in the axial (Z) direction (approximately 0.05 mm/kN) results in the center of the tool shoulder residing at approximately the top surface of the workpiece during welding. Prior to starting the data acquisition system, a reference point for the tool's angular position data was set by positioning one of the tool probe flats against the front face of the workpiece fixture (perpendicular to the weld direction).

To examine the effect tool runout and slant on the oscillatory component of the process forces, welds were first performed with the tools in their baseline state as described in Table 1. Two welds were performed for each tool at 1,000 rpm and 200 mm/min. Subsequently, the slant in the tool shoulder with respect to the true rotational axis of the tool was eliminated by fixing a turning tool to the table of the CNC mill used for friction stir welding, and turning the shoulders of each of the tools to make them level with respect to the true rotational axis of the tool as it spins in the milling machine spindle. The slant in all tools after machining was less than

the resolution of the dial indicator (2.5 μm), leaving only a significant runout of the tools. After leveling the tool shoulder with the rotational axis of the tool, the same welds were performed at 1,000 rpm and 200 mm/min with two replications for each tool. Post welding, a discrete Fourier transform was used to extract the amplitude of the oscillating component of the force signals in the X and Y directions over a period of 20 tool rotations once a steady-state condition, in terms of process forces, had been reached (100 mm into the weld length).

To examine the effect of tool runout on defect formation and force-based defect detection, welds were performed at increasing amounts of advance per revolution (APR) in order to create welds without defects (low advance per revolution) and welds with defects (high advance per revolution). Welds were performed at three rotational rates: 800, 1,000, and 1,200 rpm. The travel speed was then set to produce welds with advance per revolutions ranging from 0.3 to 0.8 mm/rev for each spindle speed. The full range of welding parameters that each individual tool was tested at is shown in Table 2. For Tool 3 (183 μm runout), the highest three advance per revolution conditions were not performed since this particular tool started to form defects at lower travel speeds than Tools 1 and 2. A total of 54 welds were performed.

Table 2: Parameters used to create defective and non-defective welds for all three tools

APR	800 rpm	1,000 rpm	1,200 rpm
0.3 mm	240 mm/min	300 mm/min	360 mm/min
0.4 mm	320 mm/min	400 mm/min	480 mm/min
0.5 mm	400 mm/min	500 mm/min	600 mm/min
0.6 mm	480 mm/min	600 mm/min	720 mm/min
0.7 mm	560 mm/min	700 mm/min	840 mm/min
0.75 mm	600 mm/min	750 mm/min	900 mm/min
0.8 mm	640 mm/min	800 mm/min	960 mm/min

Post welding, three cross sections (each 15 mm apart) were cut from each weld (in the X-Z plane in Figure 1) at a distance approximately halfway along the weld to ensure the weld had reached a steady state condition in terms of process forces. All cross sections were mounted, ground, and polished in order to expose the presence of sub-surface defects. Images of all defects were capture using white light optical microscopy (Alicona Infinite Focus). The

areas of the defects within each cross section were determined using an image analysis method developed in Mathworks MATLAB. The images were converted to black and white, where the aluminum becomes white (pixel values close to 255), and the defects become black (pixel values less than 100). A threshold value of 250 was set for segmenting all images. The images were then cleaned so that all artifacts smaller than 5 pixels in diameter are converted to the surrounding medium. An example of the segmentation process along with a sample histogram of the image is contained in the Appendices. The number of defect pixels was then counted and converted to an area value using the number of pixels in the scale bar outputted from the microscope software.

2.2 Explanation of Oscillatory Process Forces

The oscillation in process forces was examined by comparing the direction of the resultant process force in the plane of welding (X-Y plane) in relation to the angular position of features on the FS tool (enabled through the encoder data). The focus of this analysis to isolate the direction of the oscillating part of the process forces, *i.e.*, the parts of the force signals that rotate with the tool. Figure 4 illustrates the progression of deriving the direction of the resultant force from the measured X and Y force signals. The compass plots shown in this section are the result of taking the measured forces signals in the X and Y directions, eliminating the average components of the force signal, and then combining the normalized X and Y components for a singular point in time to form a resultant force in the X-Y plane. The arrow in the compass plot shows the direction and amplitude of the oscillatory component of the force that the tool is applying to the workpiece material. The tool will typically apply an average force to the workpiece in the direction of travel and toward the advancing side of the weld, which are due to the travel of the tool and shearing of colder material in front of the tool. Both average forces are removed from the force depicted in the compass plots in order to isolate the direction of the oscillatory component itself. The angular position of the features on tool probe at the given time when the resultant force is calculated can

be overlaid on the compass plot since the angular encoder pulses were used to trigger the force measurements.

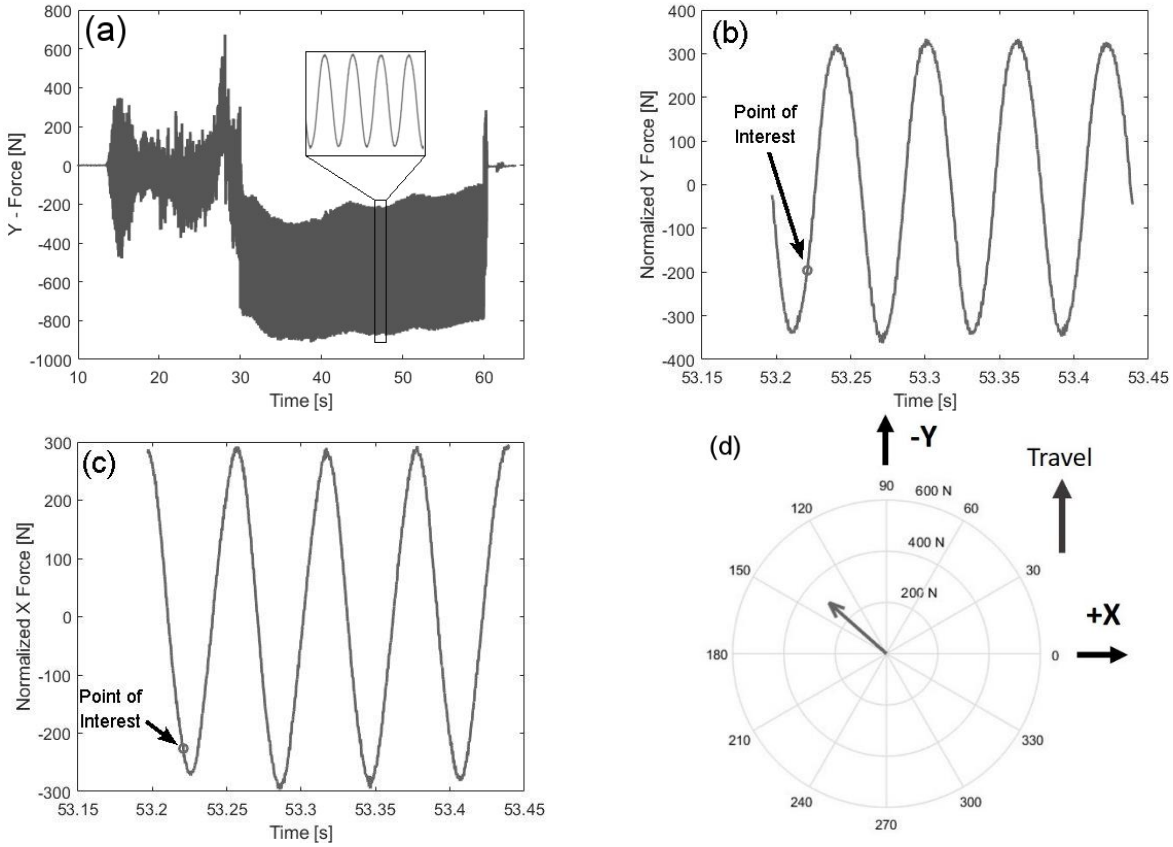

Figure 4: Generation of the resultant direction of the oscillatory component of the process forces in the X-Y plane: (a) the full measured Y force signal, (b) the normalized Y force with selected point of interest, (c) the normalized X force with selected point of interest, and (d) combination of selected X and Y force at point of interest in the plane of welding.

The resultant force for each tool prior to leveling the tool shoulder with the CNC mill is illustrated at a point in time (when the reference flat is at the trailing edge) during the steady-state portion of the weld in Figure 5. The angular positions of the tool features at this specific point in time are overlaid on the compass plot. The tool is represented as a cross-section of the probe in the X-Y plane showing the angular location of the three flats. The dashed line labeled “RO” represents the angular position of the most eccentric point of the tool and the dashed and dotted line labeled “S” represents the angular position of the lowest point of the slanted tool shoulder. The dashed circle represents the tool path for the motion for an eccentric tool. Note that the eccentric tool path is not to scale. For Tools 1 and 2 (lower tool runout) the direction of the resultant

force is perpendicular to the angular position of the low point in the tool shoulder slant and leads the slant in the direction of rotation (counterclockwise). This suggests that the low point of the shoulder is digging into the workpiece material and applying a force to the material in the direction of rotation. In contrast, for Tool 3, the large amount of runout outweighs the effect of the shoulder slant and forces the direction of the resultant force to be towards the most eccentric part of the tool. This suggests the eccentric motion of the tool probe applies a normal force to the workpiece material as it rotates. The directions of the resultant forces with respect to the features were confirmed by performing multiple repetitions of each weld. Additionally, within a rotation, the direction of the force with respect to the angular position of the tool remains constant, *i.e*., there is no significant change in phase between the direction of the force and the tool within one rotation.

Figure 5: Direction of resultant force with respect to angular position of tool features prior to leveling of tool shoulder for (a) Tool 1, (b) Tool 2, and (c) Tool 3. Note that the circle representing eccentric tool path is not to scale.

Figure 6 shows the direction of the resultant force with respect to tool features during welding after the shoulders of each tool had been machined level will the CNC mill. Without the low point of the tool shoulder digging down into the material, only the eccentric motion of the tool probe can apply an oscillatory force to the surrounding material. This is observed for Tools 1 and 2 where the direction of the resultant force now points to the peak of the tool probe that is nearest the most eccentric point of the tool. Additionally, for all three tools, the amplitudes of the oscillatory forces (magnitude of vector) reduced after leveling the tool shoulder. This is seen more clearly in

Tool 1 and 2 as the amplitude was first driven by the shoulder slant (before leveling) which was larger than the force applied by the eccentric probe. With the slant removed, the smaller force applied by the eccentric probe manifests itself. The imperfection (slant or runout) that will drive the force oscillation will be dependent on the magnitude of each as well as the size of the shoulder compared to the size of the probe. Furthermore, specific alignment of the angular positions of the slant and runout would cause them to add together (runout leads slant by approximately 90°) or subtract from each other (runout trails slant by approximately 90°).

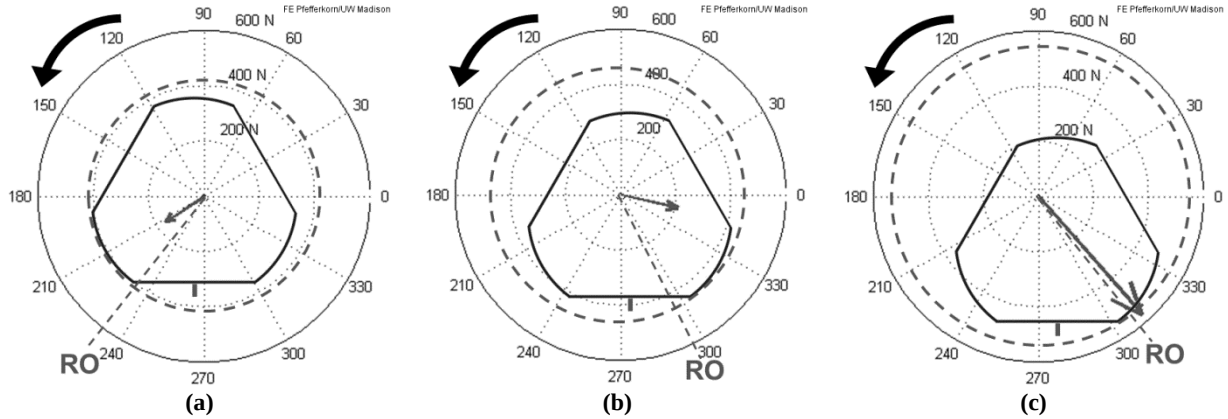

Figure 6: Direction of resultant force with respect to angular position of tool features after leveling of tool shoulder: (a) Tool 1, (b) Tool 2, and (c) Tool 3.

Figure 7 shows the values of the amplitudes in the measured X and Y force signals for two replications 1,000 rpm and 200 mm/min (non-defective) for each of the three tools after the shoulder slant was removed. The amplitude of the force oscillations appears to increase linearly with the measured static runout. The linear relationships have Y-intercept values close to zero newtons of amplitude at a runout value of zero. This suggests that the majority of the force oscillation stems directly from the eccentric motion of the tool, *i.e.,* there is not an apparent additional mechanism that generates a significant component of the amplitude. These results support the findings reported by Zaeh et al. [24] that examined the amplitude of the oscillating process forces for two different tools, one that had a runout of 300 μm, and one that had a runout of 1 μm, which was created by turning the tool on the same machine that welding was performed on. Plunging tests (friction stir spot welds) resulted in amplitudes of approximately 300 N and 10

N, respectively, which corroborates the current linear relationships seen. Since it appears that the eccentric motion of the tool is fundamental in generating the oscillatory nature of the process forces, it must be considered when developing a force-based detection method that relies on the oscillatory forces. In addition, the slant of the tool shoulder must be considered if it is the driving factor.

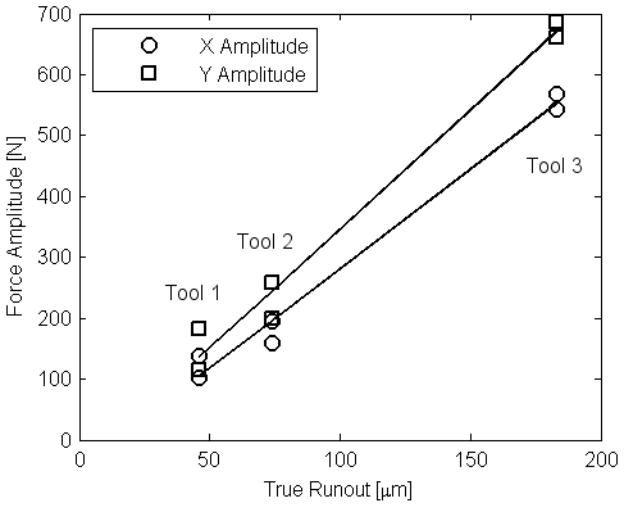

Figure 7: Relationship between the magnitude of static runout of the tools and the amplitudes of the process force oscillations during good welding conditions.

The aforementioned results are fundamental in understanding the underlying mechanisms of material flow during friction stir welding. The observation that the resultant component of the oscillatory process force points toward the most eccentric point of the tool (or leads the low point of a slanted shoulder), in combination with the linear scaling of the amplitude with increased runout suggests that these imperfections are the primary drivers of the oscillatory process force and the intermittent flow. It appears that the oscillatory process forces do not stem primarily from a change in contact condition between sticking and slipping, or from a forming and filling of a cavity once per tool revolution as have been previously proposed. However, it must be noted that other mechanisms can be present but secondary to the eccentric motion of the tool (for the current welding conditions). It is feasible that the eccentric motion of the tool instigates either strain localization or the opening of a small cavity which then develops into the banded features

observed in the microstructure of friction stir welds. Additionally, the direction of the resultant force suggests the equal and opposite reactionary force that the workpiece material applies to the tool should constrain the eccentric motion of the tool during these particular welding conditions. This is contrary to the hypothesis proposed by Fonda *et al.* [13] suggesting that the oscillatory forces help generate an additional oscillatory motion of the tool on top of the tool's natural runout. The current results do not mean that it is not possible to have an additional oscillatory motion that is generated by the oscillatory forces. Prior research has shown that FSW systems can become unstable and a larger oscillatory motion, *i.e.,* long-range oscillation, can be imposed on the tool. *In situ* measurement of the eccentric motion of the tool during welding is covered in Chapter 3. In addition, the potential for long-range oscillations due to and instability in machine dynamics must be considered when developing a defect detection method based on oscillatory force transients.

2.3 Explanation of Defect and Probe Interaction

The progression of the resultant force within one rotation of the tool during a defect interaction is illustrated in Figure 8, which shows the direction and amplitude of the resultant force in 30° increments for a weld performed with Tool 3 at a rotational rate of 1,000 rpm and a travel speed 600 mm/min. Note that the images in Figure 8 show measured force and angular position of tool features, but only hypothesized deflection of the tool from its eccentric motion (not to scale) and hypothesized void size and location (not to scale). Welds performed with Tool 3 in a good welding condition have an oscillatory force amplitude on the order of 600 N. Therefore, during a good weld, the magnitude of the resultant force would remain a relatively consistent 600 N throughout the rotation and its direction would follow the most eccentric peak of the tool probe as illustrated in Figure 6. However, when a defect is forming the resultant force will be altered in the manner as described for each of the corresponding figure letters (Figure 8) as follows:

a) The most eccentric peak (Peak 1) is in the upper right quadrant and the resultant force is pointing toward that peak with an amplitude of approximately 600 N which is indicative of full contact between that peak and surrounding workpiece material.

b) A similar condition to (a). In addition, note that the majority of the material that is moved per revolution is opposite the most eccentric peak of the tool and therefore now resides at the trailing edge of the tool, *i.e.*, the majority of the material is now being extruded in the wake of the tool which is when a breakdown in flow resulting in a defect is most likely to manifest itself due to the intermittent nature of the flow.

c) A lack of material flow into the wake of the tool due to an inadequate thermomechanical state results in the formation of a void volume. The void volume is represented by the dark dotted circle. Currently, the void is located where the peak of the tool probe leading the most eccentric peak (Peak 2) is located. It is hypothesized that at this point the entire tool starts to deflect back into this voided region since less material in that region is present to constrain the tool. The deflection is forced by the large average force being applied to the tool by the material ahead of the tool as the tool travels. This small amount of deflection (represented by the small arrows) results in a reduction in pressure at the leading edge of the tool where Peak 1 resides, which is why the magnitude of the resultant force at the leading edge has started to drop to near 400 N.

d) As the void region continues to expand due to a lack of flow around the tool probe, the tool continues to be deflected back into the void region causing a further reduction in the magnitude of the resultant force at the leading edge, which is now approximately 300 N.

e) The tool is still deflected into the void region by the average forces resulting in the reduced magnitude of the resultant force.

f) Peak 2 is now starting to leave the void region and contact solid material on the advancing side of the weld. This contact will now prevent deflection and thus the magnitude of the resultant force will start to increase.

g) Peak 2 has now moved out of the void region and is now contacting solid material of the advancing side of the weld which prevents the tool from defecting from its original path and restores the magnitude of the force that the eccentric tool applies to the workpiece (back to 600 N).

h) Neither peak of the probe is in immediate angular proximity to the voided region, which prevents the void from altering the resultant force.

i) The most eccentric peak is now moving into the angular position of the void region. An absence of material causes a reduction in the magnitude of the force as the eccentric peak now has less material to push against, *i.e.*, reduction in the direct contact force.

j) The most eccentric peak is still in the void region resulting in a reduced resultant force.

k) Same condition as in (j)

l) The most eccentric peak is now contacting material in the upper right quadrant causing the force to increase back towards its full value of 600 N. The whole process will then repeat itself on the subsequent rotation.

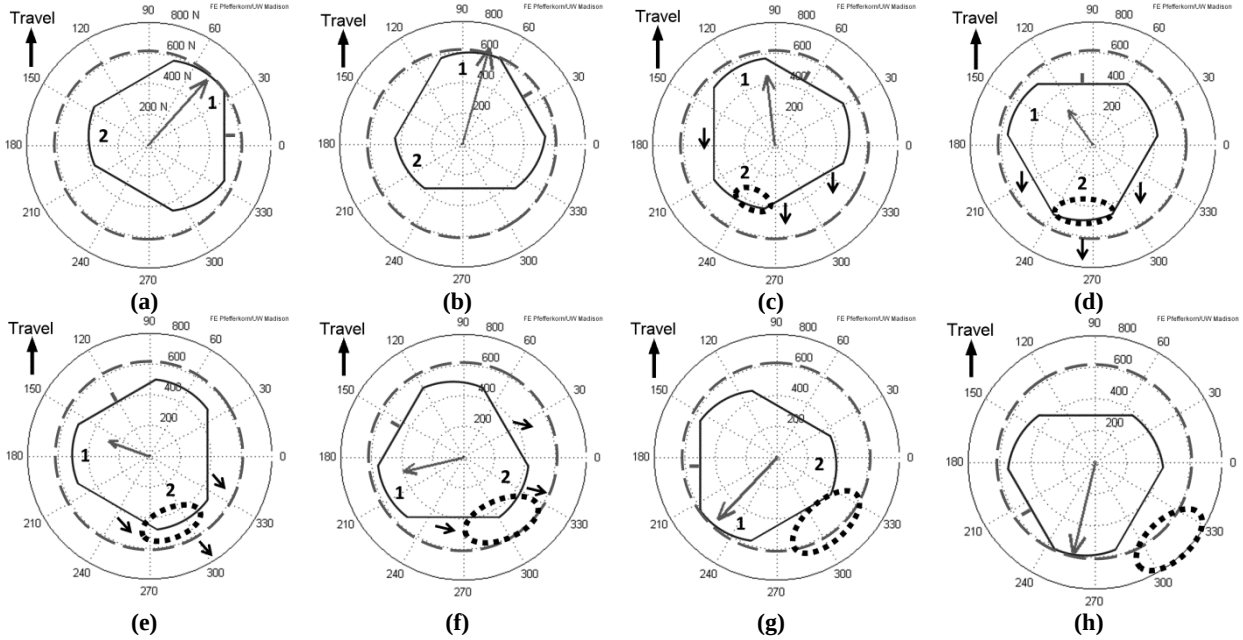

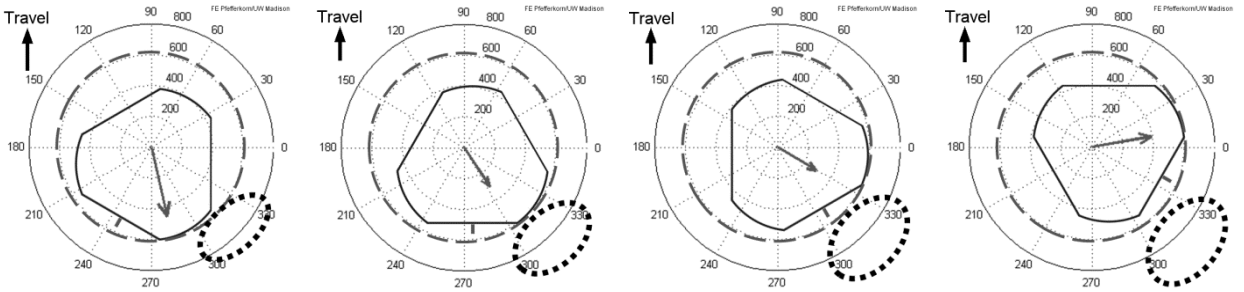

(i) **(j)** **(k)** **(l)**

Figure 8: The progression of the resultant component of the oscillatory process force at 30° increments during defect formation. The progression of (a) through (l) is described in the proceeding text. Note: the force and angular positions are measured but the size and location of tool deflection and voided region are hypothesized and not to scale.

The fundamental understanding of the probe/defect interaction proposed in Figure 8 illuminates how aspects of the process will affect the development of a method built on this concept. The hypothesis relies on the deflection of one of the peaks created by the flats of the tool probe into a voided volume in the wake of the tool when insufficient material is transferred around the trailing edge of the probe. This deflection leads to a reduction in the contact force between the eccentric peak of the tool probe and the material at the leading edge of the tool probe. This suggests that a tool design consisting of deeper flats will create sharper peaks on the tool probe that may deflect more significantly into a smaller voided volume, thus producing a larger distortion in the force signals. Tool wear on the probe features can also become relevant in friction stir welding applications where tool wear is significant. Additionally, deflection of the tool suggests the compliance of the machine is relevant, *e.g.*, stiffer machines will not respond as readily to the presence of a defect as the tool cannot deflect into the voided volume as easily. The compliance of the CNC mill system used in this study is examined measured in Chapter 5. Given that the average process forces measured in the X and Y directions during the defective welds performed in this study range on the order of 1,000 to 3,000 N, substantial tool defections relative to the advance per revolution (thickness of shear layer) are assumed to be achieved during welding. Preliminary investigations of different aluminum alloys performed by Franke *et al.* [37] have shown that harder/stronger aluminum alloys result in larger average process forces in the X and Y directions during welding, and thus produce larger amplitudes at the third harmonic for a given

defect size. It is hypothesized that the larger average forces create a larger driving force for the deflection of the tool probe into the voided region causing a larger distortion for a given void volume. The current hypothesis suggests that it may be possible to sense defect formation through a deflection or acceleration measurement as opposed to a force-based measurement. This would provide the option of attaching an accelerometer to the tool to capture significant accelerations at higher harmonic frequencies during void interaction.

2.4 Effect of Tool Runout on Defect Formation and Size

Welds were created with all three tools in order to examine how the magnitude of runout affects material flow and defect formation. Interestingly, the tool with the largest runout (Tool 3) started to produce defects at a lower advance per revolution (0.5 mm/rev) as compared to the two tools with lower magnitudes of runout (Tools 1 and 2 start to form defects at 0.6 mm/rev). In general, defects are more likely to occur at conditions of larger advance per revolution because the volume of material that needs to be moved around the tool per revolution becomes larger while the heat input per unit length of weld becomes smaller. Additionally, Tool 3 had much larger measured defect areas as a whole. Tool 3 produced welds with an average defect area of 0.496 mm^2 for all welds performed at the 0.6 mm/rev conditions, while Tools 1 and 2 had average defect areas of 0.010 mm^2 and 0.053 mm^2, respectively, at the 0.6 mm/rev conditions. When comparing the average areas of all the defective welds (0.6 to 0.8 mm/rev conditions) performed with Tool 1 and Tool 2, Tool 2 (74 μm runout) had smaller defect sizes with an average defect area of 0.165 mm^2 compared to an average defect area of 0.205 mm^2 for Tool 1 (46 μm runout). An example of the cross sections of defective welds for all three tools performed at the exact same welding conditions of 1,000 rpm and 600 mm/min can be observed in Figure 9. The larger runout of Tool 2 (compared to Tool 1) appears to help paddle more material around the tool probe per revolution, resulting in smaller defects. However, it appears the Tool 3 has excessive runout that is detrimental to material flow around the tool probe leading to larger defects.

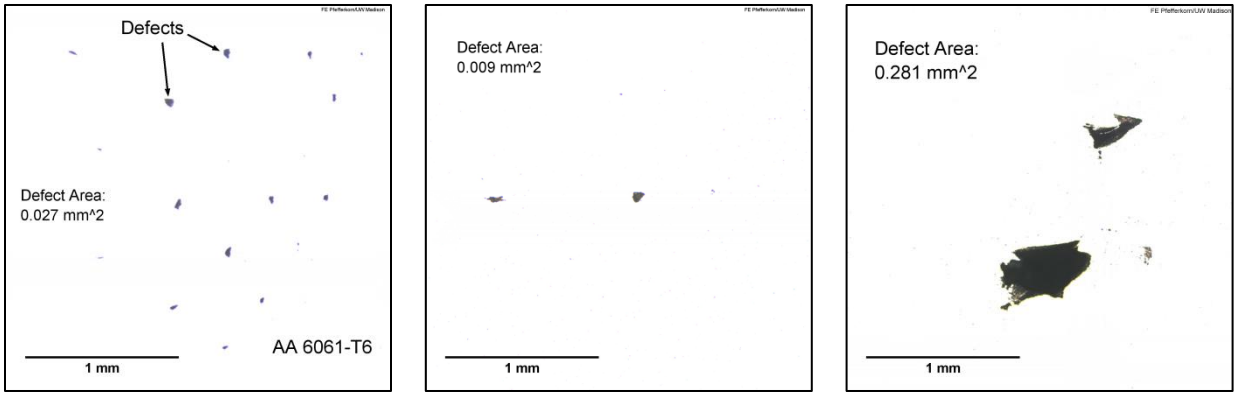

(a) **(b)** **(c)**

Figure 9: Images of the defects produced at consistent welding parameters (1,000 rpm 500 mm/min) by: (a) Tool 1, (b) Tool 2, and (c) Tool 3.

The results are supported by several prior studies which have shown that having a larger magnitude tool eccentricity can help facilitate the flow of material around the tool but only up to a critical point where excessive eccentricity can reduce material flow [38-40]. Chen *et al.* [38] showed that increased tool eccentricity can help prevent defect formation and results in more distinct onion rings in the weld microstructure. Yuqing *et al.* [40] determined that indeed material flow increases with increasing tool eccentricity but only up until a point where the eccentricity becomes too large and reduces material flow. The authors determined that for a tool with a shoulder diameter of 28 mm and a threaded probe tapering from 10 mm in diameter down to 5 mm in diameter that a tool runout of 200 μm produced a maximum stir zone area (more material movement). Tools with runout larger than 200 μm resulted in a decreased stir zone size (less material movement). Given that the tools used in the current work (15 mm diameter shoulder) were approximately half the size of the tools used by Yuqing *et al.*, it would be expected that the critical limit for tool runout should be on the order of 100 μm. This matches the results as Tool Number 3 had a runout larger than 100 μm and Tools 1 and 2 had runouts less than 100 μm. It is hypothesized that the excessive eccentric motion of the tool probe displaces material from the stir zone rather than stirring it around the tool.

2.5 Summary

A fundamental understanding of the mechanisms that drive process force transients and changes in process force transients during defect formation has been proposed. This new understanding allows for a preliminary understanding of how force and torque-based monitoring methods need to be adapted when altering aspects of the friction stir welding process. It appears that small imperfections from an idealized tool (eccentricity and shoulder slant) drive the oscillatory process forces once per tool revolution, and thus are believed to be fundamental in driving the intermittent flow of material around the tool probe once per tool revolution. During sub-surface defect formation, the peaks of the tool probe created by flats interact with voided volumes during each revolution of the tool resulting in a distortion of the force signal as presented in detail in Section 2.3. This illuminates how process factors should alter the proposed friction stir weld monitoring / detection method.

Chapter 3: Influence of Tool Runout on Force-Based Internal Void Monitoring

The objective of any force-based monitoring method is to correlate a change in measured forces with the occurrence and size of voids. The most distinct change observed in the process forces (when using a three-flat tool) is the generation of an amplitude at the third harmonic of the tool rotational frequency due to the distortion in the oscillating force signals described in Chapter 2. It has been proposed that tool runout applies a dynamic force to the workpiece each revolution, which generates the oscillations in the measured forces with a frequency corresponding to the nominal tool rotation rate. When two of the peaks of the tool probe (created by the three flats) each separately interact with a void volume, the interaction produces a momentary reduction in the amplitude at the tool rotational frequency due to the lack of contact. The distortions in the amplitude at the tool rotational frequency can be extracted as an amplitude at the third harmonic when looking at the frequency content of the signal.

3.1 Methods

This analysis in this chapter is performed using the welds within the void interaction welding conditions described in Table 2 in Section 2.1.2. Three cross-sections (in the X-Z plane) were cut from each weld. The cross-sections were cut near the center of the weld with 15 mm between each cross-section. The collected force data confirmed that the friction stir welding process was at a steady state (with regard to the average process forces) at the center position of the weld where the sections were cut. The distances of the cross-section locations from the start and end of the weld (in terms of where the trailing edge of the tool probe resides at each position) were measured with an estimated uncertainty of ±1 mm. These distances were then used to locate approximate points in time within the force data by examining where the force in the travel direction (Y direction) spiked at the start of the weld (designates start time corresponding to the zero position) and dropped rapidly at the end of the weld (designates end time

corresponding to 150 mm position). A linear relationship between position and time was used to calculate the time within the force data when the trailing edge of the tool probe resided at the position of the cross-section. At each of the three corresponding approximate points in time, a discrete Fourier transform was applied over three tool rotations (three cycles per cross section) in order to extract the frequency content of the X and Y direction force signals with respect to the tool rotational frequency. An illustration of the method of synchronizing cross sections to force data is shown in Figure 10. The method relied on the assumption that the void size and force transients are relatively consistent over several adjacent advances per revolution of the tool. This would allow the three force cycles that span the region of weld from which the cross sections were cut to represent the void area observed. Each cross-sectional void area and corresponding section of force data resulted in a singular data point in the analysis. The average force value that the FS tool applies to the surrounding material (about which the signals oscillate) was also calculated from the same force data over which the frequency content was extracted.

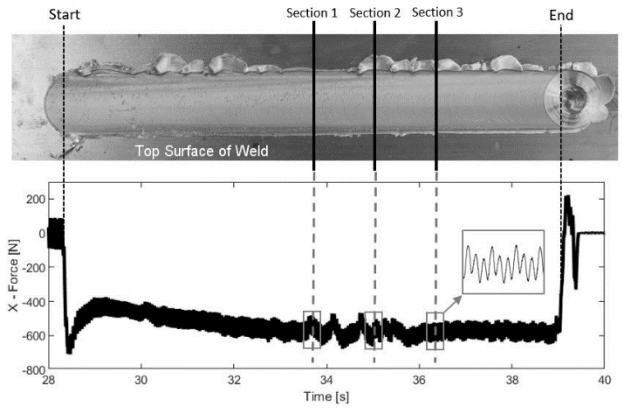

Figure 10: Method of synchronizing the three cross sections per weld to the corresponding force data

3.1.1 Computed Tomography Imaging of Representative Internal Voids

Four welds that contained voids and one fully consolidated weld (as determined by the cross sections) were selected for further three-dimensional computed tomography (CT) imaging to reveal the three-dimensional nature of the voids created in this study. The welds were selected based on the void cross-sectional area and the tool used. Two of the welds with voids were

created by Tool 1, one with void areas at the large end of all of the welds created by Tool 1, and one with void areas towards the small end of the range of areas. Similar welds on the large and small end of void sizes were chosen for Tool 2. The samples consisted of 15 mm sections of weld that were cut from 100-115 mm along the total weld length. All samples were scanned on a Siemens Inveon microCT (Siemens Medical Solutions USA, Inc., Knoxville, TN) utilizing the following parameters: 80kVp, 1,000 µA current, low magnification, bin factor 2, 1.5mm aluminum filtration, 1050ms exposure time, and 600 projections over 220 degrees. Raw data was reconstructed with filtered back-projection by applying the Shepp-Logan filter using the high-speed COBRA reconstruction software (Exxim Computing Corporation, Pleasanton, CA) yielding isotropic voxels of approximately 31.52 microns. The scans were analyzed in the Inveon Research Workplace software. All CT scan datasets were evaluated using threshold values ranging from -700 to 1,000 Hounsfield units.

3.1.2 Measuring Resultant Tool Plunge Depth

An optical profilometer (Alicona InfiniteFocus G4, Graz, Austria) was used to scan the surface of all welds to measure the position of the surface of the weld relative to the initial workpiece surface. All scans were taken with a 5X magnification lens and a vertical scan resolution of 1 µm. All scans were taken across the weld at the position adjacent to the last cross section cut from the weld (15 mm along the weld length after last cross section). A profile (Figure 11) was extracted from each scan by averaging the height data within a 1 mm band across the weld in the Profile-Form Measurement module within the Alicona IF Measure Suite software. The step height from the top surface of the workpiece to the bottommost point of the weld surface was measured. This measurement gives an approximate vertical location of the trailing edge of the tool shoulder during welding.

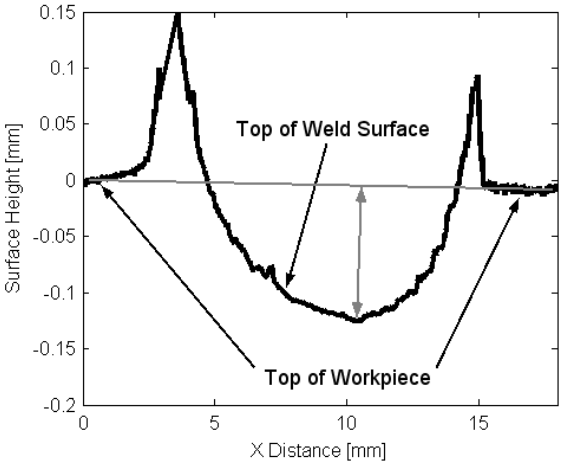

Figure 11: Example surface profile taken from the profilometer scan of a weld surface

3.2 Force Transients Measured Perpendicular to Welding (X-direction)

The primary objective of the current research is understanding how altering the runout of the tool alters the relationship between the amplitude of the third harmonic and void size. Each cross-sectional void area is plotted against its corresponding amplitude at the third harmonic in the X-direction force signal for all three tools in Figure 12. The relationships for Tools 1 and 2 (Figure 12 (a) and (b)) show similar trends. First, there is a distinct cutoff value between the fully consolidated welds and welds containing internal voids in terms of the amplitude of the third harmonic. Secondly, the void areas appear to grow exponentially with an increase in the amplitude of the third harmonic. This suggests that after a certain void size is reached, the amplitude of the third harmonic reaches a pseudo saturation limit. The cutoff values between full consolidation and void presence and the saturation limit are both larger for Tool 2, which had a larger kinematic runout. The larger runout also generated larger force amplitudes at the nominal rotational frequency of the tool during a welding condition with full contact between the probe features and the workpiece, *i.e.*, no void interaction. During a weld with no void interactions (1,000 rpm and 200 mm/min), when the force oscillations were purely at the tool rotational frequency (no substantial amplitudes at higher harmonics), Tool 1 generated an amplitude at the tool rotational frequency of 140 N in the X direction, whereas Tool 2 generated an amplitude of 180 N. These

two values have been plotted as vertical lines at the far-right end of each respective plot. The cutoff value for the amplitude of the third harmonic that differentiates fully consolidated welds from welds with voids in the cross-sections is approximately 30% of the respective amplitude at the fundamental frequency in a full-contact welding condition for both Tool 1 and Tool 2. Additionally, the saturation limit value is approximately 70% of the amplitude at the tool rotational frequency for a full-contact weld. It makes physical sense that the amplitude of the third harmonic saturates at a value less than that of the amplitude at the tool rotational frequency because it appears that the amplitude at the third harmonic is manifested through a reduction in the amplitude at the tool rotational frequency due to a reduction in contact between the probe features and workpiece material. Maximum contact between the probe and surrounding material leads to the maximum force amplitude at the tool rotational frequency in a full-contact welding condition, of which the amplitude of the third harmonic should not be larger than due to less contact. A depiction of how the amplitude at the tool rotational frequency devolves into a saturated amplitude at the third harmonic is illustrated in Figure 13.

The trends observed for Tools 1 and 2 do not extend to Tool 3 (Figure 12 (c)), due to the abnormal flow mechanisms produced by Tool 3 as described in Chapter 2. The larger runout of Tool 3 resulted in void formation at lower advance per revolution conditions than with Tools 1 and 2. Additionally, the voids generated by Tool 3 were larger across the comparative parameter space studied. It has been proposed that the excessively large runout of Tool 3 displaces material from the weld zone as opposed to shearing is around the probe to be deposited in the weld. This displacement mechanism appears to mask the reduction in force when a peak on the tool probe interacts with a voided volume. This results in relatively small third harmonic amplitudes at relatively large void sizes when compared to the relationships observed for Tools 1 and 2. The flow condition produced by excessive eccentricity should be avoided in a production setting. It would be harder to develop a force transient based monitoring method, and such tool conditions would tend to cause voids at less aggressive process parameters.

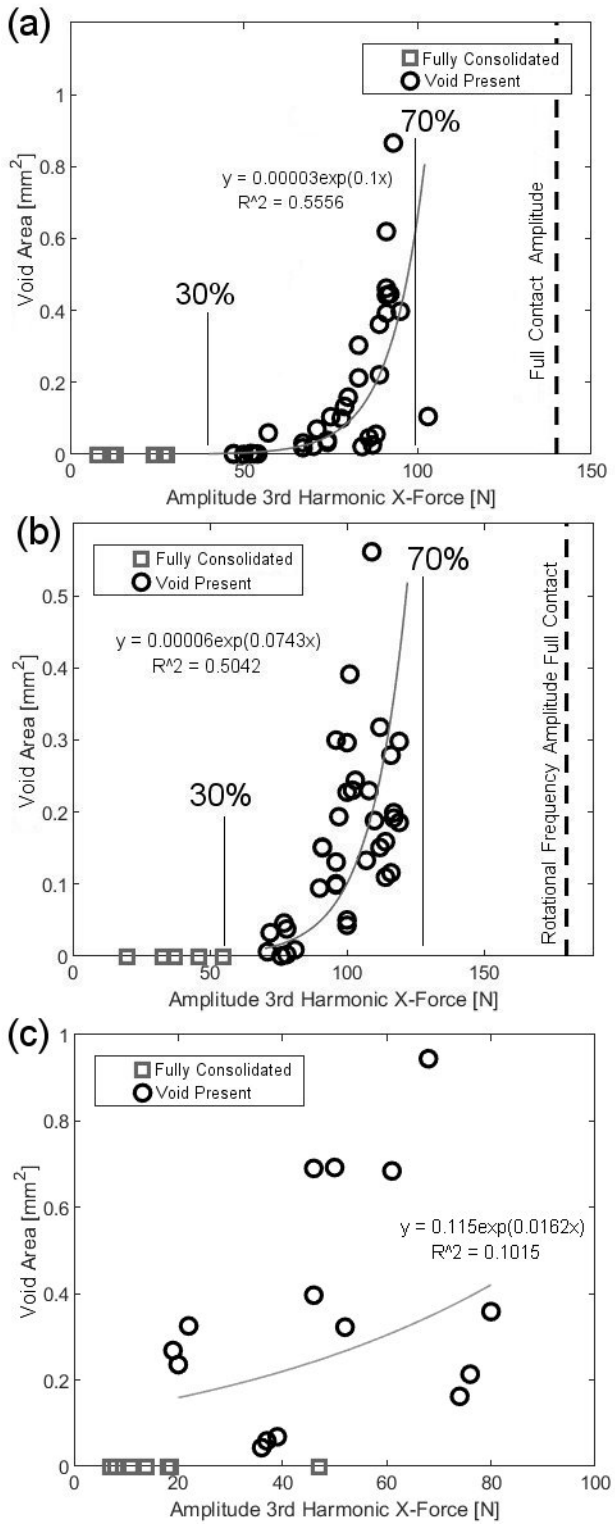

Figure 12: The relationships between measured third harmonic X-direction force amplitudes and void areas: (a) Tool 1, (b) Tool 2, and (c) Tool 3.

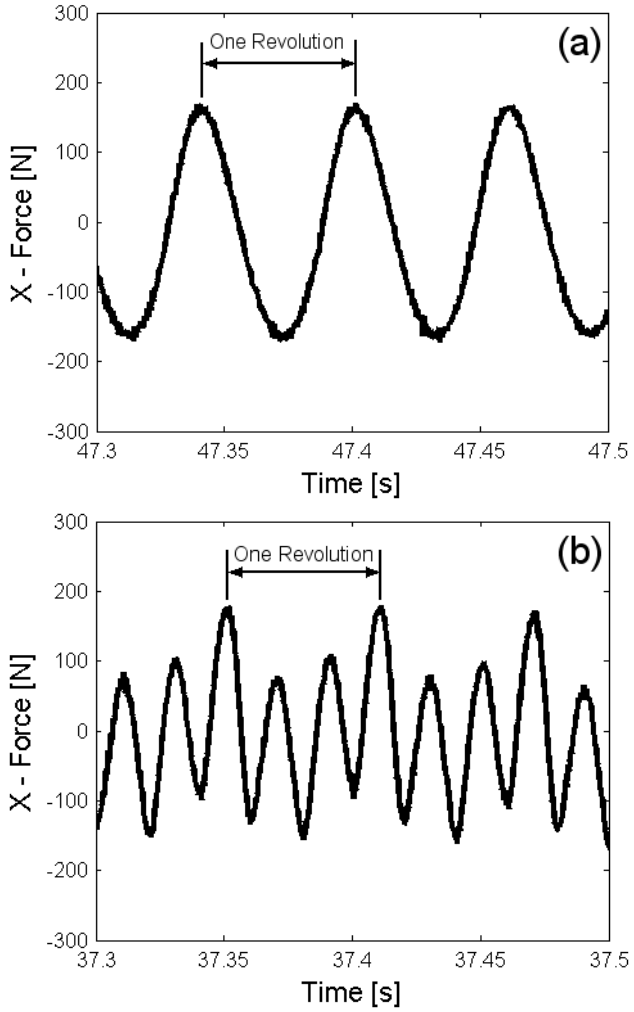

Figure 13: Force signals in X direction during welds performed with Tool 2: (a) welding condition with full probe/material contact within each revolution, (b) distorted signal due to a reduction in material contact leading to an amplitude at the third harmonic that has saturated at 70% the amplitude in the full contact condition. Note: the average force in this X direction has been removed from the signal, i.e., it is normalized around zero.

3.3 Force Transients in the Direction of Welding (Y-direction)

Similar trends to X-direction forces can be observed in the relationships between the amplitude of the third harmonic in the Y-direction and void size (Figure 14). The amplitudes at the tool rotational frequency in the Y-direction tend to be larger than the amplitudes in the X-direction for a given weld. This is due to the eccentric motion adding to the bulk travel motion of the tool. The larger amplitudes in the Y direction during a fully consolidated weld are plotted as vertical lines at the right end of the plots for Tools 1 and 2 in Figure 14 (a) and (b). The amplitudes of the

third harmonic for welds with voids fall within a similar 30-70% range that was previously observed in the X-direction trends. However, there appears to be a larger spread of the data points about the exponential fit as described by the smaller R-squared values. It is hypothesized that the trends are affected by larger variations in the average force values in the Y direction. Within the steady state portion of all welds, the tool applied an average force to the workpiece in the negative Y-direction in Figure 1(travel direction), and an average force in the negative X-direction in Figure 1(due to the shearing that occurs in front of the tool). The force transients in the X and Y directions oscillate around the average force values. It has been hypothesized that the magnitude of the average force impacts the magnitude of momentary deflection of the tool into voided volumes during interaction. A larger average process force will drive the tool to deflect more when an imbalance in the pressure field around the probe is created by the presence of a voided volume. The larger deflection and/or pressure file generates a larger distortion in the force signal. Across the welding conditions studied, the average forces in the X-direction ranged between 577 and 1471 N with a standard deviation of 276 N for Tool 1 and ranged between 1103 to 1951 N with a standard deviation of 262 N for Tool 2. In the Y-direction signals, the average forces ranged between 1798 and 3857 N with a standard deviation of 582 N for Tool 1 and ranged between 1717 and 3561 N with a standard deviation of 474 N for Tool 2. There is an approximate doubling in the range and standard deviation when comparing the X-direction average forces to the Y-direction average forces. This coincides with a reduction in the R-squared values of the exponential trends by an approximate factor of two when comparing the Y-direction trends to the X-direction trends. This suggests that since the driving force for momentary tool deflection into voids is more consistent in the X-direction, it becomes the ideal direction for measuring a force signal that can be used for predicting void size from changes in force transients. However, utilizing both signals does provide more information, and the implementation of a force measurement system from the tool side of the process may consist of a rotating coordinate system in the X-Y plane.

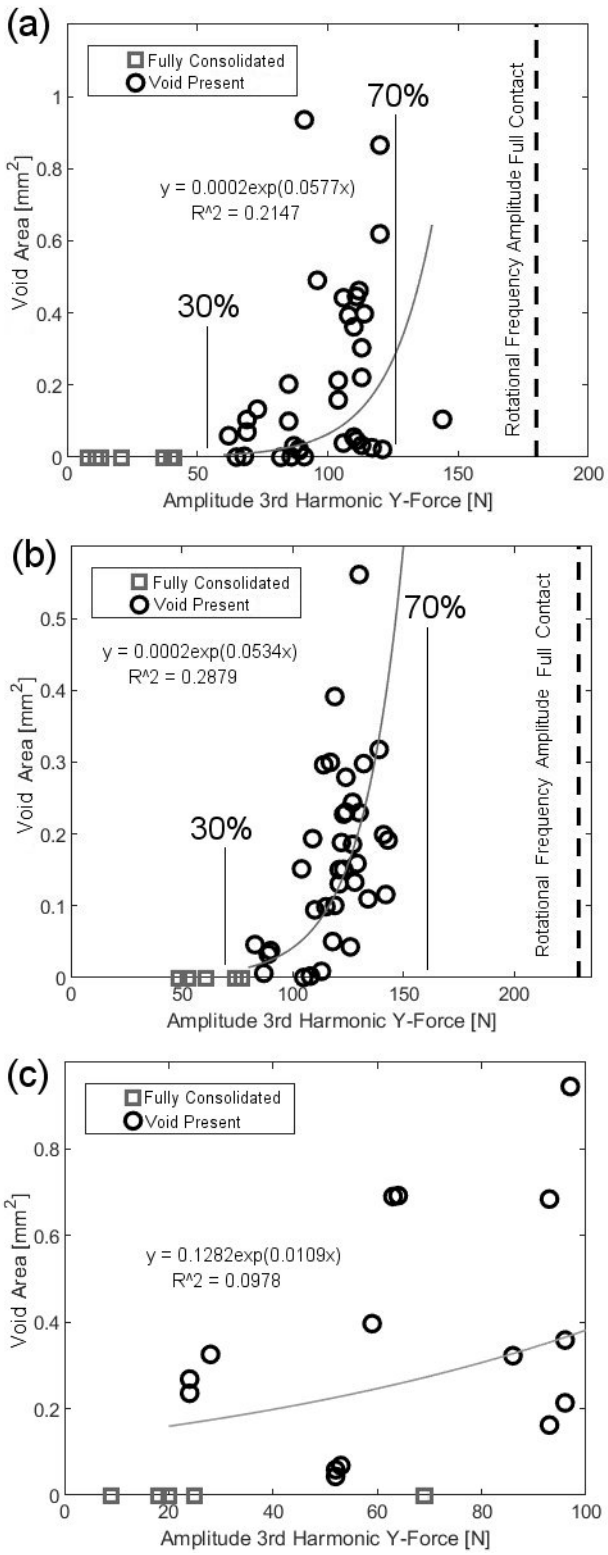

Figure 14: The relationships between measured third harmonic Y-direction force amplitudes and void areas: (a) Tool 1, (b) Tool 2, and (c) Tool 3.

3.4. Force Transients in the Axial (Z) Direction

The axial (Z-direction) force is typically the largest force during friction stir welding, and therefore is often the force measurement of interest. However, it has been hypothesized that the most substantial force distortions occur in the X and Y-directions because the eccentric motion of the probe, and thus the interaction of probe features with voids, occurs in said plane. Since all welds in the current study were performed at a three-degree travel angle, there is an oscillation generated in the Z-direction force signal generated by the runout of the tool. The three-axis coordinate system is defined by the dynamometer, which is aligned with the Z-axis of the tool/spindle. The workpiece itself is tilted at three degrees from the tool and dynamometer. The oscillation in the Z-direction formed because more pressure under the tool shoulder is generated when the most eccentric point of the probe was in the trailing direction of the process (resided deeper in the workpiece). There appears to be a momentary reduction in this pressure when a peak of the tool probe interacts with a void under the trailing surface of the tool shoulder. This also generates an amplitude at the third harmonic in the Z-force signal. However, for welds where the most severe void interactions were observed (when X and Y amplitudes of the third harmonic are on the order of 100 to150 N) the amplitude of the third harmonic in the Z-force only reached maximum values on the order of 50 N. The magnitude of the average force measurements in the Z-direction (for the parameters studied) was on the order of 10,000 N. In the plane of welding (X and Y), the magnitudes of the average force measurements were on the order of 1,000 to 3,000 N. This means that the signal to total measurement ratio is reduced by approximately a factor of 10 in the Z-direction as compared to X or Y-directions. The results suggest that it may be possible to develop a force transient void monitoring method using Z-direction force signals, *e.g.*, if it is the only force measurement available. However, it appears that a Z-direction method would result in a reduction in sensitivity when compared to a method based on force measurements in the X-Y plane.

3.5 Forging of Void Volumes by the Trailing Tool Shoulder

Research has shown that utilizing a tool travel angle (tool tilted away from the direction of travel) can be beneficial to material movement during friction stir welding of aluminum alloys [2, 3]. It is hypothesized that the travel angle of the tool allows the trailing edge of the shoulder to provide additional forging and consolidation of the workpiece in the wake of the tool probe. This hypothesis would suggest that there are two main consolidation processes during friction stir welding, as they pertain to sub-surface void formation, when utilizing a travel angle. The first is the forging of material around the probe in a rotational manner (Process 1 in Figure 15), and the second is the subsequent forging of the material downward by the trailing shoulder surface as it displaces the volume of material corresponding to the projected area in front of the shoulder in the direction of travel (Y-direction) as the tool traverses (Process 2 in Figure 15). This hypothesis is relevant to the current work because the distortions in the process force transients are resultant of an interaction between the features (peaks created by flats) on the tool probe and voids, *i.e.*, it only describes the state of the void in its condition as it interacts with the probe due to a breakdown in Process 1. One limitation of the force transient based detection method is that it does not capture how the forging action of the trailing shoulder (Process 2 in Figure 15) affects the size of voids that may have formed during Process 1. The force transients cannot capture shoulder displacement effects because the shoulder is not the primary driver of the force transients (eccentric motion of the shoulder occurs at and above the top surface of the workpiece), and the shoulder does not have features that interact with voids to produce distinct changes in contact. Additionally, prior literature has proposed that the shoulder never comes into direct contact with sub-surface voids since sub-surface voids form within the probe driven region [11, 18, 23, 34].

The hypothesis regarding the forging action of the trailing shoulder is supported by the result that there are significant amplitudes at the third harmonic (breakdown in probe driven flow causing void interactions) for welds that end up becoming fully consolidated in their final state

when sectioned. For example, multiple welds resulted in full consolidation in their final state when sectioned (square data points in Figures 12 and 14) while the force signals exhibited significant amplitudes at the third harmonic. For Tool 2 there was third harmonic values up to 60 and 77 N (X and Y directions, respectively), and for Tool 1 there were values up to 30 and 45 N. These amplitudes can be compared to the full contact conditions (exemplified in Figure 13 (a)) where the amplitudes of the third harmonic are generally less than 5 N. It is hypothesized that voids were not observed in the final state of the welds corresponding to the square data points in Figures 12 and 14 because the forging action of the trailing shoulder compensated for the lack of material flow around the probe that resulted in a void temporarily forming around the probe, which generated the significant amplitudes at the third harmonic measured in the force signals. The trailing shoulder was not able to fully consolidate the temporary void once the void became large enough to create an interaction with the tool that generated an amplitude at the third harmonic greater than the 30% cutoff value observed. The trailing shoulder surface must either displace material down into a sub-surface void or outside the weld zone as flash. It is hypothesized that the plunge depth of the trailing shoulder into the workpiece will alter how the material is displaced to the two potential locations. The measured resultant plunge depth of the trailing shoulder (refer to Figure 11) for all welds performed with Tool 1 ranged between 22 and 78 μm (37 μm average with a standard deviation of 22 μm) below the top surface of the workpiece. The variance in shoulder plunge is believed to be a contributor to the spread of the data points in Figures 12 and 14. A future systematic study of the resultant plunge depth is needed in order to understand its effect on void size.

The hypothesis of the forging action of the trailing shoulder was further tested by creating a stop-action weld sample during a condition with voids, and then subsequently imaging the wake of the tool probe within the stop-action sample using high energy X-rays to examine the state of voids underneath the trailing tool shoulder. The workpiece sample consisted of an 8.5 mm thick section of aluminum alloy 6061-T6, and the tool was scaled down in size by a factor of two so that

the welding action could be contained in the thin workpiece section. The thin section was needed for improved transmission during imaging. The stop-action weld was produced by activating the emergency-stop button on the CNC mill during the steady-state portion of a weld, which caused the spindle rotation and linear travel to halt. The tool remained fully engaged with the workpiece and the two bodies remained in a static state that is hypothesized to be similar to their state during the weld. Areal density image data was collected at the X-ray Science Division Beamline 32 ID-B at the Advanced Photon Source, Argonne National Laboratory. The areal density image (Figure 15 (b)) is a representation of the density of the material that the X-rays transmit through. The absence of material density in the voided region is clearly distinguishable. The shape of the voided region shows that height of the void (in the Z-direction) at the tool probe is much larger than the height of the void after it passes below the trailing shoulder. This observation supports the hypothesis presented in the previous paragraphs.

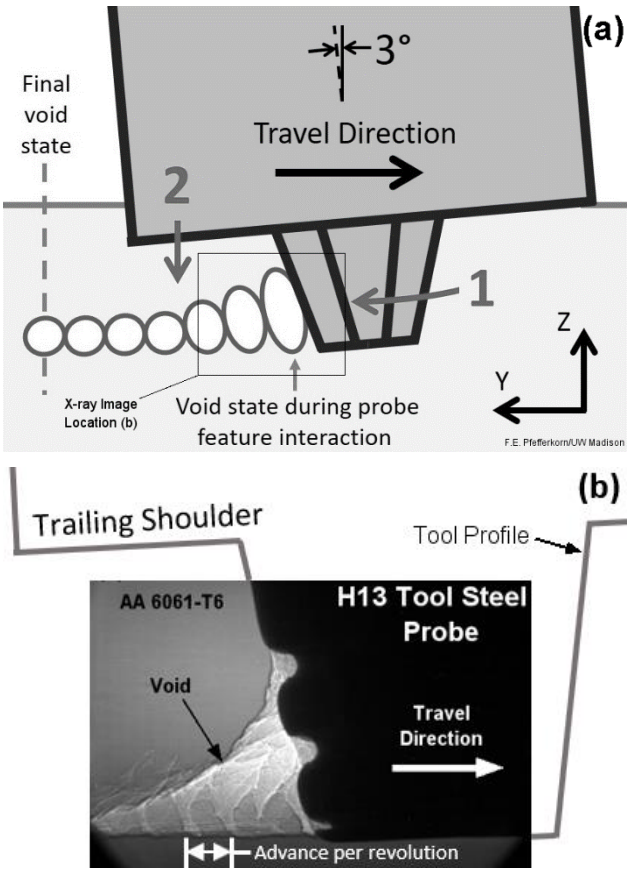

Figure 15: Illustration of the two consolidation processes achieved when friction stir welding with a 3° travel angle: (a) schematic of the hypothesized material motion with a box representing the location of the X-ray imaging, and (b) areal density (X-ray) image of the void region trailing the tool probe in a stop-action weld performed with a 3-degree travel angle.

3.6 Application of the Detection Method

Application of the method would involve extracting the amplitude of the third harmonic from the X and Y force signals, comparing them to the 30% cutoff value for the particular tool to determine whether the weld is fully consolidated or not, then using the exponential relationships to estimate the size of the void. A prediction of void size is important because small voids can be considered acceptable if they do not affect function. Within the current state of understanding, the exact trends can be assumed to be valid only for the current welding setup, *i.e.*, using the same machine and tool geometry while welding in aluminum 6061-T6. The geometrical properties of the tool probe will also influence the force transients generated during void interaction. Deeper flats (which create sharper peaks) may possess a greater potential to react with smaller void

volumes. The depth of threads on the tool probe will also affect how the features interact with a void. Geometric effects on force transient generation will need to be addressed in future research in order to fully understand the process. Additionally, the effect of different workpiece alloys on the force transient generation process needs further study. Different material properties of different alloys produce different resultant process forces under the same commanded process parameters. Preliminary work by Franke et al. [37] has proposed that aluminum alloys with higher hot strength produce larger average process forces during welding. The larger average process forces correspond to a higher pressure in the material around the tool probe. Within the higher pressure field, the effect of the disturbance created by the presence of a void will be amplified. The momentary deflection and force generation will also be dependent on the stiffness and dynamics of the machine that is used. Further details on the stiffness of the system examined in the current work can be found in Chapter 5.

The current study is a continuation in the understanding of the method proposed in Shrivastava *et al.* [18]. The prior work utilized the normalization of the amplitude of the third harmonic by the amplitude at the tool rotational frequency of the given force signal to produce a value that could be used to differentiate between voided and fully consolidated welds. It was determined that a weld contained a void when the normalized value became larger than 0.2. This normalization was utilized because examination of the amplitude of the third harmonic alone did not provide a strong differentiation. Additionally, the void size prediction model involved a relationship between the amplitude of the third harmonic normalized by the average Y-force and the size of the void normalized by a pseudo volume of sheared material based on the advance per revolution. The major difference between the current and prior work is that the geometric imperfections of the tool (runout and shoulder slant) were not considered previously. It is hypothesized that the tool used by Shrivastava *et al.* had a slanted shoulder surface that rotated with the tool. The shoulder is the primary driver of the force oscillation when a significant slant in the shoulder surface is present. In the current work, the shoulder slant was removed by turning

the shoulder while the tool was rotating in the spindle of the machine on which friction stir welding was performed. In the prior work, the amplitude of the third harmonic was never larger than 55% of the amplitude at the tool rotational frequency for a given force signal during void interaction, *i.e.*, the primary component of the signal remains at the tool rotational frequency. It appears that the larger amplitude of the signal at the nominal rotational frequency of the tool is driven by an unbalanced shoulder surface. The more significant reaction at the tool shoulder surface masks the interactions with the voids that form at the probe level. In the current work, the amplitude of the third harmonic became the primary component of the force signal, *i.e.*, much larger than the amplitude at the tool rotational frequency within the signal. This can be observed in the signal shown in Figure 13 (b), where the primary amplitude of the signal is at the third harmonic with an amplitude of 80 N, while the component of the signal at the tool rotational frequency is only 20 N. The elimination of the shoulder slant in the current work appeared to isolate the probe/void interaction by isolating the effect of the probe's eccentric motion on the oscillatory forces at the tool rotational frequency. This isolation appears to provide a more direct relationship between the amplitude of the third harmonic and the void size.

3.7 Discussion of Experimental Method Assumptions

Cross-sectional area measurements of void areas are the most accessible way of quantifying void size. However, using an area measurement to describe a volumetric entity will introduce experimental uncertainty. In this analysis, it was assumed that voids were generated each revolution and that once the weld has reached a steady state, the void formation process remained relatively consistent over several advances per revolution. It is not readily achievable to match a singular void volume within the resultant weld to a singular oscillation in the force data. Therefore, several force cycles were used to calculate the frequency content, and a cross-sectional area was extracted from the length of the weld corresponding to those force cycles. The volumetric nature of the voids was examined using X-ray computed tomography (CT) datasets of

selected welds in order to determine the consistency of the void size over several revolutions (Figure 16). The observed features at the distance of the advance per revolution confirm that the voids are formed on a per revolution basis. However, even at the smaller end of the void size range for both tools (Figure 16 (a) and (b)), the voids stack together to create a semi-continuous trench in the welding direction. This suggests that when sectioning the welds perpendicular to the travel direction a representative volume will be exposed regardless of the exact position along the weld length. The representative area will vary depending on the exact position of the section plane within each advance per revolution. The variation within these sections is illustrated in Figure 17. It can be observed that different sections from a singular weld expose void areas on similar orders of magnitude to each other and distinguishable from welds at different process parameters. Additionally, Table 3 reports the average and standard deviation of the area values from the three total cross sections cut from each singular weld performed with Tool 1. This provides additional quantification of the variation within the three area measurements from a single welding parameter. The variation introduced by the sectioning method is a contributor to the large spread in the data shown in Figures 12 and 14. This effect appears to be most significant in the larger voids created with Tool 1, as the voids appear more discontinuous (Figure 16 (c)). It appears that the largest voids created by Tool 2 (Figure 16 (d)) tend to be more continuous than the largest voids created by Tool 1 when comparing the morphology of each. The effect of the larger eccentricity of Tool 2 on material flow appears to affect the morphology of the voids by causing them to become more tunnel-like, *i.e.*, it created a more consistent material flow pattern per revolution.

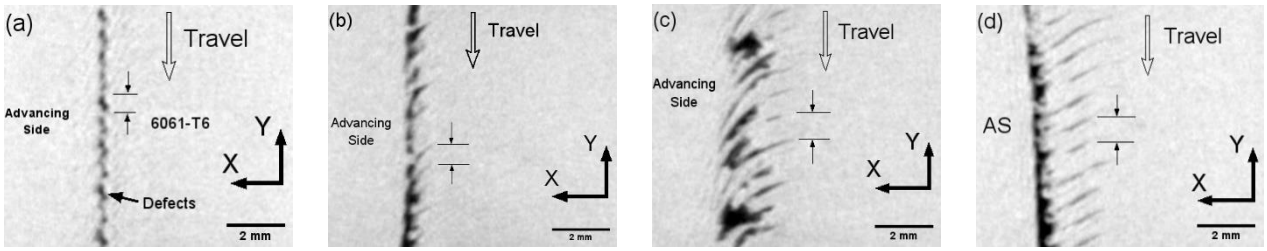

Figure 16: Images in the plane of welding extracted from CT datasets at the vertical positions (2-2.5 mm below top surface of welds) corresponding to the major volume of the voids within each weld: (a) small voids created with Tool 1, (b) small voids created with Tool 2, (c) large void created with Tool 1, (d) large voids created with Tool 2. Note that the advance per revolution of each weld is distinguished by the horizontal lines and arrows.

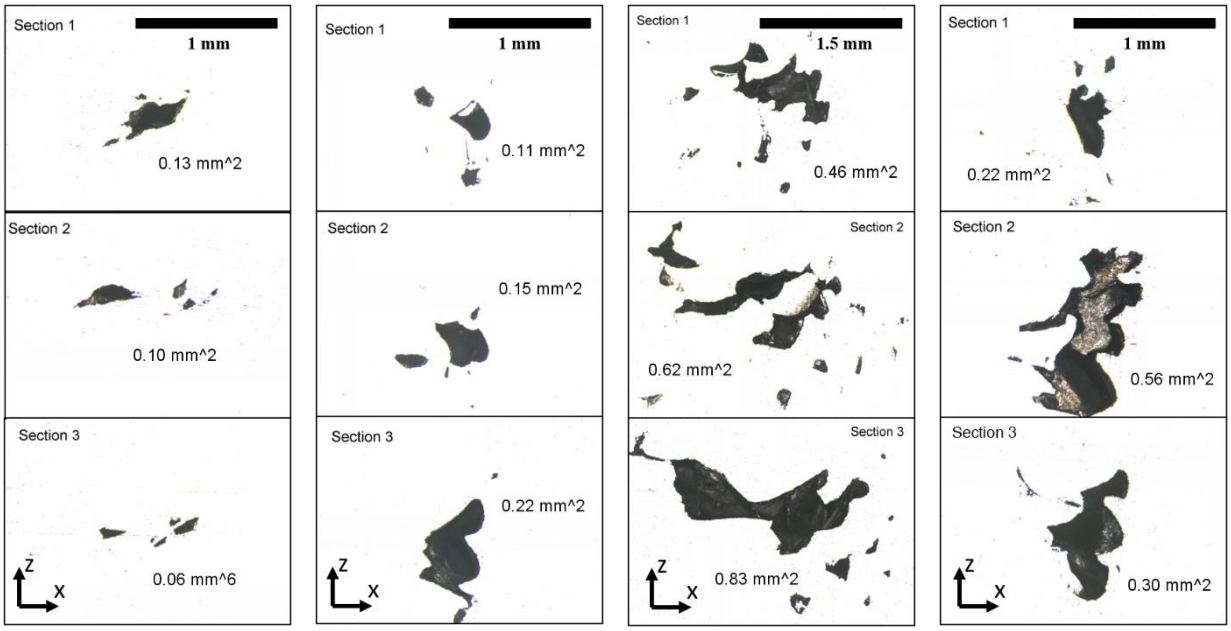

(a) **(b)** **(c)** **(d)**

Figure 17: Three cross sections from within a singular weld at varying weld length positions: (a) small voids created with Tool 1, (b) small voids created with Tool 2, (c) large void created with Tool 1, (d) large voids created with Tool 2. The measured area of each void section is superimposed.

Table 3: Average and standard deviation of void areas taken from the three cross sections at each welding parameter performed with a singular tool (Tool 1). Note that all area values are in mm^2.

		Spindle Speed		
		800 rpm	**1,000 rpm**	**1,200 rpm**
Advance	**0.6 mm**	0.0017±0.0009	0.0267±0.0089	0.0009±0.0006
Per	**0.7 mm**	0.069±0.029	0.375±0.109	0.051±0.038
Revolution	**0.75 mm**	0.098±0.030	0.225±0.059	0.045±0.009
	0.8 mm	0.543±0.031	0.384±0.016	0.644±0.172

The focus of this research is the correlation of void size to changes in process force amplitudes. Prior work using the current force data acquisition system utilized a root sum square method to estimate an uncertainty of ±8.4 N and ±9.4 N in the measurement of the forces in the

X and Y direction, respectively [18]. All force signals in the current work contained a background noise at a primary frequency of 1,000 Hz. The source of this noise is unknown. However, the amplitude of the noise never exceeded 5 N in the force signals used in the current analysis. This noise level is an order of magnitude smaller than the amplitudes that are generated at the third harmonic during welds with voids. Additionally, the frequency is on the order of magnitude larger than the highest frequency of interest in this work which is the 60 Hz corresponding to the third harmonic of the 1,200 rpm cases.

3.8 Summary

Variations in tool runout (on the order of 10's of μm) have a measurable effect on the force transient/void size relationship. This suggests that tool runout must be known and accounted for when implementing a monitoring method derived from the oscillatory force transients described. Additionally, it appears that removing the slant in an unlevel tool shoulder serves to isolate the interaction between the probe applied force and sub-surface voids. Therefore, any uneven nature of the tool's shoulder surface must be known and addressed as well. The detailed conclusions from the research are summarized as follows:

- The force amplitudes corresponding to the third harmonic of the tool rotational frequency grew in the measured X, Y, and Z directions with a positive correlation to the growth in sub-surface void size. However, the growth is more significant in the X-Y plane because the eccentric motion of the tool per revolution occurs in said plane.
- For the range of tool shoulder plunge depths studied, a void remains in the final weld once the amplitudes of the third harmonic in the X and Y directions exceed approximately 30% of the amplitude at the tool rotational frequency from a full tool/workpiece contact welding condition with no interaction.
- Once the voided volume becomes large enough (relative to the process), the amplitudes of the third harmonics saturate around 70% of the amplitude in the force signals at the

tool rotational frequency during a full contact welding condition with no void/tool interaction.

- The correlation between the third harmonic and void size is strongest in the X-direction measurement because the average process force around which the transients oscillate is more consistent than in the travel direction.
- Excessive tool probe eccentricity masks the generation of the amplitudes at the third harmonic. The tool motion appears to displace material from the weld nugget as opposed to shearing it around the tool. Practitioners of friction stir welding should consider the magnitude of tool runout relative to tool size. Based on the current results as well as results from Yuquing *et al.* [40], the runout becomes excessive when its magnitude is larger than 1% of the tool shoulder's diameter when the shoulder diameter is approximately twice the probe diameter.
- Forging of the voided volume by the trailing shoulder of the tool must be controlled or monitored as the force interaction only describes the condition of the void as it interacts with the probe. Additionally, the results suggest that the plunge depth of the trailing shoulder affects the size of the final state of sub-surface voids, *i.e.*, the forging action (Process 2) shown in Figure 15 must be considered by practitioners.

Chapter 4: In Situ Friction Stir Tool Motion Measurements

One objective central to understanding the intermittent flow of material and void formation was the examination of the hypotheses presented in Chapters 2 and 3 through an *in situ* measurement of the motion of the friction stir tool. In Chapter 2, the results showed that the direction of the resultant component of the oscillatory process forces (within the X-Y plane of welding) points towards and rotates with the most eccentric point of the tool. This result suggests that the eccentric motion of the tool applies the oscillatory force to the workpiece. Additionally, it was hypothesized that momentary reductions in the oscillatory process forces during defect interactions are driven by momentary deflections of the friction stir tool from its nominally eccentric path. The goal is to further explain prior force measurements by adding a means of measuring the in situ motion of the friction stir tool. One device capable of measuring such a motion is a single point laser Doppler vibrometer (LDV). The laser Doppler vibrometer operates by measuring the velocity of a surface with a focused laser beam by using the Doppler shift between the incident light and scattered light returning to the measurement instrument. To the best of the author's knowledge, the only prior research that has examined the motion of the friction stir tool during welding was performed by Yan et al. [22] by means of a linear variable differential transformer (LVDT). The current work seeks to provide a deeper analysis of tool motion measurements with a focus on tool motion during defect interaction.

4.1 Experimental Setup

Real-time tool velocity measurements were captured using a Polytec PSV 400 laser vibrometer. The scan head was position perpendicular to the direction of welding (X-direction) as shown in Figure 18. The laser doppler vibrometer measures the frequency shift in backscattered light due to the motion of the surface that it is reflecting off of. It compares the shift between the backscattered light and a reference beam to determine the velocity of the surface in the singular dimension towards and away from the scan head. The laser beam was focused on the edge of

the tool shoulder just above the surface of the workpiece during welding. When the tool rotates eccentrically, the 1-D motion is measured as a sine wave by the vibrometer. A cumulative numerical trapezoidal integrator was used to convert the velocity measurements recorded by the vibrometer to position data. Proper operation of the vibrometer was validated by comparing the amplitude of the free-spinning tool position data to the kinematic runout of the tool measured with a dial indicator. A range of defective and non-defective welds were created in 3003-H14, 6061-T6, and 7075-T6 using Tool 2 from Chapter 2 (74 micrometers true runout).

Figure 18: Image of the experimental setup consisting of the laser vibrometer in relation to the force dynamometer and workpiece clamping system

4.2 Tool Motion during Good Welding Conditions

The single point laser vibrometer measures the motion of the surface it is focused on in a singular dimension corresponding to the direction in which the beam is aligned. The eccentric motion of the tool due to the natural tool runout occurs as a two-dimensional circular motion in the X-Y plane. Therefore, when the beam is aligned in the X-direction the circular two-dimensional eccentric motion of the tool is captured as a sinusoidal signal in the X-direction by the vibrometer. The amplitude of the free-spinning tool position signal captured by the vibrometer was examined in order to confirm that the vibrometer was capable of capturing the eccentric motion of the tool

at the scale on which it occurs. The average peak-to-peak value of the position data was taken to be double the amplitude value at the tool rotational frequency extracted from the position signals by a Discrete Fourier Transform. The average of the peak-to-peak value from the tool position signal across all free spinning vibrometer tests was 76.1 ± 2.6 μm. An example of one revolution of the position signal measured from the tool spinning freely at 1,000 rpm is shown as the dotted line in Figure 19. The small deviations in the signal from a perfect sinusoid are due to small inconsistencies of the shoulder surface from a perfect circle. The true runout of the tool measured using a dial indicator was 73.7 μm (0.0029 in), where the resolution of the dial indicator was 2.5 μm (0.0001 in). The total position change in the vibrometer signal is equal to the dial indicator measured true runout within the bounds of uncertainty for each measurement. Since the vibrometer confirmed the dial indicator measurement, it was assumed that that the vibrometer system can adequately capture the eccentric motion of interest.

The amplitude of the position data measured by the vibrometer for non-defective welds (1000 rpm 200 mm/min) in alloy three alloys is presented in Figure 19. In 6061-T6 and 7075-T6, the amplitude of the eccentric motion of the tool during welding is smaller than the amplitude of the free-spinning tool by 20-30%. This suggests the workpiece material constrains the eccentric motion of the tool during welding. This supports the results in Chapter 2, which showed that the direction of the oscillatory component of the process force that the tool applies to the workpiece in the X-Y plane tracks the most eccentric peak of the tool within each revolution (eccentric motion applies the force to the workpiece), and thus the equal and opposite reaction force should constrain the eccentric motion of the tool. This bolsters the conclusion that the eccentric motion of the tool due to tool runout is the primary driver of the oscillatory process forces. Prior results on tool motion measurements by Yan et al. [22] also showed small reductions in the periodic variations in tool position due to tool runout. The finding that the tool is constrained by the oscillatory processes forces refutes the hypothesis by Fonda et al. [13] that proposed that oscillatory process forces lead to the propagation of eccentric tool motion, which amplifies the

effect of the eccentric motion of the tool on the intermittent flow of material around the tool probe. However, the results still support the primary part of the hypothesis proposed by Fonda et al. that the eccentric motion of the tool is the primary driver of the intermittent flow of material. The only discrepancy is the propagation of motion.

In the 3003-H14 welds, the tool was not substantially constrained. This is believed to be due to the runout of the tool (74 micrometers) being excessive in this alloy. This is similar to the excessive nature observed for Tool 3 in 6061-T6 (Chapter 2). Since welds in 3003-H14 have more plasticity in the shoulder driven region, it is easier for the eccentric motion of the tool probe to displace material radially as opposed to stirring it around the tool probe. When the material is displaced radially it cannot constrain the eccentric motion of the tool. Additionally, the average process forces are smaller during the welds in 3003-H14. A larger average process force would be more likely to constrain the motion of the tool. 7075-T6 had the largest average process forces, which resulted in the largest constraining effect.

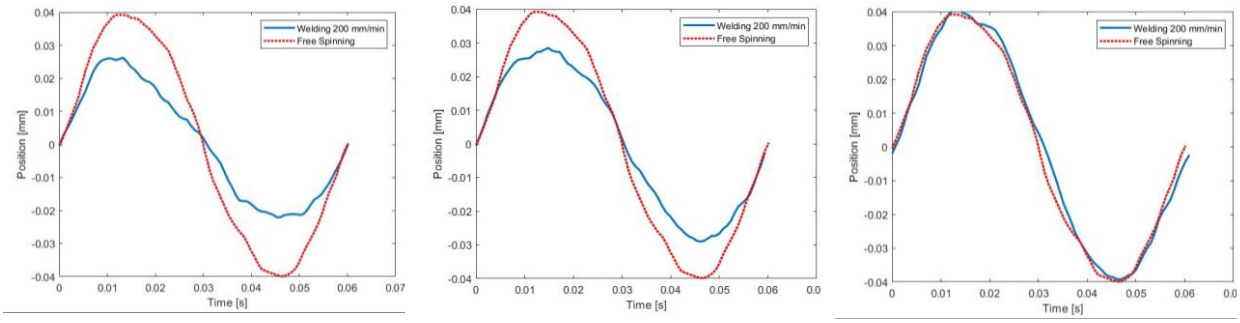

Figure 19: Comparison of the position signal of the FS tool during non-defective welding against the position signal of the free spinning tool (a) 7075-T6 (b) 6061-T6 (c) 3003-H14

4.3 Tool Motion during Defective Conditions

In Chapter 2, the primary hypothesis focused on the physical explanation of what occurs within one tool revolution when features on the tool probe (peaks between flats) interact with subsurface volumetric defects and alter the process force transients. It was hypothesized that the force that the eccentric motion of the tool applied to the workpiece was momentarily reduced

when the peaks of the tool probe interacted with defective volumes because the tool was momentarily deflected from its eccentric path into the defective volumes. This hypothesis was tested by measuring the motion of the friction stir tool with the laser vibrometer during defect interaction. During a fully consolidated welding condition, the process forces oscillate primarily at the tool rotational frequency and the corresponding position signal is also primarily a sinusoid at the tool rotational frequency as shown in Figure 20 (a) and (b). However, when welding in a defective regime, two of the peaks on the tool probe interact with the defective volume formed each revolution to produce two distortions in the force and position signals as shown in Figure 20 (c) and (d).

For both the force and position signals, the positive X-direction is towards the advancing side of the weld (Figure 1). When the most eccentric point of the tool was towards the advancing side of the weld, one of the peaks on the probe opposite the most eccentric point interacted with the defective volume that had started to form on the retreating side of the weld. The narrow peak on the tool probe allowed the tool to be momentarily deflected towards the retreating side into the defective volume. This is labeled as Interaction 1 in Figure 20 (c) and (d). The deflection of the tool towards the retreating side momentarily reduced the force that the eccentric motion of the tool applied to the workpiece on the advancing side. This deflection was resultant of the relaxing of the tool from its nominal position in the X direction that the tool resided at along the length of the weld due to the average process force in the negative X-direction. Note that in the defective welding data shown, the average process force in the X-direction was 2000 N, which would result in significant steady-state deflection of the tool due to the compliance of the system in the X-direction. The second interaction (Interaction 2 in Figure 20) occurred when a second peak on the tool probe moved into the defective volume on the advancing side of the weld which caused the tool to momentarily deflect towards the advancing side causing a momentary reduction in the force that the eccentric motion of the tool applied to the workpiece on the retreating side. The angular encoder data was utilized to verify that that

the two distortions within the two data streams align with each other in the time domain. The angular position of the most eccentric point of the tool is known in the encoder/force timing scheme. Therefore, the point in time encoder/force data when the most eccentric point of the tool at the advancing side edge (nearest to the vibrometer) can be approximately aligned to the most positive point in time in the vibrometer position signal. Precise synchronization of the force and position signals via the angular encoder is examined in Chapter 5.

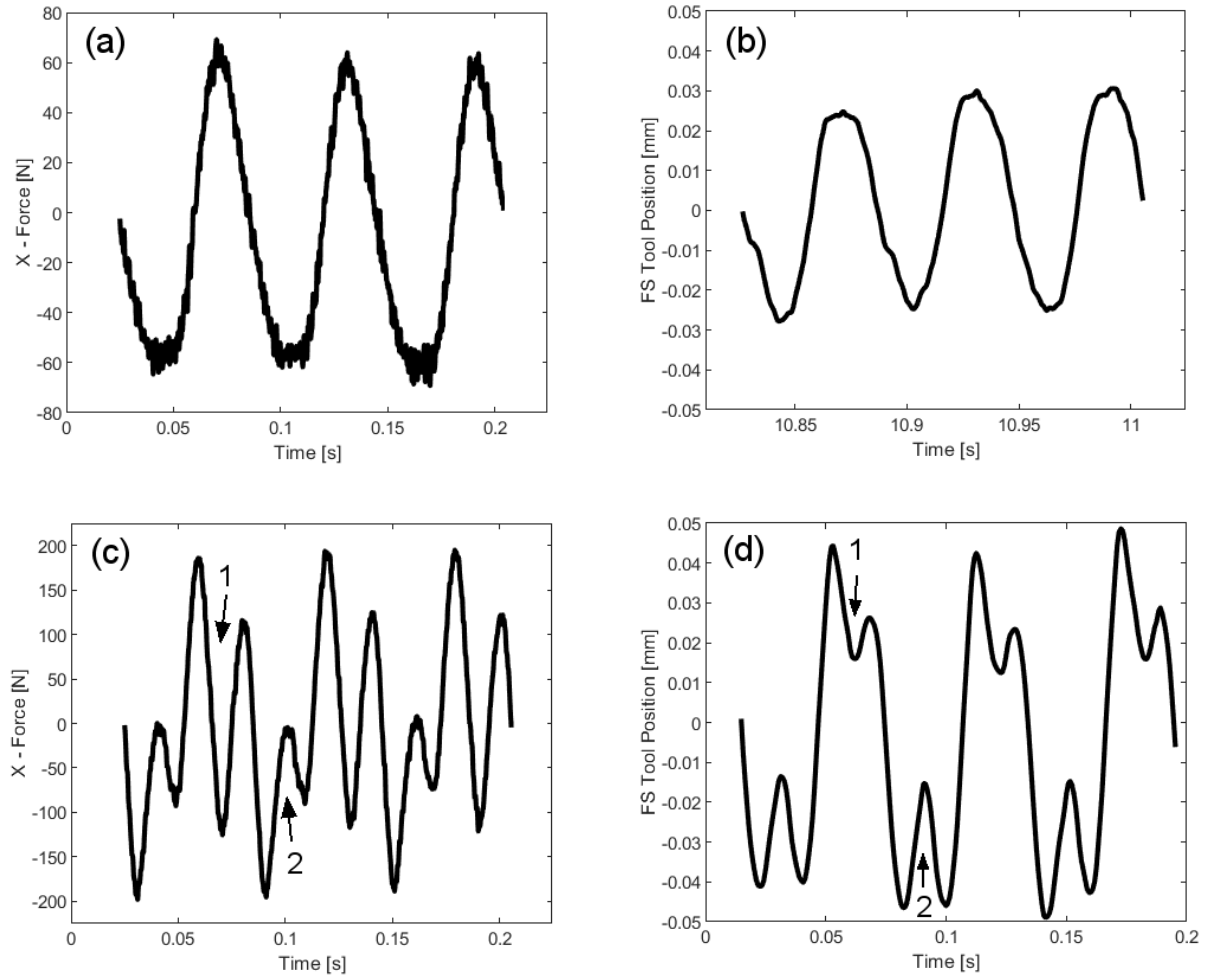

Figure 20: Three revolutions of (a) X-direction force fully consolidated weld, (b) X-direction tool position fully consolidated weld, (c) X-direction force defective weld, (d) X-direction position defective weld. Note: the average components of the force signals have been removed, *i.e.*, normalized around zero.

Prior research on the force transients generated by the interactions previously described has shown that the distortions in the force signals can be extracted as an amplitude at the third harmonic of the tool rotational frequency (the two distortions generate three peaks per

revolution). For the corresponding force and positions signals for each given weld, the amplitude at the third harmonic of the tool rotational frequency was extracted using a Discrete Fourier Transform. The amplitudes at the third harmonic for corresponding position and force signals are plotted against each other in Figure 21 (a). A direct linear relationship was observed, which supports the fundamental linking of the momentary deflection and momentary reduction in the oscillatory process forces. The relationship between the distortions in the force signal and the distortions in position signals should be dependent on the dynamic properties of the welding system, primarily the stiffness of the system. The stiffness of the system used for friction stir welding can vary significantly from more compliant robotic arms to more rigid dedicated gantry-style systems. How altering the stiffness of the system alters the force and deflection relationship will be investigated further in Chapter 5.

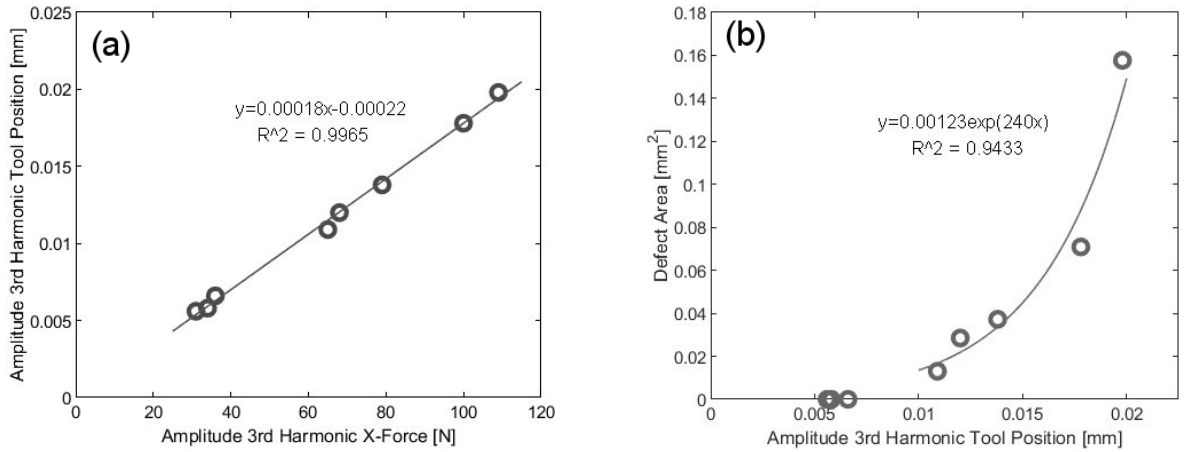

Figure 21: Relationship between the amplitude of the third harmonic in the tool position signal and (a) the amplitude of the third harmonic in the corresponding force signal, and (b) the average area of defects taken from cross sections.

In Chapter 3, it was shown that a direct relationship can be drawn between the distortions in force signals and the size of sub-surface defects left within the weld. The result that the momentary deflection of the tool is fundamentally linked to the distortions in the forces signals suggests that a relationship between the distortions in the tool position signal and defect size can be developed. Figure 21 (b) shows the relationship between the amplitude of the third harmonic in the friction stir tool position signal and the average defect area taken from the

cross-sections of each of the corresponding welds. The trend is very similar to the relationship between the amplitude at the third harmonic in the force signal and defect size reported in Chapter 3. The amplitude of the third harmonic in both signals increased with defect size but reached a limit where the amplitude saturates above a certain defect size. The relationship between distortion in the tool position signal and defect size suggests that a motion-based measurement (accelerometer) has the potential to be used in a method of defect monitoring. An accelerometer-based measurement may be easier to implement from the tool side of the process in a production setting as compared to a force-based measurement. Future examinations must determine if an accelerometer can capture similar tool motions.

In Figure 22, the third harmonic extracted from the position signal is plotted against its corresponding third harmonic in the measured force data for all three aluminum alloys. Across all three, the amplitude in the third harmonic in the position data grows at the same rate as the amplitude in the third harmonic in the force data. This suggests that regardless of workpiece alloy (which typically determines the process forces experienced) the momentary deflection of the tool is directly related to the momentary reduction in the force signal. This suggests that the deflection process is driven by the system's dynamics, which in this case is consistent across all three alloys. The system can be thought of as a spring that is loaded under the average process forces. Once the pressure surrounding the tool is altered by the defect interaction the spring will relax and deflect back towards its unloaded position.

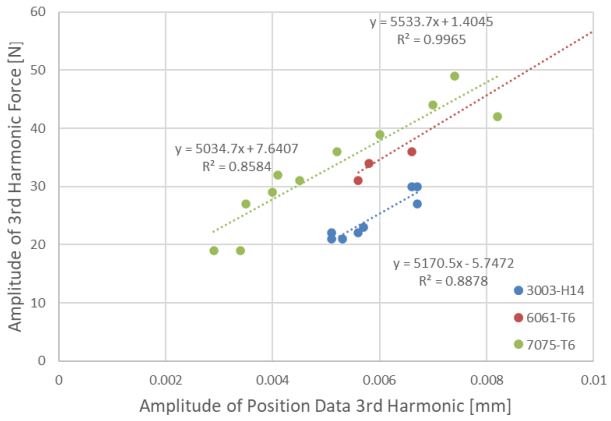

Figure 22: Amplitude of the third harmonic of the position data plotted against its corresponding amplitude in the force data in the X-direction

4.3 Summary

A laser vibrometer system was utilized to produce a real-time non-contact measurement of the microscale motions of a friction stir tool during welding of aluminum 6061-T6, 3003-H14, and 7075-T6 in both fully consolidated and sub-surface defective welding regimes. The conclusions that can be drawn from the results are:

- In fully consolidated welds, during which the tool was in complete contact with the workpiece material (no void interactions that we know of), the workpiece material constrains the eccentric motion of the tool as compared to its eccentric motion due to its runout when it was spinning freely. This supports previous research that suggested that the eccentric motion of the tool was the primary driver of oscillatory process forces in the plane of welding. The magnitude of the constraining effect is dependent on alloy type, with harder/stronger alloys providing a larger constraining effect.
- In defective welding regimes, when the peaks (created by flats) on the tool probe interacted with subsurface volumetric defects, the tool was momentarily deflected into the defective volume. This supports the previous hypothesis that described the physical nature of changes in process force transients during defect interaction.

- The momentary deflection of the tool during defect interaction suggests that a motion-based measurement (accelerometer) holds potential as the basis of a defect monitoring system.

Chapter 5: Dynamic Modeling of Tool Motion during Subsurface Void Interaction

The physical insights on force signals during void/tool feature interaction provided in Chapter 2 suggested that the tool momentarily deflects into the void volume during feature interaction. In Chapter 4 a real-time non-contact measurement of the motion of the tool was captured using a laser vibrometer in order to test this hypothesis, as well as examine the effect of the eccentric motion of the tool on intermittent material flow. The objective of Chapter 5 is to advance the fundamental understanding of what drives the dynamics of the tool motion during welding and void interaction. This fundamental understanding will form the basis of a more robust and adaptable motion-measurement-based void monitoring method. Since a change in force will produce an acceleration, accelerometers also hold potential for capturing interactions between friction stir tools and defects. Accelerometers are attractive for this application due to their low cost and ease of implementation. Accelerometer instrumented toolholders are commercially available and have been used for monitoring the end milling process [41, 42]. The focus of the current research is to build the foundational understanding of the relationship between friction stir welding process forces and motion of the friction stir tool to enable future development of subsurface void monitoring via an accelerometer instrumented toolholder.

5.1 Mass-Spring-Damper-Modeling

The primary objective of the current research was to test the hypothesis that a simple mass-spring-damper model can be used to develop a fundamental understanding of the relationship between the process forces applied to the friction stir tool and the motion that the tool experiences during sub-surface void interaction. The mass-spring-damper model is commonly used to describe the dynamics of end mills during the machining process of milling [43-50]. The mass spring damper model is governed by the standard equation of motion:

$$m\ddot{x} + b\dot{x} + kx = F \quad (1)$$

where *m* is the mass of the system, *b* is the damping coefficient of the system, *k* is the stiffness of the system, and *F* is the force applied to the system. In the current work, the mass of the system was the effective mass of the spindle side of the welding system, the damping coefficient was characteristic of the process damping due to the interaction of the tool and workpiece as well as any damping provided by the spindle structure, the spring constant was the stiffness of the spindle side of the system in the direction of interest, and the force was the force applied to the tool due to the changed in contact pressure between the tool and the workpiece.

The stiffness of the spindle side of the welding system was determined by the combination of the stiffness of the toolholder and the stiffness of the welding machine. The two components can be described as springs in series using the following equation [51]:

$$\frac{1}{k_{eq}} = \frac{1}{k_1} + \frac{1}{k_2} \quad (2)$$

where k_{eq} is the equivalent stiffness of the entire system, k_1 is the stiffness of the toolholder itself, and k_2 is the stiffness of the welding machine. The effective mass of the spindle side of the system, *i.e*., the mass that moves when a force is applied to the tool, cannot be directly measured. However, the effective mass can be related to the stiffness of the system and its natural frequency through the equation of simple harmonic motion [51].

$$f = \frac{1}{2\pi}\sqrt{\frac{k}{m}} \quad (3)$$

where *f* is the natural frequency of the system, *k* is the stiffness, and *m* is the effective mass. Rearranging this equation to solve for *m,* provided a method of estimating the effective mass of the system by measuring the stiffness and natural frequency.

5.1.2 Process Damping in End Milling:

Mass-spring-damper modeling is commonly utilized to understand system dynamics

during machining in order to examine process chatter. End milling is similar to friction stir welding in that both involve a CNC machine tool with a rotating tool that deforms a metal workpiece. In chatter conditions, when the frequency of interest is at or near the natural frequency of the system, damping is relevant to the system's dynamics. Several studies have proposed that the major source of damping in the end milling process comes from the interaction between the cutting tool and the workpiece material [43-46]. The damping coefficient is dependent on the amount of engagement between the tool and workpiece, with more engagement providing more damping. Huang and Wang [43] and Budak and Tunc [44] both reported damping coefficients for end milling up to 500 Ns/m. It was hypothesized that if damping is relevant to the friction stir welding process dynamics, then the damping coefficient should be significantly higher than the highest values reported for end milling since the friction stir welding process involves a tool that is fully surrounded by plasticized material, *i.e.*, substantial engagement between the tool and workpiece.

5.2 Methods

5.2.1 Experimental Apparatus:

Friction stir welding was performed using a 3-axis CNC Milling machine (HAAS, TM-1). Three different transducers were utilized to capture data during welding. A three-axis piezoelectric force dynamometer (Kistler, model 9265) captured the interaction force that the tool applies to the workpiece in the three directions labeled in Figures 1. Additionally, a magnetic angular encoder (HAAS, Part #: 30-30390, 1024 pulses per revolution) connected to the CNC mill spindle captured the angular position of features on the tool within the same timing scheme as the forces. The encoder and dynamometer feed signals to the same data acquisition system (National Instruments, BNC-2090A, PCI-6014, PCIe-6320). Additionally, the tool's linear velocity in the X-dimension was measured via a one-dimensional laser vibrometer system

(Polytec, PSV-400 Scanning Head and Junction Box; PSV-A-420 Geometry Scan Unit; OFV-5000 Vibrometer Controller Unit). Refer to the experimental setup shown in Figure 23.

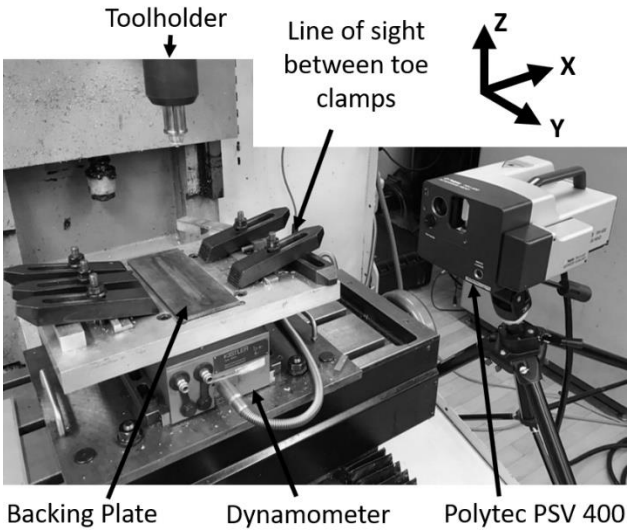

Figure 23: The experimental apparatus used to measure process force and tool motion during welding. Note that the angular encoder is attached to the spindle motor and not shown**.**

5.2.2 Toolholders and Friction Stir Tools:

Two different toolholders were used in order to examine the effect of the stiffness of the toolholder on the dynamics of the tool. Toolholder 1 (Figure 24) was a standard CAT 40, 1-inch inner diameter, end mill holder (Lyndex, C4006-1000-4.00). Toolholder 2 is a custom toolholder designed in-house. Toolholder 2 extends approximately 100 mm further from the machine spindle than Toolholder 1. Both toolholder systems utilized the same friction stir tool (Figure 25) that consisted of a 15 mm diameter concave shoulder and a probe that tapered from 7 mm to 5mm in diameter with three 0.635 mm deep flats and threads. A small indentation was chiseled into the 1 mm wide cylindrical surface that sits just above the tool shoulder and workpiece interface during welding (Figure 25). This is the surface that the laser reflects off of during the vibrometer measurement. When the indentation passes through the laser it provides a small disruption in the vibrometer measurement that was linked to the point in time in the force and encoder data corresponding to the angular position when the indentation is known to be at the same angular position of the laser. The toolholder 1 setup produced a natural tool true runout value of 64 µ, as

measured by a dial indicator at the tool shoulder when rotating freely. The Toolholder 2 setup produced a true tool runout value of 132 µm. Tool runout is a product of how the holders and tools are manufactured as described in Chapter 2.

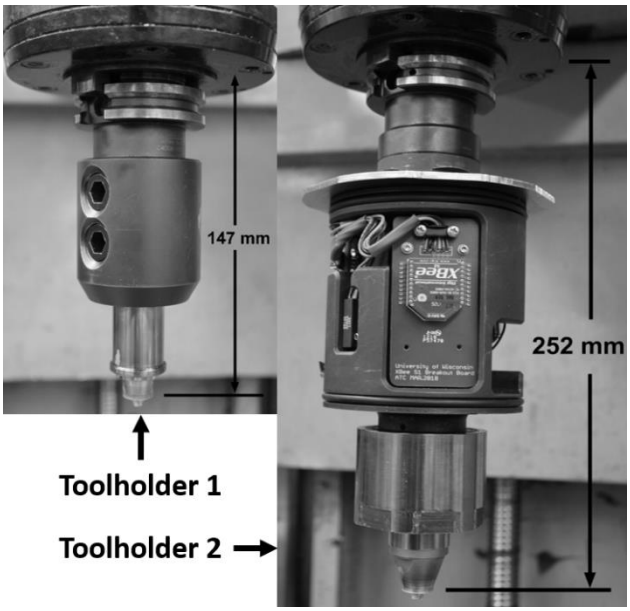

Figure 24: The two toolholders utilized in the study shown mounted in the machine spindle

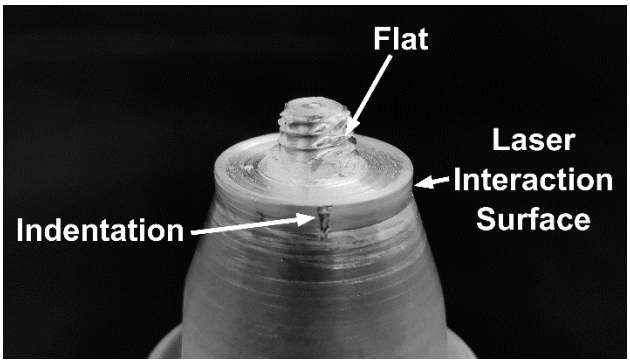

Figure 25: Profile of friction stir tools utilized in both toolholders

5.2.3 Laser Vibrometer Setup:

Welding was performed by translating the workpiece and the fixture (attached to the mill table) in the Y-direction through the stationary rotating tool, which allowed the vibrometer to be focused on the tool. The vibrometer was positioned perpendicular to the weld travel direction on the advancing side of the weld as depicted in Figures 23 and 26. The laser vibrometer was able

to capture the motion of the tool during welding between the two toe clamps on the advancing side of the fixture. The welds were programmed such that the table moves 130 mm in the Y direction to create a 130 mm weld. The vibrometer was able to capture the tool motion during the 90-105 mm section of the weld length within the line of sight between the toe clamps. Prior to testing, the laser beam had to be aligned with the tool shoulder surface (at its position during the weld section of interest) in three-dimensional space. Starting with a level vibrometer, the vertical position of the vibrometer was raised to align the beam on the center of the laser interaction surface (Figure 25). In the X-direction, the beam was manually focused to provide a beam spot diameter of 1 mm on the interaction surface to produce a bulk motion measurement of the tool as opposed to changes in micro imperfections in the surface. The Y-position of the beam was adjusted while capturing data until the velocity measurements oscillate around a value of zero. Oscillations around an average positive or negative value would be produced if the beam was not centered on the tool in the Y-dimension (non-physical). The Polytec PSV 400 velocity scale setting was set to “VD-07” (5 mm/s/V), all filters were turned off, and the bandwidth value was set to 0.5 kHz with 6400 FFT lines. These specific parameters allowed for 12.8 seconds of data to be captured at a sampling rate of 1.28 kHz.

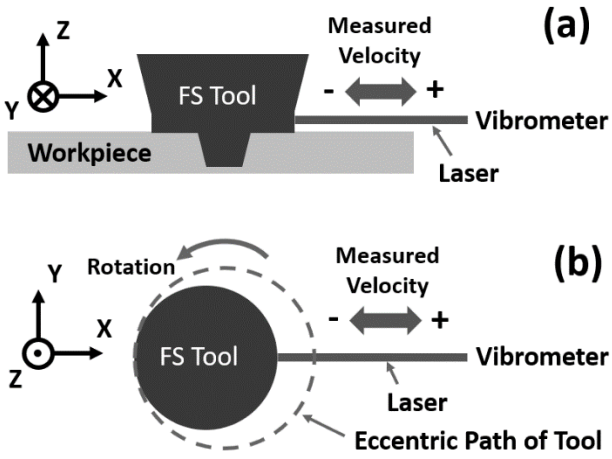

Figure 26: Schematic of the laser measurement process during welding

5.2.4 Procedure

The natural eccentric motion of both free spinning toolholder setups was collected while rotating freely at 1,000 rpm both before and after all welding tests. Three welds were performed at a rotational rate of 1,000 rpm and 200 mm/min to produce welds with no void interaction. Eight defective welds (that resulted in sub-surface void interactions) were performed at 1,000 rpm and travel speeds ranging from 500 to 850 mm/min in increments of 50 mm/min for each toolholder setup totaling 16 void conditions. All welds were performed as a bead on plate weld, and with a 3-degree travel angle. An axial shoulder plunge depth of 0.2 mm was programmed at the center of the shoulder for the 6 non-void interaction conditions, and a plunge depth of 0.35 mm was programmed for the 16 defective welds. The programmed values of plunge depth at the center of the tool shoulder result in the center of the tool shoulder residing near the top surface of the workpiece during welding due to the compliance of the system. All workpieces were 6061-T6 aluminum and were 200 mm long, 100 mm wide, and 6.35 mm thick. Prior to starting the force/encoder data acquisition system, the indentation in the laser interaction surface was set to the far advancing side of the process, *i.e.*, 90 degrees from the travel direction. This set a zero point in the encoder data so that the angular position of the indentation, as well as the flats and most eccentric point of the tool, can be resolved throughout the welding force data. During welding, the vibrometer data acquisition was started when the laser reached the line-of-sight gap between the two toe clamps.

Post welding, all tool velocity data was converted to both position and acceleration data using either the cumulative trapezoidal numerical integrator function “cumtrapz” in MathWorks MATLAB to produce a position signal, or numerical differentiation function “diff” in MathWorks MATLAB to produce acceleration. The dynamometer force signal and the vibrometer motion signal were aligned in the time domain globally by using the 105 mm weld position as a reference point in both data streams. At 105 mm into the weld, the laser hit the fixture (second toe clamp) resulting in a momentary spike in the velocity data. The 105 mm point in time in force data was

found based on a linear interpolation from the start time of the weld (spike in the travel direction force) to the end time of the weld (drop in the travel direction force). The force and velocity measurements were synchronized locally within one revolution using the encoder measurement of the indentation on the laser interaction surface of the tool. The indentation produced a distinct disruption in the vibrometer measurement that can be linked to the exact point in the encoder/force data corresponding to when the angular position of the indentation is at the advancing side position where the laser was focused on the tool. More details on the indentation effect can be found in the supplemental material file. Five cycles of the synchronized force and motion signals (taken around the 100 mm point in both data streams) were analyzed in combination. The frequency content (amplitudes at harmonics) was extracted from the acceleration signal via a Discrete Fourier Transform and the corresponding force data was used as an input to a MathWorks Simulink model described in further detail in Section 5.2.7.

5.2.5 Measurement of System Stiffness:

The static stiffness of the toolholder/spindle side of the system in the direction of interest (X-direction) was determined by incrementing the CNC mill table in the X-direction in order to move the dynamometer fixture into contact with the side of the friction stir tool probe. After starting the force data acquisition system, the dynamometer was incremented into the tool probe while the deflection of the tool (in the X-direction) driven by the dynamometer was measured by a dial indicator that was fixed to a separate static structure. Ten stiffness tests were performed on each toolholder setup (1 and 2) by deflecting the tool to distances ranging between 100 to 200 µm while recording the total change in force. Additionally, ten tests were performed by deflecting the CNC mill spindle without a toolholder in it to get the stiffness of the machine spindle itself. Additionally, the procedure was repeated in the Y-direction for both toolholders.

5.2.6 Measurement of System Natural Frequency:

The natural frequency of the tool-side of both toolholder systems was determined by applying an impulse to the side of the tool shoulder by means of striking it with a dead blow hammer and measuring the subsequent motion of the tool with the laser vibrometer focused on the tool shoulder. This action was performed in the X-axis direction. The region of interest of the motion response shown in Figure 27 was processed with a Fast Fourier Transform to determine the dominant frequency that the system vibrated at. Five impulse tests were performed for each toolholder setup.

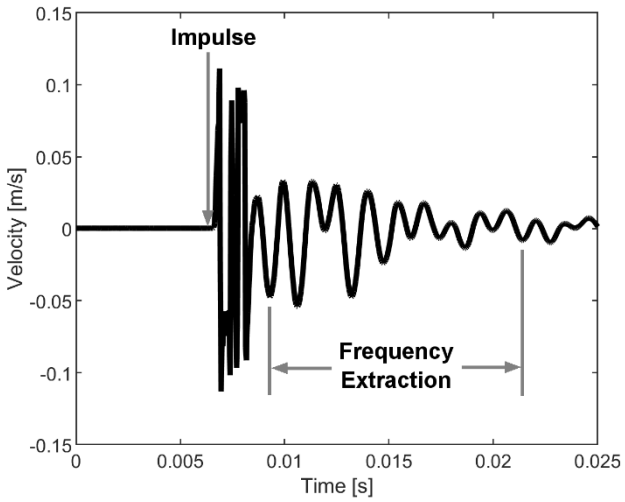

Figure 27: Impulse response of tool in the X-direction captured with vibrometer

5.2.7 Implementation of the Mass-Spring-Damper Model:

Dynamic modeling of the mass-spring-damper systems was implemented in MathWorks Simulink. The motion of the tool was modeled for all welds performed with both toolholder setups. A standard one-dimensional mass spring damper block diagram (Figure 28) was used. The measured force data that the tool applies to the workpiece in the X-direction was inverted to represent the reaction force that the workpiece applies to the tool. The section of force data corresponding to the weld region where the vibrometer acceleration was processed by the Discrete Fourier Transform was utilized as the input force. Seven force cycles corresponding to

the seven tool rotations that spanned the 100 mm weld length position were inputted into the block diagram as the forcing function. The relevant mass (*m*) and spring constant (*k*) estimated from data described in Sections 5.2.5 and 5.2.6 were loaded into the Simulink model along with a relevant damping coefficient (*b*). The damping coefficients examined in Simulink ranged from the maximum value reported in end milling literature (500 Ns/m) to ten times that value (5,000 Ns/m). All Simulink simulations were performed using a variable step 4th order Dormand-Prince solver (Simulink: “ode45”) where the maximum time step was set to 0.001 s, with a relative tolerance of 0.001, and zero-crossing detection enabled. The full list of Simulink parameters is contained in the supplemental material file. The seven force cycles used as the forcing function resulted in seven output motion cycles. Within the seven cycles, the first two were ignored due to nonphysical initialization (moving to the average position value due to the average force), and the last five were used for comparison with the measured tool motion.

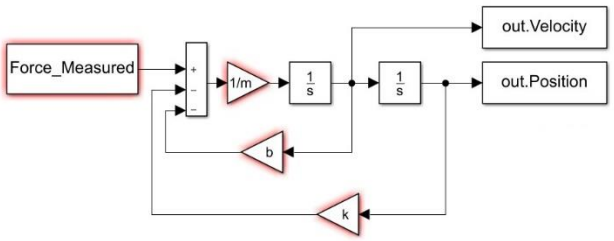

Figure 28: Standard mass-spring-damper Simulink block diagram

5.2.8 Three-Dimensional Finite Element Modeling of Void Interaction:

A numerical simulation of the friction stir welding process was setup and solved in ABAQUS 6.16 in explicit solver, using a Coupled Eulerian-Lagrangian (CEL) governing equations framework. The material model (Johnson Cook), contact, boundary conditions, and other model assumptions were the exact same as the model setup used in prior work by Ansari *et al.* The specific goal of the current formulation of the simulation is to examine the reaction force and tool displacement analysis for the defect/probe feature interaction examined in the experimental work. The 3D numerical model was designed around the experimental

components described in Section 5.2.2, specifically with the measured properties (tool runout and stiffness) characteristic of the Toolholder 1 setup. Shown in Figure 29 (a) is the 3D Eulerian domain with a volume of 20×20×7 mm^3, which was meshed with 23016 thermally coupled Eulerian elements (EC3D8RT) with a size of 0.5 mm and having 4 degrees of freedom per node. Eulerian domain included two main regions: The blue part (full region) was assigned to the aluminum alloy with a thickness of 6 mm and the 1 mm thick red zone (empty region), where no material was assigned in order to allow flash to form above the surface of the workpiece during welding. The meshed friction stir tool and tool dimensions are presented in Figure 29 (b). The tool is modeled using Lagrangian rigid body formulation consisting of 23522 4-node thermally coupled tetrahedron (C3D4T) elements with a size of 0.6 mm. The simplified tool was modeled with a three-flat straight probe using the average diameter of the experimental probe and without threads in order to make the simulation more computationally efficient. The plunging stage of the process was not modeled to also aid in computational efficiency. This means that the initial startup of the process is non-physical. To avoid any overestimations due to the non-physical startup, the numerical results were only investigated when the process's X and Y forces reached a steady-state condition.

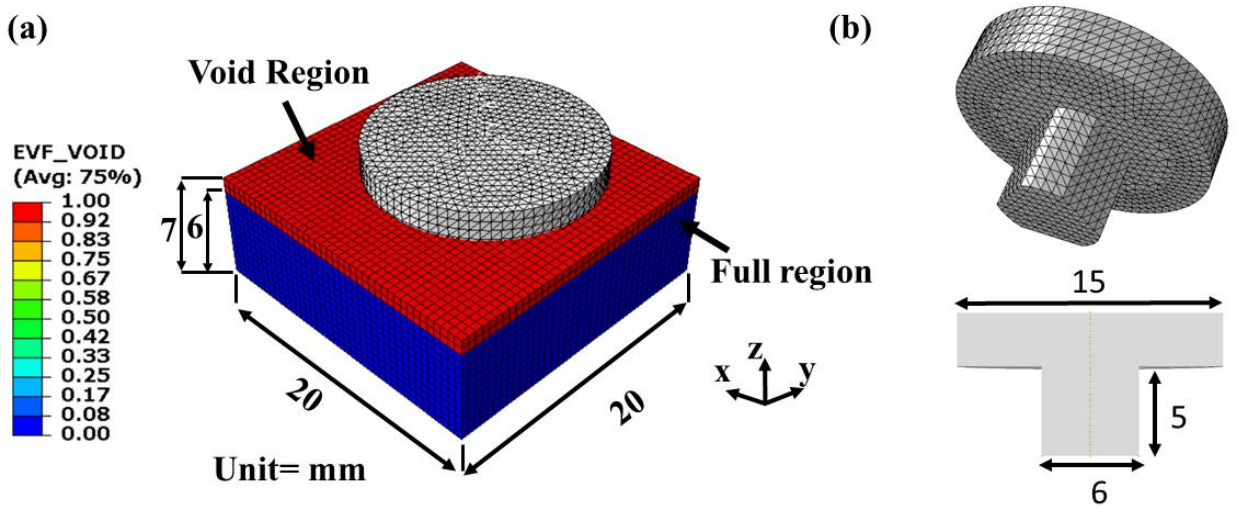

Figure 29: Numerical mesh and geometrical description: (a) the workpiece domain, and (b) the friction stir tool.

Tool runout was implemented into the simulation by offsetting the body of the tool from a reference point around which the tool rotated at 1000 rpm. The body was offset 32 µm in order to achieve the true runout value of 64 µm that was measured for Toolholder 1 (Figure 30 (b)). System compliance was implemented through the addition of linear spring elements between the reference point of the tool body and three fixed points in the X, Y, and Z directions (Figure 30 (a)). Since the eccentric motion of the tool occurs in the X-Y plane, the spring element in the Z direction was set to an infinite value to isolate the deflection of the tool in the plane of welding. The stiffness of the spring elements X and Y direction are set to the values determined in Section 5.2.5 (6.15 MN/m and 8.3 MN/m respectively). The welding action is simulated by passing the workpiece material through the Eulerian domain. This is achieved by setting the inflow and outflow velocities of the domain to the travel speed of the process (Figure 30 (b)), specifically 600 mm/min in this case. All other exterior domain surface velocities are set to zero to prevent material from passing through.

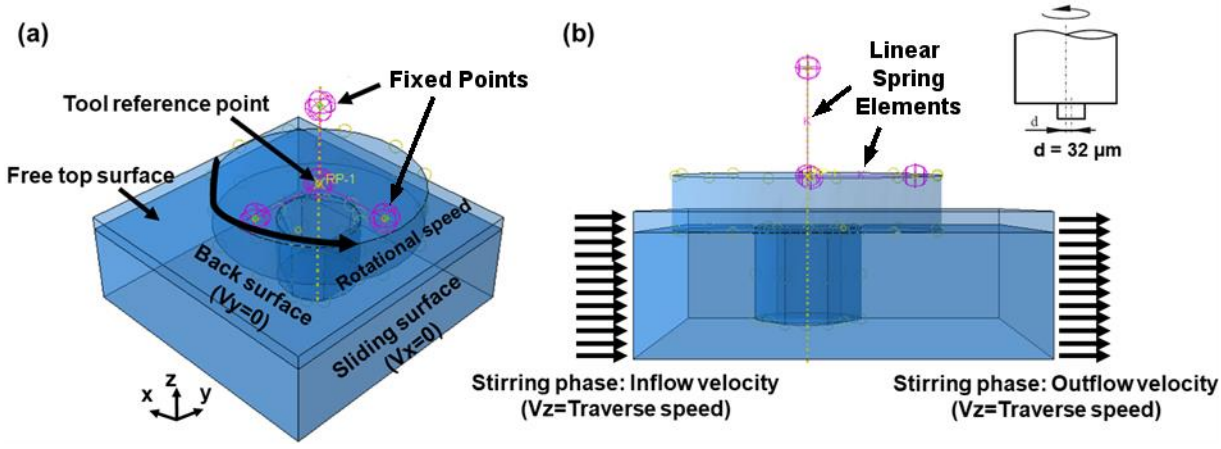

Figure 30: Simulation setup and boundary constraints

5.3 Results and Discussion

5.3.1 System Stiffness:

The average and standard deviation of static stiffness tests of each toolholder system as well as the machine spindle without a toolholder are reported in Table 4. The values are

reported only for the direction of interest (X direction). Toolholder 2 had a system stiffness of approximately half of Toolholder 1 because it was almost twice the length as Toolholder 1 and both are cantilevered beams extending from the machine spindle. The reported stiffnesses are on the same order of magnitude of similar systems in both end milling and friction stir welding applications ranging from 2.6 to 18 MN/m [47, 48, 52]. The measurement of the machine spindle alone allows for the determination of the lateral stiffness of each toolholder itself by means of *Equation (2)*. Using *Equation (2)*, the stiffness of Toolholder 1 alone was determined to be 8.6 MN/m, and for Toolholder 2, 3.1 MN/m. This suggests that the full stiffness of the tool-side system was primarily driven by the more compliant toolholder as opposed to the stiffer machine. For example, given Equation 2, an infinitely stiff machine would still result in a system stiffness of only 8.6 MN/m when combined with Toolholder 1. This is relevant because many dedicated friction stir welding machines are stiffer than the milling machine used in this study, but many friction stir welding toolholders are long and narrow in order to fit between workpiece clamps, *i.e.*, compliant in terms of beam bending. This suggests that it may be common that compliance of the toolholder (as opposed to machine) would determine system stiffness in the plane of welding where the examined tool motions occur (X-Y directions) in many friction stir welding applications. It is hypothesized that the opposite is true in the axial (Z) direction because a similar toolholder may be stiffer than the machine in the axial direction as it is not cantilevered in the axial direction.

Table 4: Measured stiffness of both toolholder systems and the machine spindle alone

	X-Direction Stiffness [MN/m]
Machine Spindle	21.4 ± 3.1
Full System: Toolholder 1	6.15 ± 0.42
Full System: Toolholder 2	2.68 ± 0.10

5.3.2 System Natural Frequency and Effective Mass:

The natural frequencies of Toolholder Systems 1 and 2 were determined from impulse testing (Section 2.3.2) to be 745 ± 2 Hz and 282 ± 4 Hz respectively. The natural frequencies are within the range of natural frequencies reported in literature for similar experimental setups on similar machines in both end milling and friction stir welding applications ranging from 60 to 1800 Hz for systems with stiffnesses ranging from 2.8 to 18 MN/m [47-50, 52]. Within this range, machines with larger stiffness have a higher corresponding natural frequency. The stiffnesses of the two toolholder systems match well with their corresponding natural frequencies when considering both stiffness and natural frequencies within the ranges reported in literature. The natural frequency of the Toolholder 1 system was approximately double the natural frequency of the Toolholder 2 system because the stiffness was approximately double.

The stiffness and natural frequency of each toolholder system were used to calculate an effective mass of the system via *Equation (3)*. The effective mass of Toolholder systems 1 and 2 were 0.28 ± 0.02 kg and 0.85 ± 0.06 kg respectively. The effective mass represented the mass of the toolholders that would move under an applied force given the cantilevered nature of the toolholder. The effective cantilevered mass should be less than the total mass of each toolholder when weighed on a scale, which was 2 and 5 kg respectively for Toolholders 1 and 2.

5.3.3 Force and Displacement

Chapter 4 has shown that the laser vibrometer system can accurately capture the tool motion of interest and that the eccentric motion of the tool due to its natural runout is constrained during welding. In the current Chapter, an updated experimental setup utilized tools that had distinct indentations in the laser interaction surface that allowed the laser vibrometer motion measurement to be synchronized in time with the force dynamometer measurement using an angular encoder. Figure 31 (a) illustrates an example of the difference between the free spinning natural runout of the tool and the constrained eccentric motion of the tool during a

welding condition with no void interaction (fully consolidated weld). The difference is calculated as the subtraction of the welding tool position signal from the free-spinning position signal at every point in time. The difference in the two position signals is due to the force that the material applies to the tool during welding. The difference in the position signals in the X-direction is plotted in the same timing scheme as the force signal in the X-direction that the workpiece applies to the tool in Figure 31 (b).

It was observed that the oscillation (once per tool revolution) in the difference in the position signal is in phase with the oscillation in the force applied to the tool (once per tool revolution). When examining all welds performed with both toolholder systems in the fully consolidate dwelling conditions, the difference in phase between the position difference signal and the force signal was consistently less than 8 degrees. The minor difference in phase suggests that the stiffness of the system governs the motion of the tool at the rotational frequency that is driven by the process interaction force. If there was a significant phase difference in the signals, it would suggest that a non-linear effect such as damping is occurring. This was examined further by plotting the force signal versus the position signal as shown in Figure 31 (c). It was observed that there is a direct linear relationship between the force and position signal within one revolution. The average slopes of the linear relationships (Figure 31 (c)) for all fully consolidated welds were determined to be 6.3 ± 0.7 MN/m for Toolholder 1 and 3.2 ± 0.6 MN/m for Toolholder 2. These values showed good agreement with the measured stiffness values reported in Section 3.1. This appears to confirm that the stiffness of the system governed tool displacement at the tool rotational frequency during welding. It also suggests that a stiffer system will prevent the process forces from displacing the tool from its natural eccentric path (runout) during welding. This would allow more available runout of the tool to occur in-process, which has been shown to affect material flow [40].

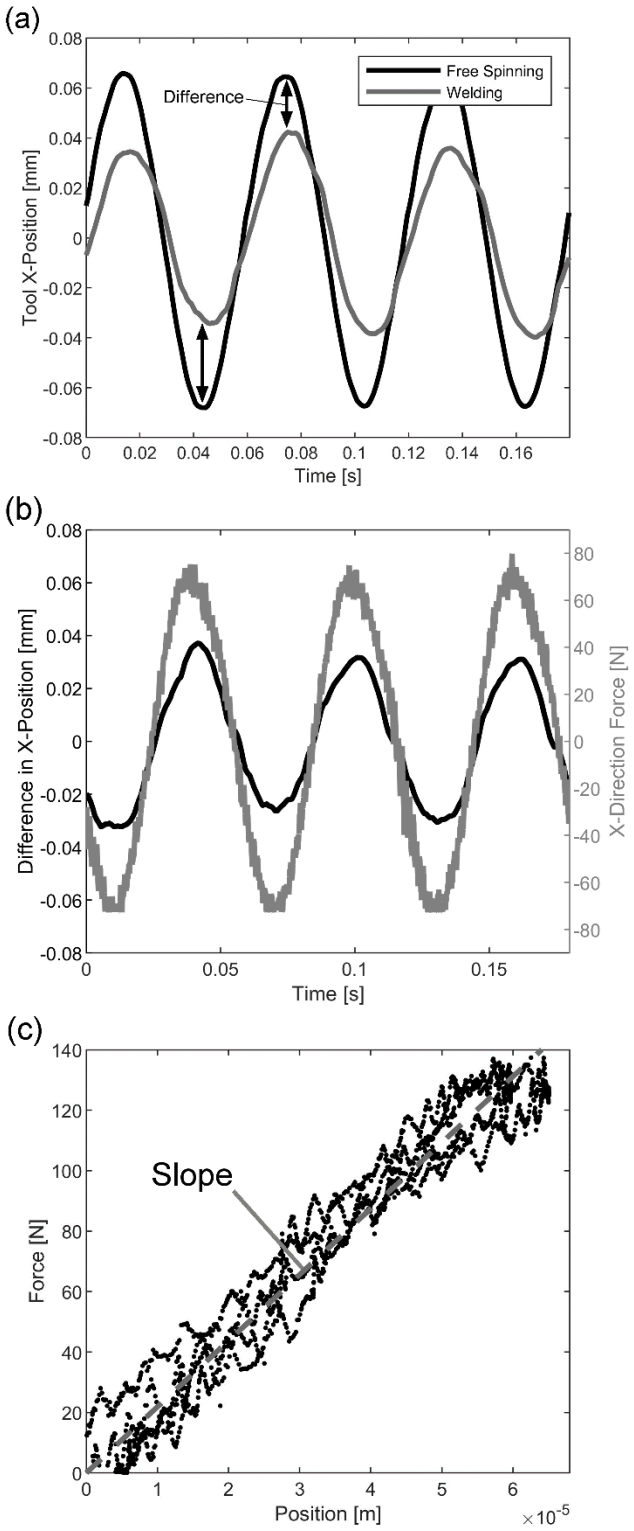

Figure 31: The synchronization of force and tool displacement in the X-direction: (a) the difference of the tool position during welding from the tool's natural free spinning amplitude, (b) difference in position plotted in the same time scheme and the force, (c) force plotted versus displacement over several revolutions.

Distinct interactions between two of the peaks in between the three flats on the tool probe and void volumes occur when substantial sub-surface voids are formed. The interactions are resultant of a change in contact pressure between the material and tool that result in a momentary deflection of the tool into the void volume which corresponds to a reduction in the oscillatory process force that the eccentric motion of the tool applies to the workpiece. The synchronization of the tool motion measurement and the interaction force measurement allowed for the examination of the displacement of the tool in the X-direction with respect to the force applied to the tool in the X-direction during void interaction as exemplified in Figure 32. The position signal shown was calculated in the same manner as the difference in position shown in Figure 31 (b). It was observed that for all the void interaction welding parameters studied, the two distortions per revolution in both the force and position signals also have minimal difference in phase when examining the two signals within the same timing scheme. The observation that the distortions in both signals occur simultaneously supports the fundamental link between the amplitude in the third harmonic in the tool position and interaction force proposed in Chapter 4. Additionally, the observation that the force and displacement are in phase with each other suggests that the dynamics of the system at three times the tool rotational frequency are also governed primarily by the stiffness of the system as opposed to damping. This observation will be examined in greater depth in Section 5.3.4.

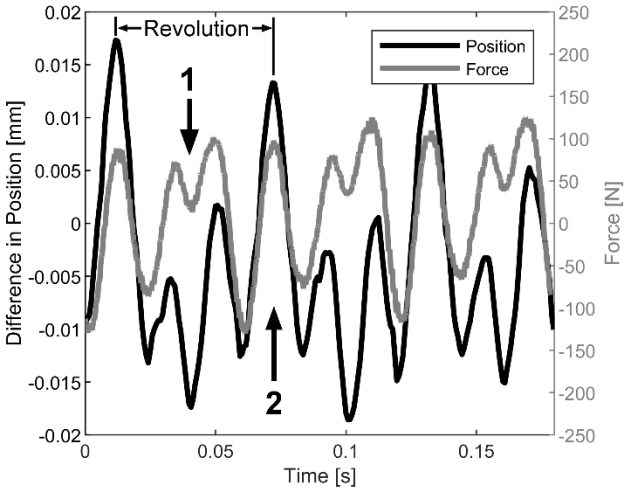

Figure 32: Synchronization of tool displacement and interaction force in the X-direction

5.3.4 Friction Stir Tool Acceleration:

The objective of the current work is to develop a fundamental understanding of the relationship between the process interaction forces and the motion of the tool. This understanding will inform the development of accelerometer measurement based void monitoring methods. It has been hypothesized that a simple mass-spring-damper model can form the basis of this understanding. The hypothesis was examined through the comparison of the tool motion predicted by the mass-spring-damper model (driven by measured interaction force) and the tool motion measured via the laser vibrometer. The tool acceleration during void interaction was the parameter of interest in this study since it will be the measured value when utilizing an accelerometer.

It was observed that the primary amplitude in the acceleration signal derived from the vibrometer measurement was at three times the tool rotational frequency during all the void interaction welding conditions studied. An example of the acceleration signal during void interaction is shown in Figure 33 (a), where the amplitude of the signal at three times the tool rotational frequency is on the order of 1.8 m/s^2. In all void interaction welding conditions studied, the amplitude of the acceleration signal at three times the tool rotational frequency was in the range of 0.6 to 3 m/s^2. These amplitudes can be compared to the nominal acceleration

amplitudes of the tool at the rotational frequency due to its natural runout during a non-void interaction welding condition, *i.e.* the associated acceleration of the tool corresponding to the motion shown in Figure 31 (a), which is on the order of 0.3 m/s^2 for both Toolholders 1 and 2. This suggests that when examining the frequency content of the acceleration signal, the acceleration of the tool into void volumes during the feature interactions dominates the nominal acceleration due to the bulk eccentric motion of the tool (for the magnitudes of runout considered). Based on prior work that focused on frequency content of force and position signals and void size (Chapters 2, 3, and 4), it is hypothesized that the amplitude of the component of the acceleration signal at three times the tool rotational frequency (3rd harmonic) will provide the strongest correlation with void size when developing a monitoring method utilizing an accelerometer.

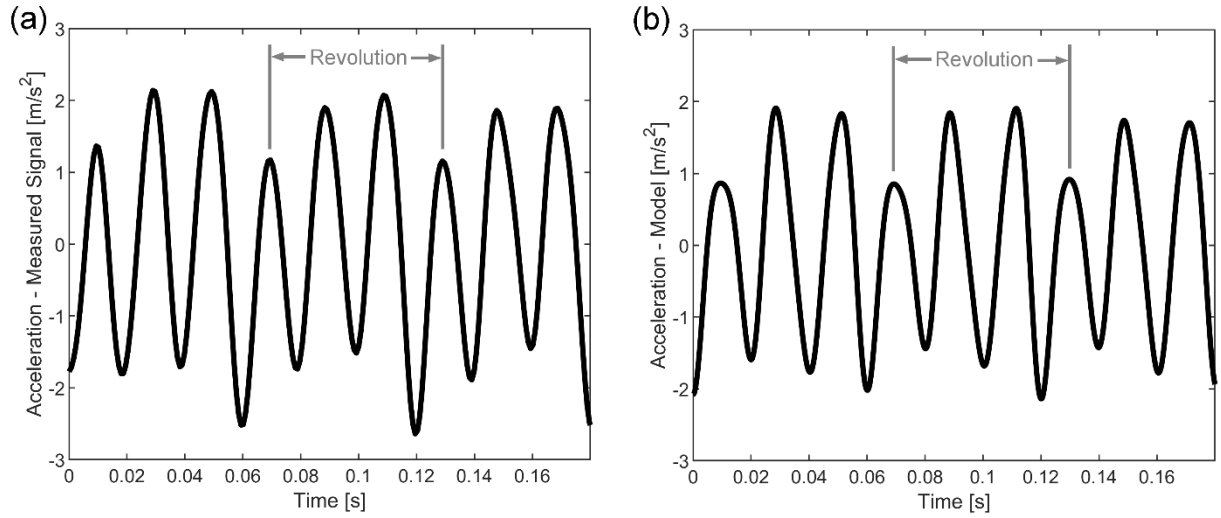

Figure 33: Three tool rotations of the vibrometer measured (a) and Simulink modeled (b) tool acceleration during subsurface void interaction for the same section of weld data. Note that the signals have been filtered (low-pass-filter at 100 Hz) in order to isolate the motion of the tool at the frequency of interest.

The hypothesis that a simple mass-spring-damper model can provide a fundamental understanding of tool-side dynamics was tested by comparing the acceleration signal derived from the Simulink model to the acceleration signal derived from the laser vibrometer measurement. Shown in Figure 33 (b) is an example of the acceleration signal derived from the Simulink output corresponding the section of weld from which the measured acceleration is

shown in Figure 33 (a). Both the measured and modeled acceleration signals oscillate primarily at three times the tool rotational frequency and have good agreement in term of the value of the amplitude at that frequency. The model's ability to predict the amplitude at the third harmonic in the acceleration signal was tested over a range of welding conditions for both toolholder setups with different stiffnesses. The range of welding parameters were produced with an increasing amount of tool advance per revolution in order to generate larger voids that produce larger distortions in process signals. A discussion on the relationship between the amplitude of the third harmonic in the measured motion signal and measured void area is presented in Chapter 4.

The relationship between the measured amplitude at three times the tool rotational frequency and the modeled amplitude at three times the tool rotational frequency within the acceleration signals for a range of void interaction conditions is shown for both toolholder setups in Figure 34. It was observed that the amplitude at the third harmonic in the modeled acceleration grew with the measured amplitude in the acceleration at a ratio close to 1:1 (dotted line on plot represents a slope of 1). This suggests that the model can capture the change in acceleration across the range of void interactions encountered. Additionally, the model was able to accurately account for the approximate factor of 2 difference in stiffness of the two toolholder setups. Note that stiffness has a linear effect on the output motion of the model. The vertical error bars are the uncertainty in the modeled amplitudes which were determined by modeling the upper and lower bounds of the uncertainties on stiffness and mass values reported in Sections 5.3.1 and 5.3.2. This uncertainty was dominated by the uncertainty in the stiffness measurement as the stiffness was considerably larger than the mass of the system. The horizontal error bars are the error associated with the vibrometer measurement which was estimated based on the alignment of the laser. The full description of the estimation of the error associated with laser alignment is contained in the supplemental material file.

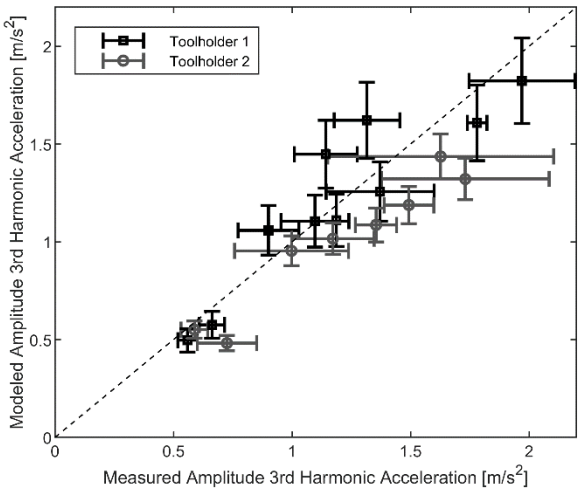

Figure 34: Comparison of the amplitude of the third harmonic of the acceleration signal derived from the vibrometer measurement and the third harmonic of the acceleration signal derived from the Simulink output across a range of void interaction welding conditions

5.3.5 Examination of Damping Coefficient:

The determination of the damping coefficient is a critical component of modeling the motion of a cutting tool in an end milling application since the occurrence of chatter occurs at a frequency near the natural frequency of the system. In the case of the friction stir welding process, the frequency of interest due to the void interaction is determined by the number of flats on the tool probe and the rotational frequency (both set by the user). The rotational rate used in all tests discussed in Section 5.3.4 was 1,000 rpm and there were three flats on the tool probe (3rd harmonic) which correlates to a frequency of interest of 50 Hz. As determined in Section 3.2, the natural frequencies of the two toolholder setups are 745 Hz and 282 Hz respectively, which are approximately an order of 15 and 6 times greater than the frequency of interest. Given that damping tends to have an effect when the frequency of interest is near the natural frequency of the system, it was hypothesized that damping would have a small effect on the motion of the tool during void interaction at 50 Hz. The damping coefficient was varied in the Simulink model and amplitude at the third harmonic (50 Hz) in the acceleration signal was examined. An example of the relationship between the amplitude and damping coefficient for two selected welds (one with each toolholder) that had similar vibrometer measured amplitudes

(1.1 m/s^2) is shown in Figure 35. A difference in the amplitude on the order of 8-13% was observed when altering the damping coefficient from the largest value reporting in end milling literature (500 Ns/m) to ten times that value. The difference tended to be slightly larger for Toolholder 2 since the natural frequency is closer to the frequency of interest. The minimal change in amplitude, given the substantial factor of 10 difference in damping coefficient supports the hypothesis that the damping in not relevant to the dynamics of the tool for the welding parameters studied.

The results also suggest that the damping coefficient that produced the best agreement with the vibrometer measured motion is on the order of 1000 Ns/m, which is approximately twice the highest value reported in end milling literature. It was expected that the damping coefficient would be larger in friction stir welding than in end milling because process damping is dependent on the amount of engagement of the tool and workpiece. A friction stir welding tool has substantially more engagement with the workpiece than an end mill given that it is surrounded by the plasticized workpiece. Process damping has the potential to become relevant to the dynamics of the tool if the frequency of interest becomes closer to the natural frequency of the system. This would be resultant of the frequency of interest becoming larger (*e.g.,* higher rotational speeds), or the natural frequency of the system becoming smaller (*e.g.,* larger effective mass of the system or lower stiffness).

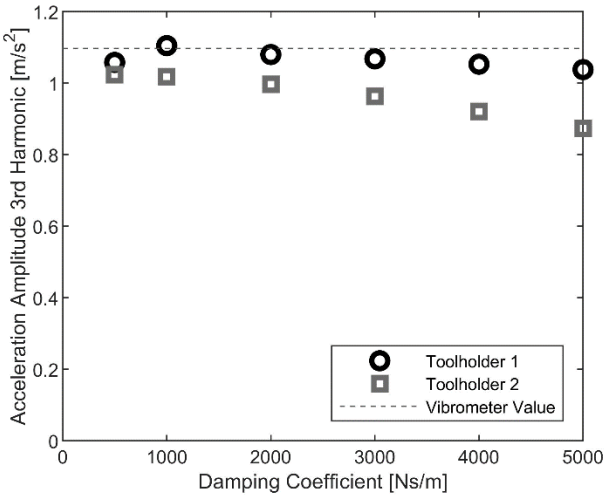

Figure 35: Relationship between the input damping coefficient and Simulink modeled amplitude at the third harmonic for two similar welding conditions with both toolholder setups. The outputs are compared to the corresponding vibrometer measured amplitude.

3.5.2 Tool Rotational Speed and Acceleration:

Void interaction conditions were tested with increasing rotational speed and consistent tool advance per revolution in order to examine the relationship between the rotational speed of the tool and the amplitude of the acceleration signals during void interaction. The advance per revolution (ratio of rotational speed over travel speed) determines the volume of material that must be passed around the tool probe per revolution and therefore has a strong correlation with void size. Holding the advance per revolution consistent was the most readily available method of producing voids of similar size. Shown in Figure 36 is the acceleration signal derived from the laser vibrometer measurement for four welds where the tool advance per revolution was held constant at 0.6 mm while the rotational speed was varied between 800 and 1500 rpm. Cross-sections of the welds revealed that void sizes were consistent in terms of void area across the four welds. Additionally, the amplitudes at the third harmonic of the corresponding position signals for the four welds were all within the range of 10 ± 1 μm. As shown in Figure 36, the amplitude of the acceleration signal corresponding to void interaction increases (approximately linearly) with tool rotational speed. The void and probe feature (peaks between flats) interaction always occurred twice per revolution when utilizing a three-flat tool. Therefore, the time period in

which the two interactions must occur is determined by the tool rotational rate. As reported in Chapter 2, a larger void size resulted in a larger momentary deflection of the tool (change in position signal) for a constant rotational rate. The current results suggest that similar void sizes produced similar amounts of deflection (change in position), but since the deflection occurs in a shorter amount of time due to the higher rotational rate, the corresponding magnitude of the velocities and accelerations are larger. This suggests that tool rotational rate must be considered when developing a relationship between the amplitude of the third harmonic within a measured acceleration signal and the size of subsurface voids.

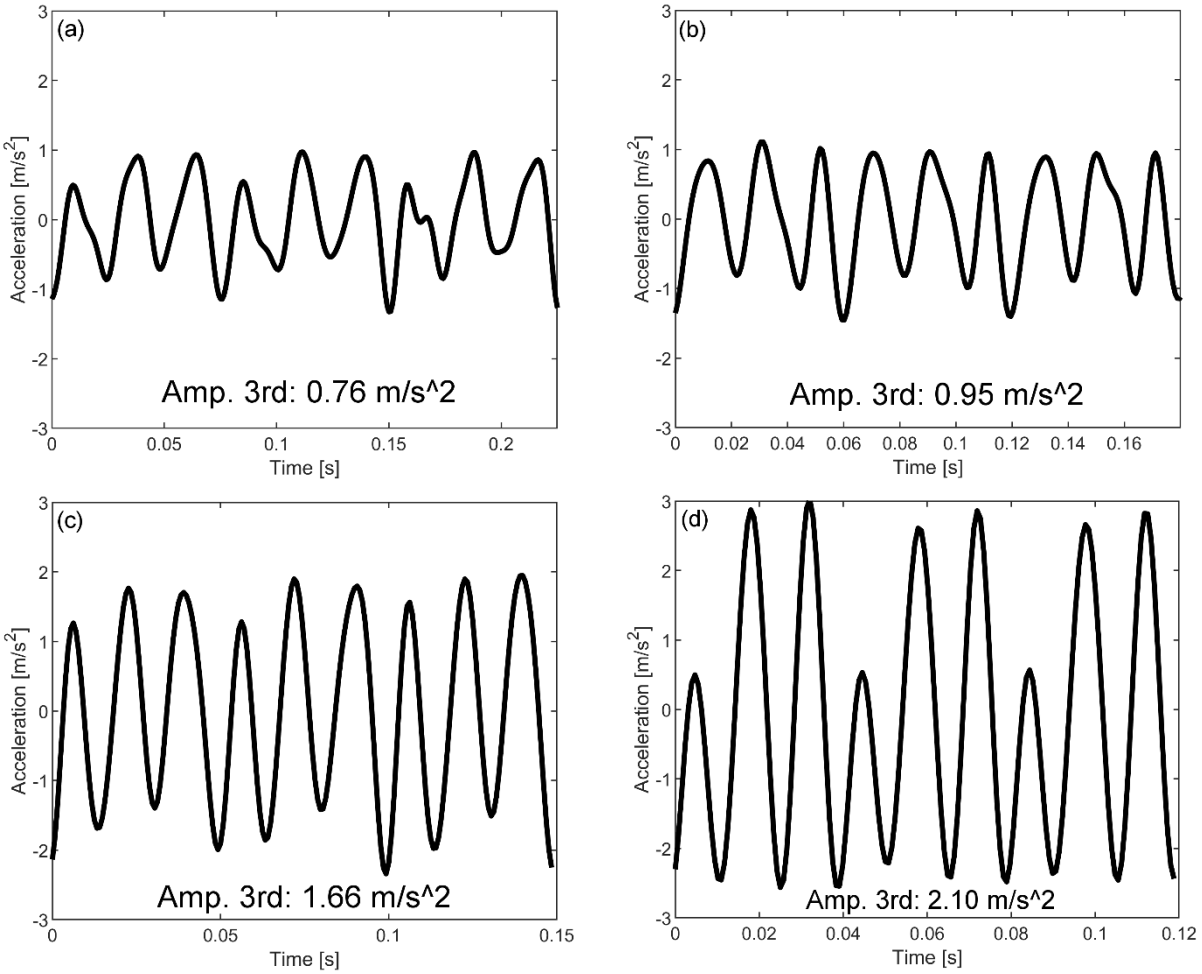

Figure 36: Acceleration signals derived form vibrometer measurements for welds performed at the same advance per revolution but varying spindle speeds: (a) 800 rpm (b) 1000 rpm (c) 1200 rpm (d) 1500 rpm.

5.3.6 Three-Dimensional Numerical Simulation of Void Interaction

The observation that the stiffness of the spindle system drives the tool dynamics allowed for the informed development of a numerical simulation where the stiffness of the system was added to the tool. The force applied to the tool in the X-direction, position of the tool in the X-direction, and the volumetric nature of subsurface voids were all extracted from the 3D finite element simulation once the simulation had reached a steady state in terms of the average process forces. One cycle of the force and position signals extracted from the simulation were compared to one cycle of the measured force and position from the corresponding welding condition (1000 rpm, 600 mm/min) performed with Toolholder 2 as shown in Figure 37. The addition of the eccentric motion of the tool in the numerical simulation generated an oscillation in the interaction force once per tool revolution that matches what was observed in the experimental measurement. Furthermore, the addition of the spring element allowed the tool to momentarily deflect into the void region when peaks on the tool probe interact with them. This resulted in two distortions per revolution within the numerical simulation force and position signals that agree well with the distortions captured in the experimentally measured values. This suggests that the numerical simulation can capture the physics of the interaction process. The simulation has the potential to be used as a tool to examine how different parameters (workpiece alloy, tool runout, system stiffness, etc.) alter the void interaction process and the resultant process signals.

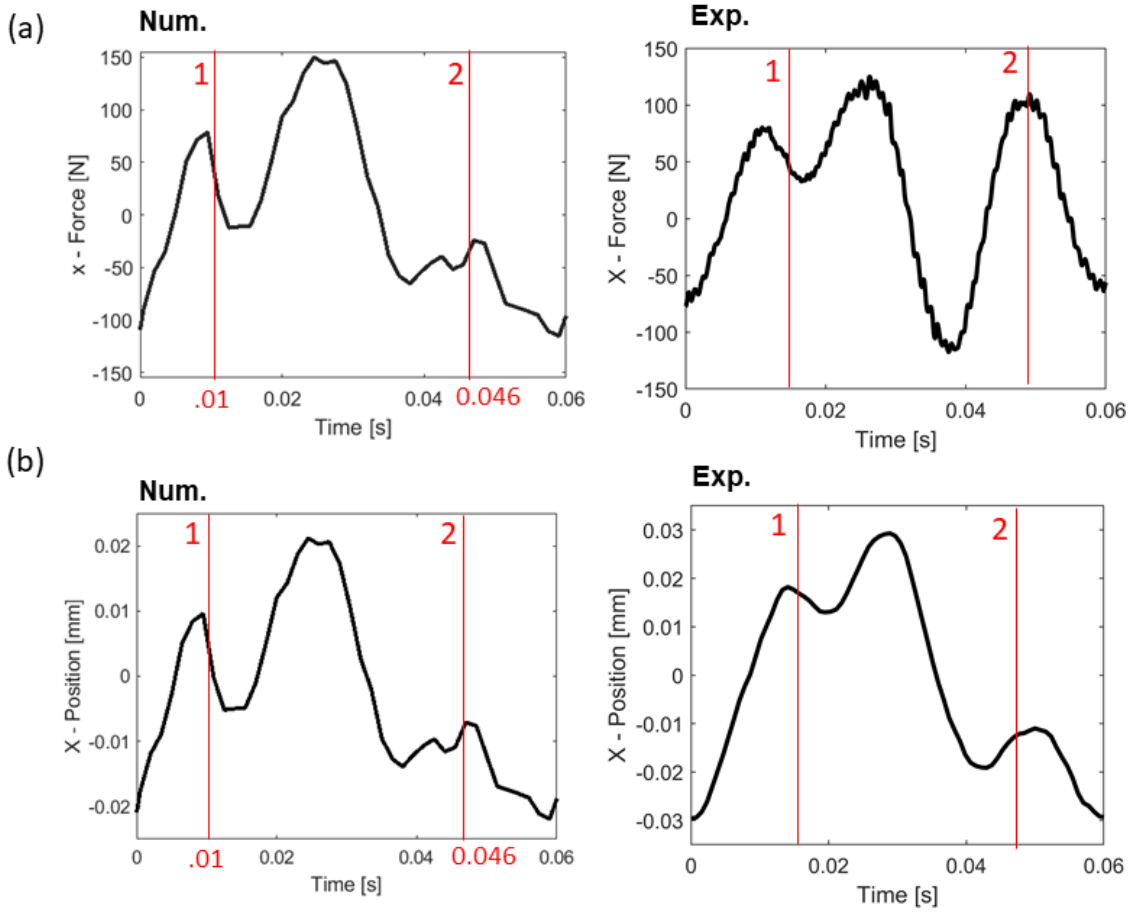

Figure 37: Comparison of numerical simulation extracted signals and measured signals for a 1000 rpm and 600 mm/min welding condition: (a) the numerical and experimental interaction force in the X-direction, (b) the numerical and experimental position in the X-direction. The two interactions of the probe features and voids are labeled 1 and 2.

Cross-sections (Figure 38) of the numerical domain at the void height were extracted from the numerical results at the two moments in time labeled in Figure 37. The numerical cross-sections illustrate the two interactions that occur per revolution that led to the signal distortions. The first interaction (Figure 38 (a)), occurs when the probe leading the most eccentric probe interacts with the void volume on the retreating side of the weld due to a lack of material flow around the retreating side. During this interaction, the tool moves towards the retreating side because the tool is nominally deflected towards the advancing side during welding due to the average process force in that X-direction, *i.e.*, the motion is a relaxing of the loaded spring that is nominally loaded by the average process force. During the second interaction (Figure 38 (b)), the tool moves towards the advancing side when the most eccentric

peak interacts with the void on the advancing side due to a lack in the equal and opposite oscillatory force (Chapters 2) that constrains the eccentric motion of the tool. The two interactions show good agreement with the description of the distortions in the force signals described in detail in Figure 8 based on measured force observations.

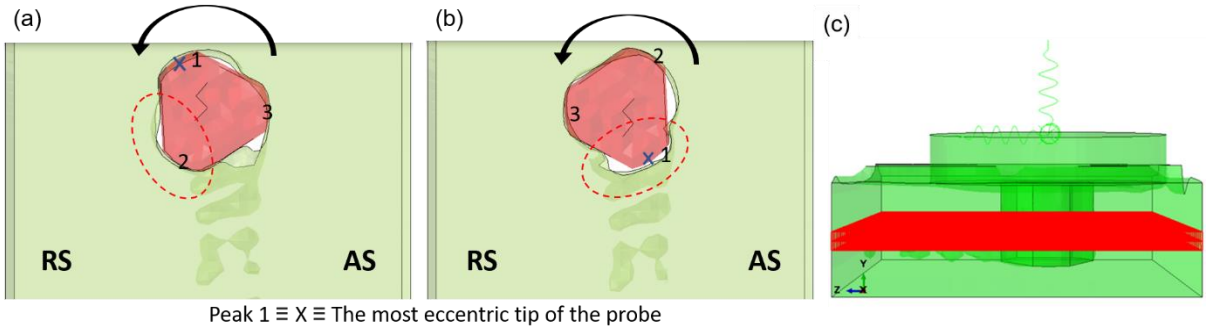

Figure 38: Examination of the interaction of peaks between the flats on the tool probe and void volumes in the numerical domain: (a) cross section corresponding to the simulation time of Interaction 1 labeled in Figure 37, (b) cross-section corresponding to Interaction 2, and (c) location of cross sections within the numerical domain.

5.4 Summary

A fundamental understanding of the tool side dynamics of a friction stir welding system was proposed. It was shown that a simple mass-spring-damper model can provide good initial agreement between predicted and measured tool motion (acceleration) during subsurface void interaction. This fundamental understanding will aid in the development of a more robust method of using tool acceleration measurements to sense subsurface void formation. The key outcomes of the current work can be summarized as follows:

- The dynamics of the tool-side of the friction stir welding system were driven by the stiffness of the system. This suggests that similar systems could be modeled simply as a spring.
- The stiffness of the tool-side of the system was driven by the stiffness of the toolholders themselves, as they were more compliant than the machine spindle. This suggests that toolholder design can be utilized to change tool motion during void interaction.

- Process damping had a minimal effect on the motion transients examined. It is hypothesized that this is due to the natural frequencies of the tool-side systems being substantially larger than the frequency of the void interactions, which was set by the number of features on the tool probe and the rotational rate.
- A 3D multiphysics numerical simulation of the process could predict the complex forces and tool motions during void interaction when applying simple linear spring elements to the tool side of the process.

The current work focused on the relationship between interaction force and tool motion. A fundamental understanding between void size and interaction force must also be developed in order to fully understand the relationship between void size and tool motion. The force applied to the friction stir tool was manifested through the change in contact pressure between the workpiece and the tool. A fundamental understanding of the pressure field must be developed in future work. It is hypothesized that the pressure field around the tool is dependent on the hot strength of the material being welded. Therefore, material dependence must be examined in future work as well.

Chapter 6: Development of Void Imaging at Argonne's Advanced Photon Source

One objective of this body of research is to achieve real-time imaging of the sub-surface void formation process during friction stir welding of aluminum alloys. To date, most experimental work on visual observations of the void formation process has been through post factum methods of observation such as tracer particles [53]. Post factum observations are limited in terms of the information they can provide on the full evolution of the defective volume as it forms. There has only been one study by Morisada et al. [54], that used real time X-ray imaging to capture the motion of tracer particles within the workpiece. However, the authors' method only captured the tracer particles within the material and not any subsurface void volumes directly. Therefore, this work seeks to provide novel insights as to how the sub-surface defective volumes form within one revolution of the tool by using real-time X-ray imaging of the void volume itself. This will provide critical insight into the morphological evolution of sub-surfaces defects that can be used to drive the numerical simulation of the void formation process. *In situ* imaging will be performed using the high-speed X-ray imaging apparatus at beamline 32ID-B at Argonne National Laboratory's Advanced Photon Source (APS). This beamline has been used for radiographical studies of other manufacturing processes such as powder bed fusion [55]. A schematic of the intended imaging process for friction stir welding is shown in Figure 39. The goal is to produce areal density images at the trailing edge of the FS tool probe. When a void volume is present the density of material in the transmission direction is less than the full section of aluminum and the change in density is captured in the areal density image.

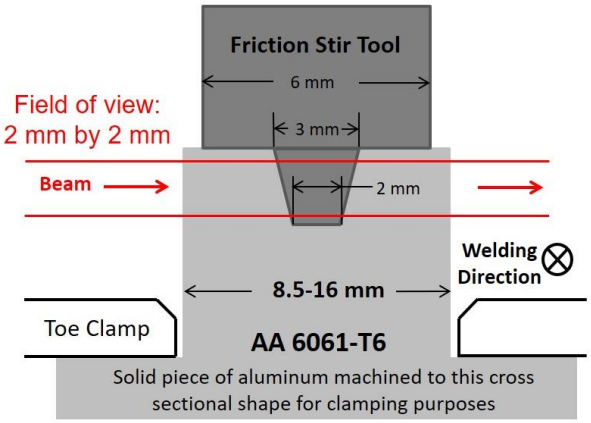

Figure 39: Schematic of the X-ray imaging process

Prior to performing full dynamic imaging, the feasibility of imaging cavities on the same order of size as the expected voids within the same thickness of material in the transmission direction must be proved. This was accomplished by statically imaging samples of the same thickness as future dynamic samples with missing volumes of material consisting of holes of known diameter drilled in the section, as well as voids created within welds in aluminum sections of interest. Figure 40 shows examples of the two types of static samples imaged. Samples were produced in three different thickness (8.5, 12, 16 mm) and three different aluminum alloys (3003-H14, 6061-T6, and 7075-T6). This will test the feasibility of imaging the process at different scales and in different alloys where defect formation mechanisms may vary.

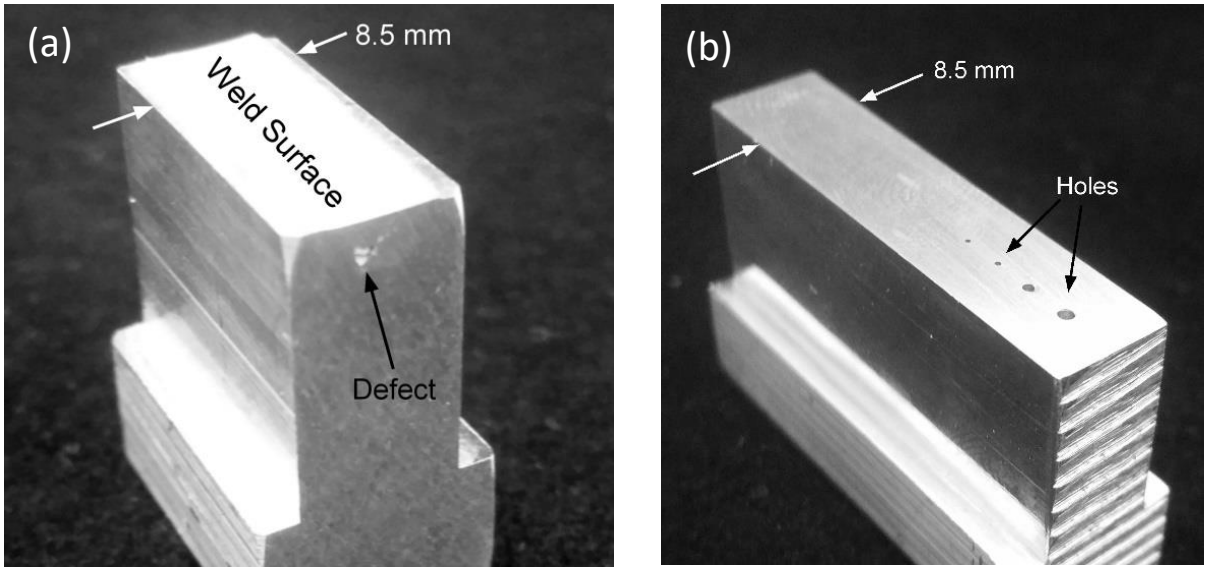

Figure 40: Two different types of static samples imaged (a) defects created in friction stir processed sections (b) holes of known diameter

4.1 Effect of Sample Thickness and Alloy Type on X-ray Transmission

Each of the three aluminum alloys examined have different alloying elements. Therefore, the effect of the alloying elements on X-ray transmission was examined. Aluminum 6061 has less than 0.5% of any alloying element that is heavier than aluminum itself, aluminum 3003 can have up to 1.5% Manganese (the only substantial heavier alloying element present), and aluminum 7075 can have up to 6.1% zinc (major alloying element heavier than aluminum). Heavier elements will be more resistant to transmission of the X-rays and adequate transmission is necessary to capture the form of defects within the aluminum sections. All static imaging was performed at a 20 kHz imaging rate with 49 microseconds of exposure and undulator gaps ranging from 13 to 17 mm. The undulator gap sets the power of the beam with thicker sections requiring smaller gaps (more power). Figure 41 shows selected results of areal density images captured during static imaging. Holes as small as 386 micrometers (smallest holes tested in 16 mm sections) were distinguishable in samples 16 mm thick of 3003 and 6061, and holes as small as 100 micrometers were distinguishable in 8.5 mm thicknesses. However, in 7075 the 386 micrometer holes could only be observed up to 12 mm of thickness. As shown in Figure 41 (c), the 16 mm sample was

too radiographically thick due to the up to 6.1% zinc present. In general, the thinner samples allowed more transmission, suggesting that imaging will be easier in the thinner sections. However, the FSW process tends to be utilized at size scales similar to or larger than the tool size that was used in the 16 mm thick section. Therefore, dynamic imaging will be performed within a range of size scales in order to examine how the defect formation process changes when different size tools are used. A thinner section will require that a smaller tool is used, *i.e.*, the tool size is designed as the maximum allowable that can be contained within the section width.

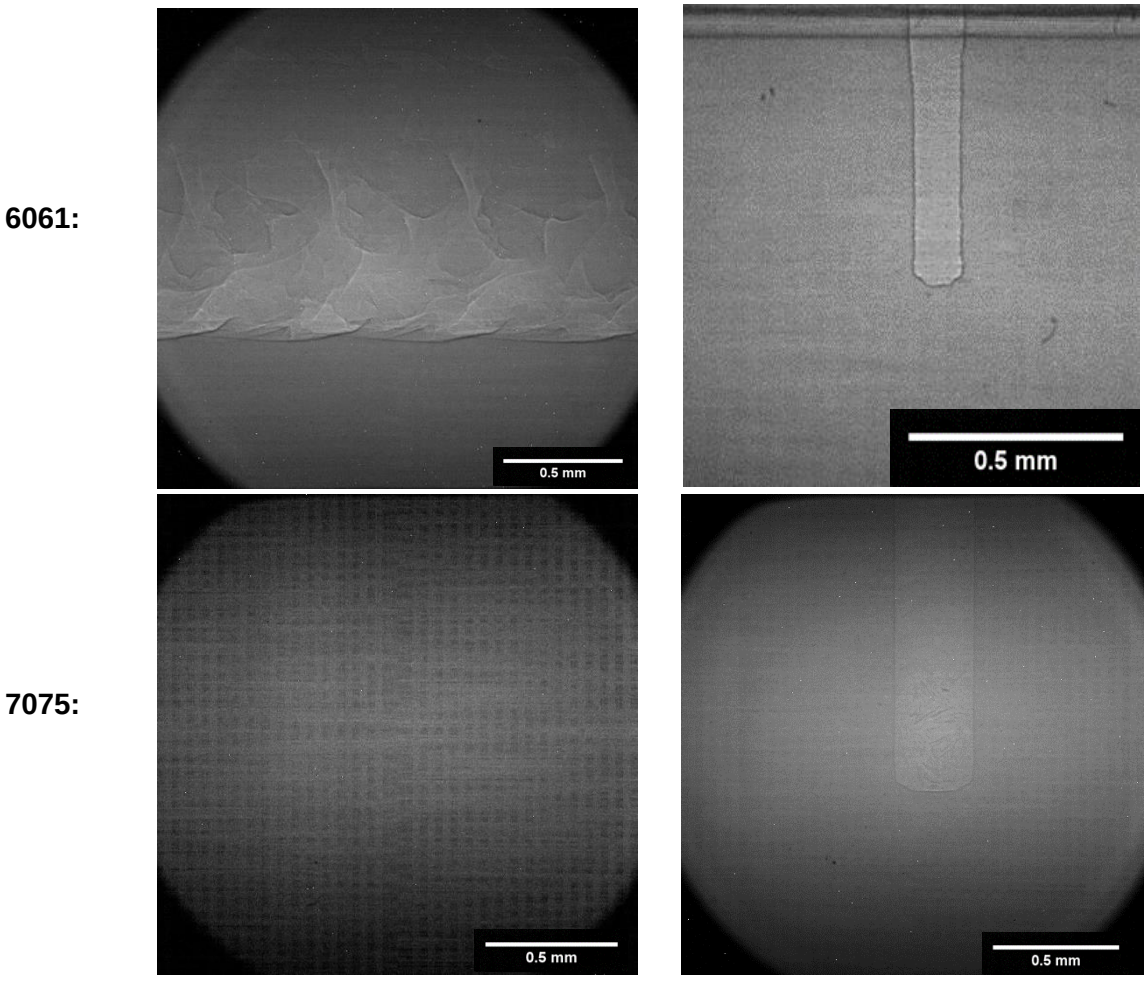

Figure 41: Selected areal density images of static samples (a) defects in 16 mm thick section of 6061 (b) 100 micrometer hole in 8.5 mm of 6061 (c) 386 micrometer hole in 16 mm of 7075 (d) 386 micrometer hole in 12 mm of 7075.

The intensity value of the pixels in the captured images is resultant of the amount of transmission. A higher pixel intensity in the image means more transmission was achieved and

less material is present. This means that the pixel intensity value can be used to provide a quantification of features in the transmission direction if the pixel intensity values of the features during welding are compared to intensity values of known features in the same thickness and with the same beam settings. Figure 42 shows the pixel intensity values of a line scan around a 386 micrometer hole in a 12 mm section of 6061. The pixel intensity value captures the density variation across the width of the holes, resulting in a curve of pixel intensities. The fact that the imaging system can differentiate the transmission through a hole on the order of 0.386 mm means that it should be capable of illustrating the nature of how a defect forms in the transmission direction when the defect is expected to be on the order of 1-2 mm in its final state.

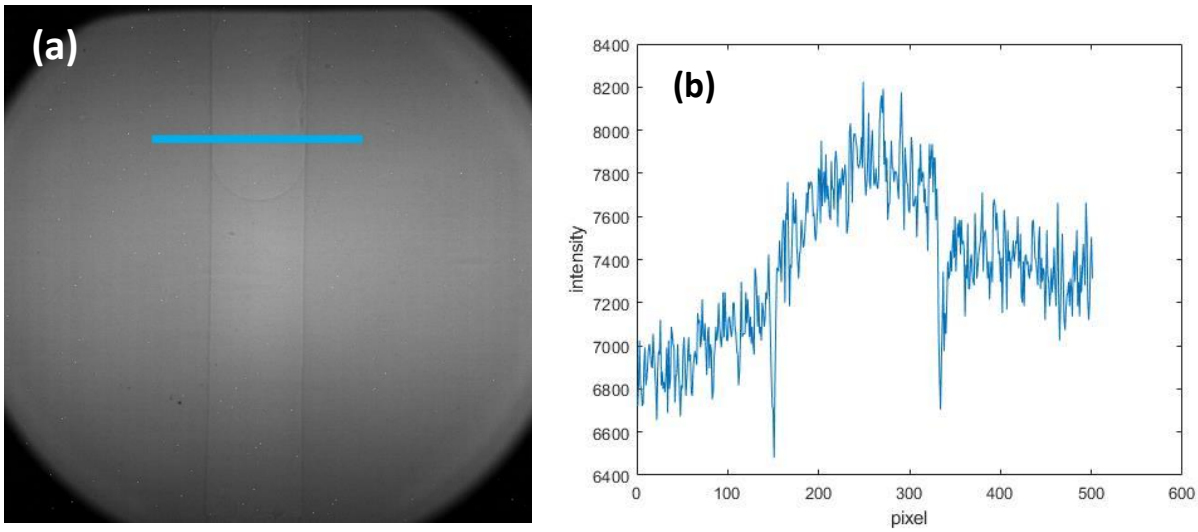

Figure 42: Example of pixel intensity across a hole: (a) areal density image of 386 micrometer hole in 12 mm thick section of 6061 with line across hole where pixel intensity values were extracted, and (b) the plot of pixel intensity values across the line scan drawn in (a).

4.2 Stop Action Welding Sample and Stainless Steel Tracer Particles

A specific weld was performed in an 8.5 mm thick section of aluminum where the tool was stopped mid-weld by pressing the emergency stop button on the machine used for welding. The tool and process will be frozen in a condition similar to what is occurring at that point in time in the weld. The stopping action cannot happen instantaneously, so the tool may rotate slightly more than its instantaneous angular position. The areal density image at the trailing edge of the

shoulder is shown in Figure 43. The weld was performed at a three-degree travel angle, and interestingly it appears that the trailing shoulder forges the material down into the defective volume after it has formed in the wake of the tool probe. In other words, the defect is larger when it interacts with the probe and is reduced to a smaller size in its final state. This concept reveals an important aspect of the process as it pertains to using methods of defect detection that sense how big the defect is at the probe but cannot describe how much the forging action of the shoulder changes the size of the defect. This phenomenon will be studied further in dynamic tests. Additionally, it can be observed that no transmission was possible through the H13 tool steel tool (it becomes a shadow with low to no pixel intensity). This means that to image phenomena in front of or behind the tool, the beam must be angle around the flats on the tool probe. Successful static images of 16 mm thick sections were achieved at up to 45 degrees with relation to beam transmission, resulting in a total average transmission length of 22.6 mm. This will allow the beam to image around the tool to capture the features as they form on the advancing and retreating sides of the process during dynamic images.

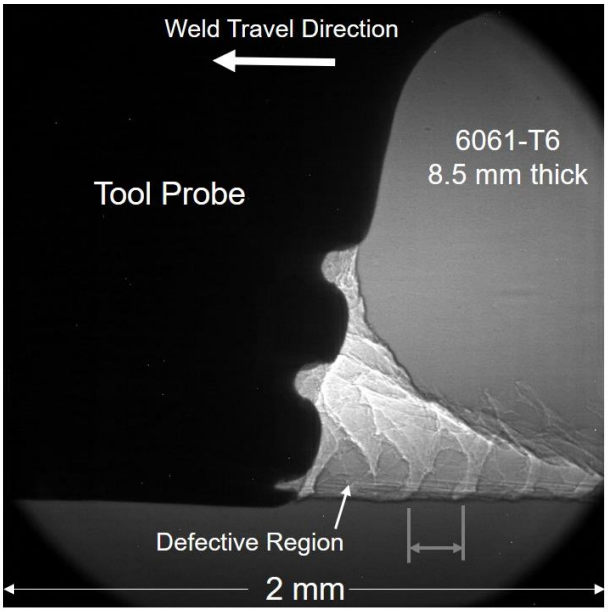

Figure 43: Areal density image of the stop action welding test

Shown in Figure 44 is the resultant areal density image of a sample of aluminum 356 that was cast with stainless steel atomized powder suspended in it. The stainless-steel powder (ranging in diameters from 45 to 100 micrometers) was stirred into the molten aluminum which was then poured into a mold. The cast part was then machined to a final shape consisting of a width in the transmission direction of 12 mm. The areal density image clearly shows the darker steel particles. These particles can be used as tracer material during dynamic tests and the distance they move between image frames and the time between images frames can be used to calculate the velocity of the material during welding. Future production of tracer material samples will utilize friction stir processing to stir stainless steel and tungsten tracer particles into aluminum workpieces.

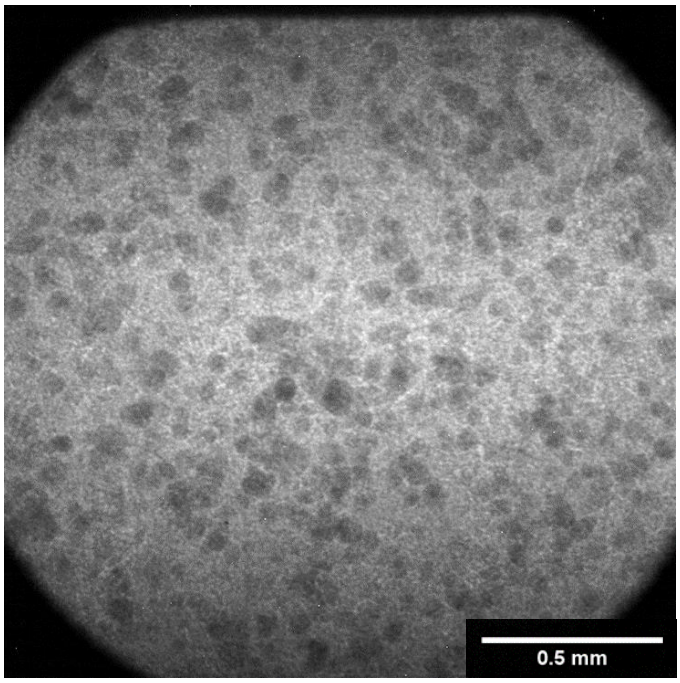

Figure 44: Areal density image of stainless steel atomized powder (dark circles) suspended in aluminum 356. Processing of the composite material during dynamic imaging provides the opportunity of using the particles as tracer material.

4.3 Development of Dynamic Imaging Apparatus and Text Matrix

Significant progress has been made towards the realization of dynamic void imaging. In order to image the friction stir welding process, the process must occur at the beam height relative

to the hutch floor which is 55 inches. The machine (HAAS TM-1 Toolroom Mill) that will be used to perform the process has a table to floor height of 33 inches. Therefore, a custom fixture (Figure 45) was designed and built to allow the thin samples to be held vertically 15 in above the mill table. The samples (one pictured in Figure 45) are machined down to their final desired thickness (8.5, 12, and 16 mm) from a standard extruded piece of aluminum that is 3/4 of an inch by 1-1/2 inches. In order to get the sample to the final beam height, a platform (Figure 46) has been designed to hold the machine eight inches above the ground so that the beam will be at the correct height to penetrate the sample. The platform is adjustable so that the machine can be moved back and forth perpendicular to the beam so that the beam can be positioned at the trailing edge of the tool. The sliding action occurs between the large square tubes that form the bulk of the platform and the bottom-most plate that rests on the floor. The linear motion is actuated by tuning bolts within a threaded nut that is fixtured to the bottom plate. The TM-1's feet are already adjustable in the vertical direction allowing the height of the sample to be adjusted precisely in the vertical direction. The platform is designed so that the machine can be jacked upward in the center using a pallet jack, the two halves of the platform will be brought underneath, the machine will be lowered, and finally, the two halves will be bolted together. The machine will be controlled remotely from the hutch control room physical switches that will be wired in around the "Cycle Start" (wired in parallel) and "E-stop" (wired in series) buttons, both of which are switches that open and close 12V logic loops.

Figure 45: Image of the custom workpiece fixture used for samples that will be imaged via the X-ray beamline

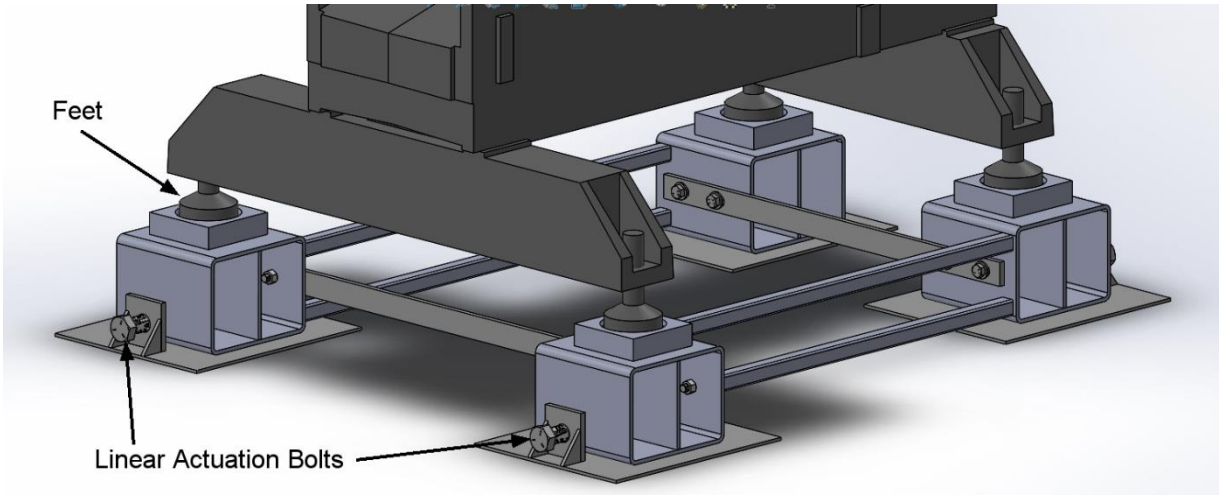

Figure 46: Illustration of the platformed designed to hold the machine at the beam height and allow for precise positioning of the machine relative to the beam

Three different sized friction stir welding tools have been manufactured in order to perform the process within the three thicknesses of interest. Each tool is designed to be the maximum diameter that is capable of performing the process within the desired thickness without causing the material at the side of the section to expand. For the 16 mm thick sample, an 11.5 mm diameter shoulder tool can be fully contained, for the 12 mm thick samples a 9 mm shoulder tool; and for the 8.5 mm samples a 6.5 mm diameter shoulder tool. Preliminary testing

within each thickness sample was performed in order to determine the parameter space in which fully consolidated and void containing welds are produced. Table 5 lists the welding parameters needed to perform successful welds in three types of welding conditions: (1) a full-contact condition with no interaction, (2) a condition with void interaction that becomes fully consolidated due to the forging action of the trailing shoulder, and (3) a large void containing condition. Voids appear at lower advance per revolution (APR) conditions for the smaller tool because the size of the APR relative to the tool becomes larger with a smaller tool.

Table 5: List of tool rotational speeds and advance per revolution conditions needed to produce the various welding states of interest for imaging

	Spindle Speed [rpm]	Full Contact Condition	Interaction and Consolidation	Significant Void Remains
16 mm Section	1000	0.2 APR	0.4 APR	0.7 APR
12 mm Section	1400	0.2 APR	0.4 APR	0.7 APR
8.5 mm Section	1600	0.1 APR	0.2 APR	0.6 APR

Chapter 7: Conclusions

This work has provided a fundamental physical understanding of what occurs when a friction stir welding tool with a distinct number of flats on the tool probe interacts with a subsurface void volume. The foundation of this understanding stems from the observation that tool runout drives the oscillations in process forces that have often been observed during friction stir welding and processing. From that, it was shown that when distinct peaks (between tool flats) on the tool probe interact with void volumes there is a change in the contact pressure that results in a momentary reduction in the force that the eccentric motion of the tool applies to the workpiece. This action is accompanied by a momentary tool defection from its nominally eccentric path. The specific conclusions that can be taken away from this body of work are as follow:

- An increase in tool runout appears to help paddle material around the tool probe and limit void formation up until a critical point where excessive runout displace material from the stir zone as opposed to shearing it around the probe.
- The force amplitudes corresponding to the third harmonic of the tool rotational frequency grow in the measured X, Y, and Z directions with a positive correlation to the growth in sub-surface void size. However, the growth is more significant in the X-Y plane because the eccentric motion of the tool per revolution occurs in said plane.
- For the range of tool shoulder plunge depths studied, a void remained in the final weld once the amplitudes of the third harmonic in the X and Y directions exceed approximately 30% of the amplitude at the tool rotational frequency from a full tool/workpiece contact welding condition with no interaction. Additionally, the amplitudes of the third harmonics saturate around 70% of the amplitude in the force signals at the tool rotational frequency during a full contact welding condition with no void/tool interaction.

- Excessive tool probe eccentricity masks the generation of the amplitudes at the third harmonic. The tool motion appears to displace material from the weld nugget as opposed to shearing it around the tool. Practitioners of friction stir welding should consider the magnitude of tool runout relative to tool size.
- Forging of the voided volume by the trailing shoulder of the tool must be controlled or monitored as the force interaction only describes the condition of the void as it interacts with the probe. The plunge depth of the trailing shoulder affects the size of the final state of sub-surface voids, *i.e*., the forging action must be considered by practitioners.
- The tool side of the system can be modeled as a simple mass-spring-damper in order to investigate the relationship between process forces and tool motion. The dynamics of the tool-side of the friction stir welding system were driven by the stiffness of the system.
- The stiffness of the tool-side of the system was driven by the stiffness of the toolholders themselves, as they were more compliant than the machine spindle. This suggests that toolholder design can be utilized to change tool motion during void interaction.
- Process damping had a minimal effect on the motion transients examined. It is hypothesized that this is due to the natural frequencies of the tool-side systems being substantially larger than the frequency of the void interactions, which was set by the number of features on the tool probe and the rotational rate.
- A 3D multiphysics numerical simulation of the process could predict the complex forces and tool motions during void interaction when applying simple linear spring elements to the tool side of the process.

The fundamental knowledge gained will form the underlying basis of advanced void monitoring methods based on measured process forces and tool accelerations. The findings will guide how the method must adapt under changing process conditions. This will result in more robust and transferable methods of void monitoring that will expedite process adoption in high-

reliability applications by reducing the need for post-welding inspection and providing the ability for in-process corrective action. Two major hurdles must be overcome in order to reach the industrial application of a void monitoring method based on process transients observed in this work. First, the measurement system must be developed for industrial application, and second, the process must be brought into real-time. This work has provided a strong base for a commercially available accelerometer instrumented toolholder (see Chapter 8: Future Work) to be used in a monitoring method. If the commercially available toolholder can capture the interactions of interest, it will help move this entire concept towards industrial application. The knowledge gained has also informed advanced numerical simulation of the void formation process in friction stir welding of aluminum alloys. This was highlighted by the successful numerical simulation of the process transients measured. Numerical simulation of the void formation process holds great potential to help expedite the design of the friction stir welding process for void/defect avoidance. This is because numerical simulation does not require the resources needed to develop the process through trial and error. This can potentially expedite the design of the process for high volume production (high travel speed) where subsurface void formation can become problematic.

Chapter 8: Future Work

8.1 Dynamic Imaging at Argonne's Advanced Photon Source

The feasibility of imaging cavities with lengths in the transmission direction on the same order of magnitude as evolving defects within the thicknesses of workpiece material of interest has been proved through static imaging (Chapter 6). The next step is to perform dynamic X-ray imaging of the evolving defects in real-time. This will be accomplished by positioning a HAAS TM-1 milling machine within beamline 32ID-B at Argonne National Laboratory's APS. Measurements have been performed confirming that a TM-1 can physically be moved into the experimental hutch on beamline 32 ID-B. In order to move the machine back into its storage area and the hutch access point, the sheet metal enclosure and X-axis motor must be removed and reassembled. Additionally, on-site electricians at the APS have determined that it is possible to install the requisite electrical power to both the storage location and inside the hutch. The electricians were in the process of preparing a quote to perform such work prior to the current shutdown of the APS due to the COVID-19 pandemic.

Dynamic imaging will be performed for welds within samples of thicknesses of 8.5, 12, and 16 mm for aluminum 6061. Alloy dependence will be studied in 6061, 3003, 7075 at a thickness of 12 mm. The 12 mm thickness is necessary for 7075 because imaging is not feasible in a 16 mm section for this alloy. FS tools of different sizes have been manufactured for each size sample. This will allow for an examination of how changing the process size alters the defect formation process. Utilizing different alloys allows for the examination of how the defect formation process changes from alloy to alloy due to their different mechanical properties. The dynamic imaging will be performed in conjunction with imaging of holes of known diameters in each alloy at the given thickness at the same beam parameters. Imaging of known features will provide a step towards the quantification of the size of defects within the transmission direction. Additionally, samples will be prepared by friction stir processing stainless steel powder into sections of

aluminum 6061 in order to suspend the particles within the aluminum sample. These particles (with diameters ranging from 45-100 micrometers) will be captured within the X-ray images as shown in Figure 44. The motion of the particles from one frame to the next will provide the ability to quantify the velocity of the material flow during friction stir welding. Additionally, imaging will be performed with the samples rotated 45 degrees relative to the beam in order to image around the tool probe on the advancing or retreating side of the process.

In all dynamic imaging experiments, defective and non-defective welds will be performed in order to examine the difference between the two regimes. All imaging will be performed at 20 kHz frequency, which will produce 600-1200 images per revolution depending on the tool rotational rate. Videos of the dynamic process will be generated from the images, providing insight into the subsurface defect formation at a level that has never been achieved before in the scientific community.

8.2 Void Monitoring via an Accelerometer Instrumented Toolholder

One challenge in the area of defect monitoring is developing a measurement system that can be quickly and easily applied to an industrial production system, yet still has sufficient sensitivity and response time to create a strong correlation between the measurement and defect occurrence. The proposed work seeks to significantly advance the state of the art in friction stir welding defect detection by using a measurement system that has already been designed for industrial application (currently on the market), while also providing a fundamental understanding of what is physically occurring during the process that causes a change in the process measurement. This work seeks to address these limitations by developing a monitoring method using the Schunk iTENDO™ toolholder with My Tool IT electronics, which is currently offered for purchase from Schunk (Figure 47) and have been used in end milling applications for chatter mitigation.

Figure 47: Image of Schunk iTENDO toolholder being used during a milling application (Taken From: https://schunk.com/at_en/homepage/itendo/)

The iTENDO™ line of toolholders consists of standard toolholders that are modified to contain the electronics from My Tool IT. The electronics consist of an accelerometer and a wireless data transfer system that allows acceleration measurements to be transmitted from the rotating tool to a stationary data acquisition system. If successful, this project will have a direct path towards industrial application due to the prior industrial nature of the measurement system. Additionally, the method will be rooted in the fundamental understanding of tool motion during defect interaction that has previously been studied at UW-Madison. Preliminary measurements that have been taken by means of a laser vibrometer (Chapters 4 and 5) have shown that when features on the tool probe interact with defective volumes, the tool is momentarily deflected into the defective volume. A laser vibrometer is not a practical measurement device in a production setting, which is why the instrumented toolholder will be the focus of future examinations. The fundamental understanding of the tool motion developed in Chapter 5 will guide the development of the monitoring method with the instrumented toolholder.

The research performed with the instrumented toolholder will focus on developing correlations between the amplitude in the acceleration signal at three times the tool rotational

frequency and the size of the voids. While developing this correlation the following process parameters will be investigated in terms of how they alter the acceleration response during void interaction:

1. The effect of the magnitude of tool runout on the acceleration signal
2. The effect of flat depth on the acceleration signal
3. The effect of tool plunge depth on the acceleration signal
4. The effect of aluminum alloy type on the acceleration signal

Preliminary testing in terms of process force measurements have been performed in all of the listed areas except for the flat depth case. The work contained in this dissertation will inform the development of the correlation between measured tool acceleration and void size when utilizing the accelerometer instrumented toolholder.

8.3 Modeling Pressure Field Around Tool Probe

Preliminary testing in various aluminum alloys has shown that harder and stronger aluminum alloys generate more distinct force distortions during void interactions [37]. It has been hypothesized that the harder stronger alloys generate a large pressure field around the tool, and therefore a larger change in pressure occurs during void interaction. This hypothesis is based on the fact that the harder and stronger alloys produce larger average process forces. A simple model was derived in which the pressure field around the probe was estimated as the average force in the X-direction over the projected area of the probe (in the x-Direction). Subsequently, an interaction area was estimated as the drop in force (amplitude of third harmonic) divided by the pressure field. The modeled interaction area was then compared to measured void areas from corresponding cross-sections of the welds from which the force data was used in the pressure model. This comparison is shown for three different alloys in Figure 48. The red line is the 1:1 ratio that would represent a perfect match between model and measured. The fact that modeled areas in Figure 48 are larger than the measured areas in the final weld cross-section can be

explained by the forging action of the trailing shoulder discussed in Chapter 4. It is hypothesized that more forging occurs in 6061 which is why the modeled values would have to be reduced more to reach the 1:1 ratio line. Overall, a positive trend is observed when comparing 7075-T6 to 3003-H14 in terms of model agreement relative to the 1:1 ratio line. This area of research is critical to understanding the relationship between the void size and the momentary drop in pressure (force distortion) during void interaction. Future research should focus on a better method of estimating the pressure field around the tool probe in order to better model the interaction (void) area. This might be best suited to be examined numerically. Additionally, the forging action of the trailing shoulder must be compensated for in order to compare to a final void size in a cross-section, or the modeled area could be compared to the real-time image of the void size while it is interacting with the tool probe once the X-ray imaging has been performed.

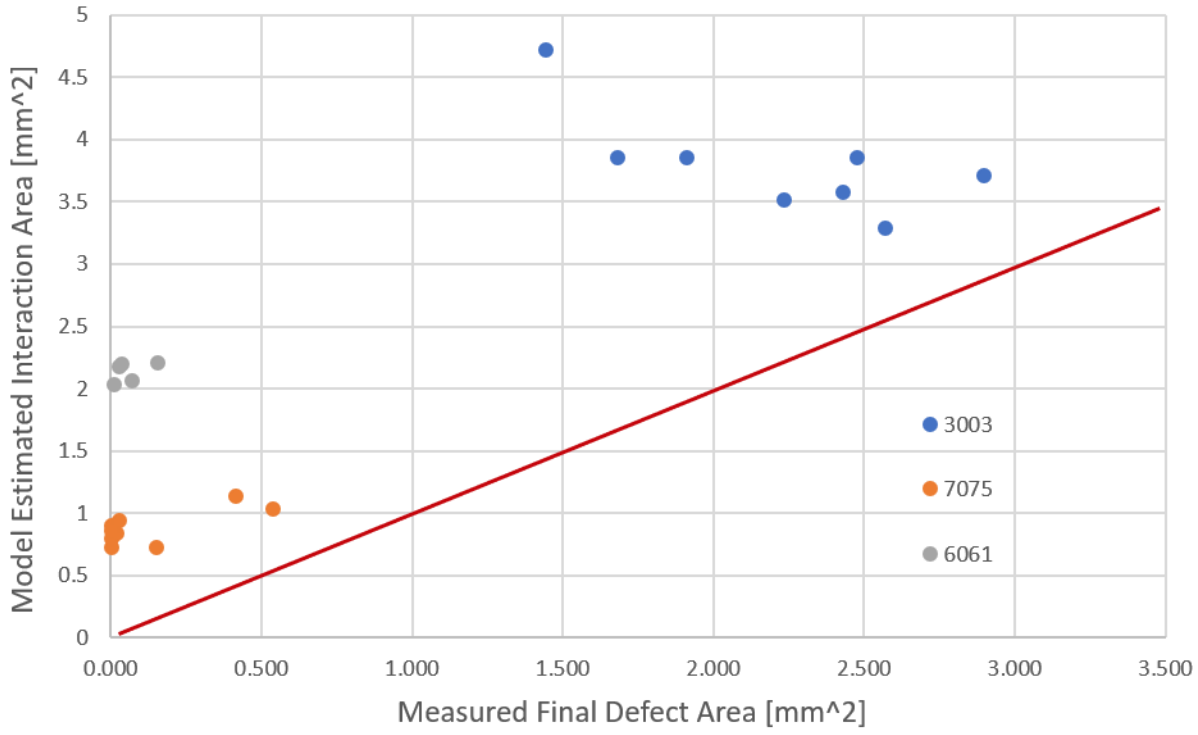

Figure 48: Comparison of an estimated void interaction area based on a simple pressure model and the measured final void area from the cross sections of the corresponding welds. Note that the red line represents a 1:1 ratio that signifies perfect agreement between modeled and measured.

References

[1] Thomas WM, Nicholas ED, Needham JC, Murch MG, Temple-Smith P, Dawes CJ. Friction Stir ButtWelding, 1991. GB Patent No. 9125978.8.

[2] Mishra RS, Ma ZY. Friction Stir Welding and Processing. Mater. Sci. Eng:R:Reports 2005:50:1-78. https://doi.org/10.1016/j.mser.2005.07.001

[3] Threadgill PL, Leonard AJ, Shercliff HR, Withers PJ. Friction Stir Welding of Aluminium Alloys. Int. Mat. Rev. 2009:54:49-93. https://doi.org/10.1179/174328009X411136

[4] Tabatabaeipour M, Hettler J, Delrue S, Van Den Abeele K. Nondestructive Ultrasonic Inspection of Friction Stir Welds. Physics Procedia 2015;70:660-663. https://doi.org/10.1016/j.phpro.2015.08.071

[5] Bird CR. Ultrasonic phased array inspection technology for the evaluation of friction stir welds. Insight - Non-Destructive Testing and Condition Monitoring 2004; 46(6):31-36. https://doi.org/10.1784/insi.46.1.31.52658

[6] Rosado LS, Santos TG, Piedade M, Ramos PM, Vilac AP. Advanced technique for non-destructive testing of friction stir welding of metals. Measurement 2010; 43:1021–30. https://doi.org/10.1016/j.measurement.2010.02.006

[7] Mandache C, Dubourg L, Merati A, Jahazi M. Pulsed Eddy Current Testing of Friction Stir Welds. Materials Evaluation 2008; 66(4): 382-386.

[8] Qian JW, Li JL, Xiong JT, Zhang FS, Li WY, Lin X. Periodic variation of torque and its relations to interfacial sticking and slipping during friction stir welding. Sci Technol Weld Join 2012; 17(4):338–341. https://doi.org/10.1179/1362171812Y.0000000001

[9] Schmidt H, Dickerson TL, Hattel JH. Material flow in butt friction stir welds in AA2024-T3, Acta Materialia 2006; 54:1199–1209. https://doi.org/10.1016/j.actamat.2005.10.052

[10] Abergast WJ. A flow-partitioned deformation zone model for defect formation during friction stir welding, Scripta Materialia 2008; 58:372–376. https://doi.org/10.1016/j.scriptamat.2007.10.031

[11] Boldsaikhan E, Burford DA, Gimenez Britos PJ. Effect of Plasticized Material Flow on the Tool Feedback Forces during Friction Stir Welding, In:Mishra R, Murray M, Sato Y, Hovanski Y, Verma R, editors. Friction Stir Welding and Proceesing VI, Wiley; 2011, p. 335-343.

[12] Nunes AC. Metal Flow in Friction Stir Welding, Materials Science & Technology 2006 Conference and Exhibition, October 15-19, 2006, Cincinnati, Ohio, USA

[13] Fonda R, Reynolds AP, Feng CR, Knipling K, Rowenhorst D. Material Flow in Friction Stir Welds, Metallurgical and Materials Transactions A 2013; 44:337-344. https://doi.org/10.1007/s11661-012-1460-6

[14] Gratecap F, Girard M, Marya S, Racineux G. Exploring material flow in Friction stir welding: tool eccentricity and formation of banded stuctures. Int J Mater Form 2012; 5:99–107. https://doi.org/10.1007/s12289-010-1008-5

[15] Reynolds AP. Flow visualization and simulation in FSW, Scripta Materialia 2008; 58:338–342. https://doi.org/10.1016/j.scriptamat.2007.10.048

[16] Chen ZW, Cui S. On the forming mechanism of banded structures in aluminum alloy friction stir welds. Scripta Materialia 2008; 58:417–420. DOI:10.1016/j.scriptamat.2007.10.026

[17] Li WY, Li, JF, Zhang ZH, Gao DL, Chao YJ. Metal Flow during Friction Stir Welding of 7075-T651 Aluminum Alloy. Experimental Mechanics 2013; 53:1573–1582. DOI: 10.1007/s11340-013-9760-3

[18] Shrivastava A, Zinn MR, Duffie, NA, Ferrier NJ, Smith CB, Pfefferkorn FE. Force measurement-based discontinuity detection during friction stir welding. Journal of Manufacturing Processes 2017; 26:113–121. https://doi.org/10.1016/j.jmapro.2017.01.007

[19] Balasubramanian N, Mishra R, Krishnamurthy K. Process forces during friction stir channeling in an aluminum alloy. J Mater Process Technol 2011; 211:305–311. https://doi.org/10.1016/j.jmatprotec.2010.10.005

[20] Balasubramanian N, Gattu B, Mishra RS. Process forces during friction stir welding of aluminium alloys. Science and Technology of Welding and Joining 2009; 14(2):141-145. https://doi.org/10.1179/136217108X372540

[21] Ji L, Zuo DW, Wang M. Force response characteristics and mechanical properties of friction stir welded AA2024 sheets. Mater Sci Technol 2106; 32(18):1–7. https://doi.org/10.1080/02670836.2016.1149916

[22] Yan JH, Sutton MA, Reynolds AP. Processing and banding in AA2524 and AA2024 friction stir welding. Science and Technology of Welding and Joining 2007; 12(5): 390-401. DOI: 10.1179/174329307X213639

[23] Boldsaikhan E, McCoy M. Analysis of tool feedback forces And material flow during friction stir welding. In: Mishra R,Mahoney MW, Sato Y, Hovanski Y, Verma R, editors. Friction stir welding and proceesing VII. Wiley, New Jersey;Wiley; 2013, p. 311–320.

[24] Zaeh MF, Gebhard P. Dynamical behaviour of machine tools during friction stir welding. Prod. Eng. Res. Devel. 2010; 4:615–624. DOI: 10.1007/s11740-010-0273-y

[25] Panzer F, Werz M, Welhe S. Experimental investigation of the friction stir welding dynamics of 6000 series aluminum alloys. Production Engineering 2018; 12:667–677. https://doi.org/10.1007/s11740-018-0834-z

[26] Mishra D, Roy RB, Dutta S, Pal SK, Chakravarty D. A review on sensor based monitoring and control of friction stir welding process and a roadmap to Industry 4.0. Journal of Manufacturing Processes 2018; 36:373-397. https://doi.org/10.1016/j.jmapro.2018.10.016

[27] Jene T, Dobman G, Wagner G, Eifler D. Monitoring of the friction stir wleding process to describe parameter effects on joint quality. Welding in the World 2008; 52:47-53. https://doi.org/10.1007/BF03266668

[28] Fleming P, Lammlein D, Wilkes D, Fleming K, Bloodworth T, Cook G, Strauss A, DeLapp D, Lienert T, Bement M, Prater T. Inprocess gap detection in friction stir welding. Sens Rev 2008; 28(1):62–7. https://doi.org/10.1108/02602280810850044

[29] Ramulu PJ, Narayanan RG, Kailas SV, Reddy J. Internal defects and process parameter analysis during friction stir welding of Al 6061 sheets. Int J Adv Manuf Technol 2013;65:1515–28. https://doi.org/10.1007/s00170-012-4276-z

[30] Kumar U, Yadav I, Kumari S, Kumari K, Ranjan N, Kesharwani RK, et al. Defect identification in friction stir welding using discrete wavelet analysis. Adv Eng Softw 2015;85:43–50. https://doi.org/10.1016/j.advengsoft.2015.02.001

[31] Kumari S, Jain R, Kumar U, Yadav I, Ranjun N, Kumari K, et al. Defect identification in friction stir welding using continuous wavelet transform. J Intell Manuf 2016; pp 1-12. DOI:10.1007/s10845-016-1259-1

[32] Das B, Pal S, Bag S. A combined wavelet packet and Hilbert-Huang transform for defect detection and modelling of weld strength in friction stir welding process. Journal of Manufacturing Processes 2016; 22:260-268. http://dx.doi.org/10.1016/j.jmapro.2016.04.002

[33] Boldsaikhan E, Corwin EM, Logar AM, Arbegast WJ. The use of neural network and discrete Fourier transform for real-time evaluation of friction stir welding. Appl Soft Comput 2011; 11:4839–46. https://doi.org/10.1016/j.asoc.2011.06.017

[34] Shrivastava A, Pfefferkorn FE, Duffie NA, Ferrier NJ, Smith CB, Malukhin K, et al. Physics-based process model approach for detecting discontinuity during friction stir welding. Int J Advanced Manuf Technol 2015;79:604–615. https://doi.org/10.1007/s00170-015-6868-x

[35] Rabi J, Balusamy T, Jawahar RR, Analysis of vibration signal responses on pre induced tunnel defects in friction stir welding using wavelet transform and empirical mode decomposition. Defense Technology 2019; 15:885-896. https://doi.org/10.1016/j.dt.2019.05.014

[36] Hartl R., Bachmann A, Habedank JB, Semm T, Zaeh MF, Process Monitoring in Friction Stir Welding Using Convolutional Neural Networks. Metals 2021;11:535. https://doi.org/10.3390/met11040535

[37] Franke DF, Zinn MR, Pfefferkorn FE. Intermittent Flow of Material and Force-Based Defect Detection During Friction Stir Welding of Aluminum Alloys. In: Hovanski Y, Mishra R, Sato Y, Upadhyay P, Yan D, Editors. Friction Stir Welding and Processing X. The Minerals, Metals & Materials Series. Springer, Cham; 2019, p. 149-160. https://doi.org/10.1007/978-3-030-05752-7_14

[38] Chen Y, Wang H, Ding H, Zhao J, Zhang F, Ren Z. Influence of tool pin eccentricity on microstructural evolution and mechanical properties of friction stir processed Al-5052 alloy. Materials Science & Engineering A 2019;739:272-276. https://doi.org/10.1016/j.msea.2018.10.057

[39] Shah LH, Guo S, Walbridge S, Gerlich A. Effect of tool eccentricity on the properties of friction stir welded AA6061 aluminum alloys. Manufacturing Letters;15PA:14-17. https://doi.org/10.1016/j.mfglet.2017.12.019

[40] Yuquing M, Liming K, Fencheng L, Qiang L, Chunping H, Xing L. Effect of tool pin eccentricity on microstructure and mechanical properties in friction stir welded 7075 aluminum alloy thick plate. Materials and Design 2014;62:334-343. http://dx.doi.org/10.1016/j.matdes.2014.05.038

[41] Bleicher F, Ramsauer CM, Oswald R, Leder N, Schoerghofer P, Method for determining edge chipping in milling based on tool holder vibration measurements. CIRP Annals - Manufacturing Technology 2020; 69:101-104. https://doi.org/10.1016/j.cirp.2020.04.100

[42] Ramsauer C, Bleicher F, New Method for Determining Single Cutting Edge Breakage of a Multi-tooth Milling Tool based on Acceleration Measurements of an Intrumented Tool Holder. Journal of Machine Engineering 2021; 21(1): 67–77. https://doi.org/10.36897/jme/131918

[43] Huang CY, Wang JJJ. Mechanistic Modeling of Process Damping in Peripheral Milling. Journal of Manufacturing Science and Engineering. 2007; 129(1): 12–20. DOI: 10.1115/1.2335857

[44] Budak E, Tunc LT. A New Method for Identification and Modeling of Process Damping in Machining. Journal of Manufacturing Science and Engineering. 2009; 131(5):051019. DOI: 10.1115/1.4000170

[45] Ahmadi K, Altintas Y. Identification of Machining Process Damping Using Output-Only Modal Analysis. Journal of Manufacturing Science and Engineering.2014; 136(5):051017. DOI: 10.1115/1.4027676

[46] Tunc LT, Budak E, Effect of cutting conditions and tool geometry on process damping in machining. International Journal of Machine Tools & Manufacture 2012; 57:10-19. https://doi.org/10.1016/j.ijmachtools.2012.01.009

[47] Li H, Shin YC, A Comprehensive Dynamic End Milling Simulation Model. Journal of Manufacturing Science and Engineering. 2006: 128(1): 86-95. DOI: 10.1115/1.2035694

[48] Kurata Y, Merdol, SD, Altintas Y, Suzuki N, Shamoto E, Chatter Stability in Turning and Milling with in Process Identified Process Damping. Journal of Advanced Mechanical Design Systems and Manufacturing. 2010: 4(6): 1107-1118. https://doi.org/10.1299/jamdsm.4.1107

[49] Wan M, Feng J, Ma YC, Zhang WH, Identification of milling process damping using operational modal analysis. International Journal of Machine Tools and Manufacture 2017; 122:120-131. https://doi.org/10.1016/j.ijmachtools.2017.06.006

[50] Ahmadi K, Altintas Y, Identification of Machining Process Damping Using Output-Oly Modal Analysis. Journla of Manufacturing Science and Engineering 2014; 136(5): 051017(1-13). DOI: 10.1115/1.4027676

[51] Symon K, Mechanics. Addison-Wesley, 1971. ISBN 0-201-07392-7

[52] Rabe P, Schiebahn A, Reisgen U. Force feedback-based quality monitoring of the friction stir welding process utilizing an analytic algorithm. Welding in the World 2021; 65:845-854. https://doi.org/10.1007/s40194-020-01044-5

[53] Edwards PD, Ramulu M. Material flow during friction stir welding of Ti-6Al-4V. J Mater Process Technol 2015;218:107–15.

[54] Morisada Y, Imaizumi T, Fujii H. Clarification of material flow and defect formation during friction stir welding. Sci Technol Weld Join 2015;20(2):130–7.

[55] Zhao C, Fezzaa K, Cunningham RW, Wen H, De Carlo F, Chen L, Rollett AD, Sun T. Real-time monitoring of laser powder bed fusion process using high-speed X-ray imaging and diffraction. Scientific Reports, 2017; 7;3602. https://doi.org/10.1038/s41598-017-03761-2

[56] Taheri H, Kilpatrick M, Norvalls M, Harper WJ, Koester LW, Bigelow T, Bond LJ. Investigation of Nondestructive Testing Methods for Friction Stir Welding. Metals 2019; 9(6):624. https://doi.org/10.3390/met9060624

[57] Huggett DJ, Liao TW, Wahab MA, Okeil A. Prediction of friction stir weld quality without and with signal features. The International Journal of Advanced Manufacturing Technology 2018; 95:1989–2003. https://doi.org/10.1007/s00170-017-1403-x

[58] Mishra D, Gupta A, Raj P, et al. Real time monitoring and control of friction stir welding process using multiple sensors. CIRP Journal of Manufacturing Science and Technology 2020; 30:1-11. https://doi.org/10.1016/j.cirpj.2020.03.004.

Appendices

Appendix A – Publication List

Journal Articles

Franke, D.J., S. Rudraraju, M.R. Zinn, F.E. Pfefferkorn, 2020, “Understanding process force transients with application towards defect detection during friction stir welding of aluminum alloys,” Journal of Manufacturing Processes, Vol. 54, pp. 251-261.

Franke, D.J., M.R. Zinn, S. Rudraraju, F.E. Pfefferkorn, 2021, “Influence of Tool Runout on Force Measurement during Internal Void Monitoring for Friction Stir Welding of 6061-T6 Aluminum,” Journal of Manufacturing Science and Engineering, Vol. 143(11). pp. 111008.

Franke, D.J., M.A. Ansari, M.R. Zinn, S. Rudraraju, F.E. Pfefferkorn, 2021, “Dynamic modeling of tool motion during subsurface void interaction in friction stir welding of aluminum alloys” Prepared – Submission Imminent

Franke, D.J., J.D. Morrow, M.R. Zinn, F.E. Pfefferkorn, 2017, “Solid-state infiltration of 6061-T6 aluminum alloy into carbon fibers via friction stir welding,” Journal of Manufacturing Science and Engineering, Vol. 139(11). pp. 111014 (9 pages)

Conference Proceedings

Franke, D.J., M.R. Zinn, F.E. Pfefferkorn, 2019, “Intermittent Flow of Material and Force-Based Defect Detection During Friction Stir Welding of Aluminum Alloys,” In: Hovanski Y., Mishra R., Sato Y., Upadhyay P., Yan D. (eds) Friction Stir Welding and Processing X. The Minerals, Metals & Materials Series. Springer, Cham.

Franke, D.J., M.R. Zinn, S. Rudraraju, F.E. Pfefferkorn, 2021, “Real-Time Measurement of Friction Stir Tool Motion During Defect Interaction in Aluminum 6061-T6,” In: Hovanski Y., Sato Y., Upadhyay P., Naumov A., Kumar N. (eds) Friction Stir Welding and Processing XI. The Minerals, Metals & Materials Series.

Franke, D.J., J.D. Morrow, M.R. Zinn, N.A. Duffie, F.E. Pfefferkorn, 2017, “Experimental determination of the effective viscosity of plasticized aluminum alloy 6061-T6 during friction stir welding,” Procedia Manufacturing, Vol 10. p.p. 218-231

Franke, D.J., J.D. Morrow, N.A. Duffie, M.R. Zinn, F.E. Pfefferkorn, 2016, “Towards Improved Hybrid Joining of Aluminum Alloys to Carbon Fiber Composites with Friction Stir Welding,” International Manufacturing Science and Engineering Conference. Volume 49897.

Appendix B – Supplemental Methods Description

Schematic of Force/Encoder Data Acquisition System:

A data acquisition system that measures tool angular position within the same timing scheme as process forces enabled the bulk of the analysis in this study. A schematic of the system described in the main text is shown below in Figure 1.

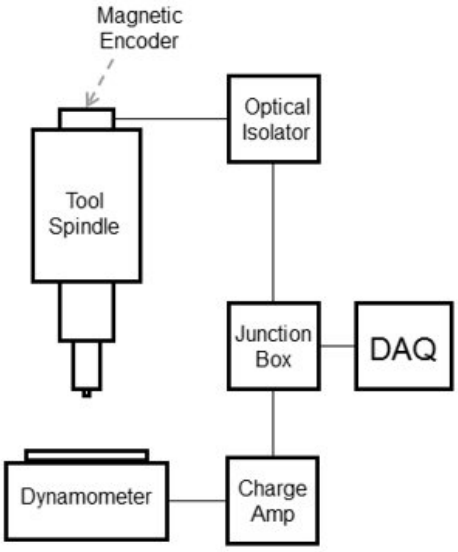

Figure 1: Schematic of full data acquisition system.

Description of Tool Holder Setup:

Figure 2 shows the friction stir tool holder configuration used on the HAAS TM-1 milling machine. The FS Tool threads into the tool holder adaptor which is held by set screws in the standard 1” CAT 40 tool holder. How the tool threads into the tool holder adaptor and how the tool holder adaptor is held by the set screws is relevant to the magnitude of tool runout and slant of the tool shoulder as described in the main text.

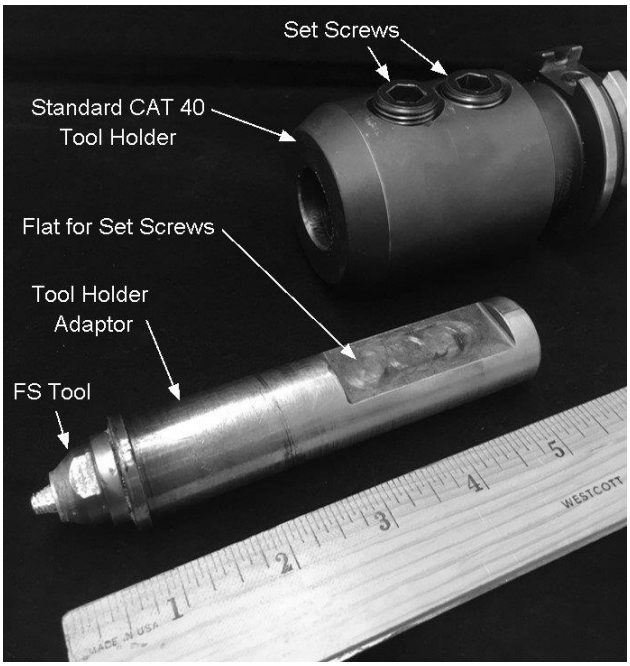

Figure 2: Tool holder apparatus

Image analysis Method for Void Area Measurements in Cross sections:

The cross-sections from all welds were ground and polished to reveal the two-dimensional nature of the voids within each cross-section. White light optical microscopy (Alicona InfiniteFocus G4, Graz, Austria) was used to produce an image of all voids from which an area value was extracted by means of a custom image analysis program written in Mathworks MATLAB (Figure 3). Black and white version of the void images were segmented using a threshold pixel value of 200. Subsequently, image cleaning was applied in order to convert any artifacts that can fit inside a 5-pixel diameter circle to the surrounding medium. A direct relationship between the number of pixels in the scale bar and the number of pixels within the void region was used to calculate the area of the void region.

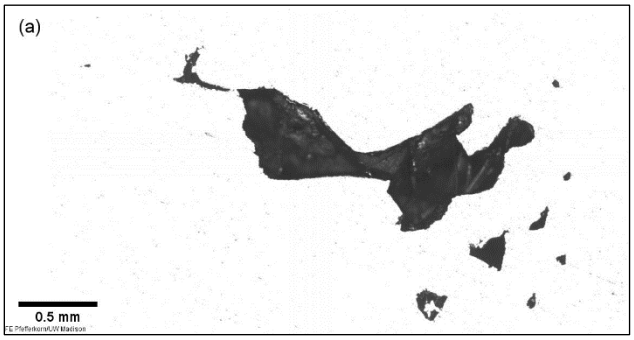

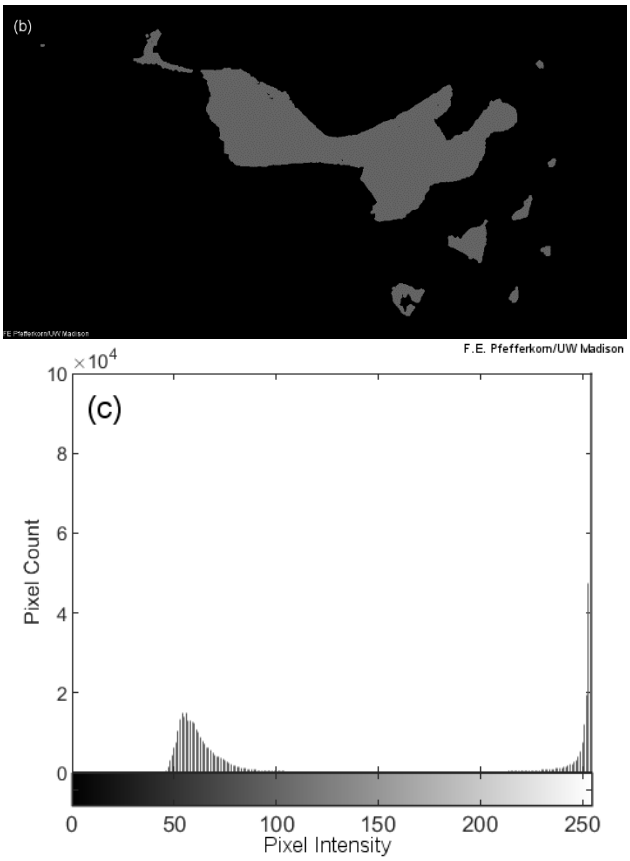

Figure 3: Depiction of Image analysis method: (a) white light image of void, (b) segmented image used for area measurement, and (c) histogram of image.

Appendix C – Equipment Data Sheets

HAAS CNC Toolroom Mill:

SPECIFICATIONS

Travels	Toolroom Mill
X	30" ,762 mm
Y	12" 305 mm
Z	16" 406 mm
Table	
Length	47.75" 1 213 mm
Width	10.5" 268 mm
T-Slots	
T-Slot Width	0.625" 15.875 mm
Number of T-Slots	3
Center Distance	4.00" 102 mm
Spindle	
Taper Size	#40 Taper
Speed	0-4,000 rpm
Transmission	Direct Speed, Belt Drive
Spindle Motor Max Rating	7.5 hp 5.6 kW
Spindle Nose to Table Top	4-20" 102 - 508 mm

Brushless Axis Motors	
Max Rating	3.0 hp 2.24 kW
Max Thrust Rating	2,000 lb 8 896 N
Feedrates	
X-Axis Rapids	200 ipm 5.1 m/min
Y-Axis Rapids	200 ipm 5.1 m/min
Z-Axis Rapids	200 ipm 5.1 m/min
Max Cutting	200 ipm 5.1 m/min
Tool Changer (Optional)	
Capacity	10
Type	CT 40
Max Tool Diameter	3.5" 89 mm
Max Tool Weight	12 lb 5.4 kg
General	
Machine Weight	3,300 lb 1 497 kg
Air Required	4 scfm, 100 psi 113 lpm, 6.9 bar
Power Required (min)	208 VAC 3-Phase 240 VAC 1-Phase
Footprint	85" x 64" 2 159 x 1 626 mm

* Base price in U.S. dollars. Prices and specifications subject to change without notice. Not responsible for typographical errors.

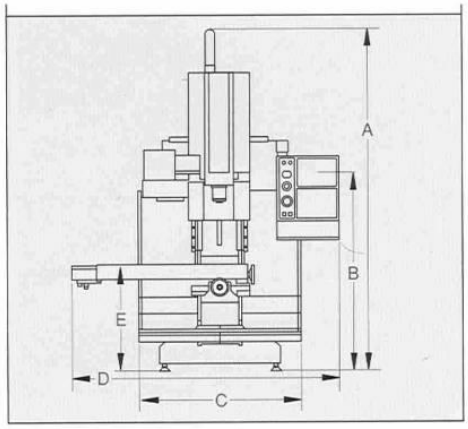

Dimensions		
A. Max Operating Height	109.0"	2 767 mm
B. Monitor Height	68.0"	1 727 mm
C. Chip Tray Width	52.0"	1 321 mm
D. Max Operating Width	84.5"	2 146 mm
E. Table Height	36.0"	914 mm

Machine depth is 64" (1 626 mm) and requires additional 35" (889 mm) to open rear service panel.

Warranty: 6 Months Parts and Labor

Kistler 9265B 3-Component Force Dynamometer:

Force – FMD

KISTLER

P.
1 ... 4

3-Komponenten-Dynamometer F_x, F_y, F_z
Dynamomètre à 3 composantes F_x, F_y, F_z
3-Component Dynamometer F_x, F_y, F_z

Type

9265B, 9441B, 9443B

Quarzkristall-Dreikomponenten-Dynamometer zum Messen der drei orthogonalen Komponenten einer Kraft. Das Dynamometer besitzt eine grosse Steifheit und demzufolge eine hohe Eigenfrequenz. Das grosse Auflösungsvermögen ermöglicht das Messen von kleinsten dynamischen Änderungen grosser Kräfte.

Dynamomètre à cristal de quartz à trois composantes pour mesurer des trois composantes orthogonales d'une force. Le dynamomètre possède une grande rigidité et par conséquent une fréquence propre élevée. Sa très haute résolution permet de mesurer les moindres variations de larges forces.

Quartz three-component dynamometer for measuring the three orthogonal components of a force. The dynamometer has a great rigidity and consequently a high natural frequency. Its high resolution enables the smallest dynamic changes in large forces to be measured.

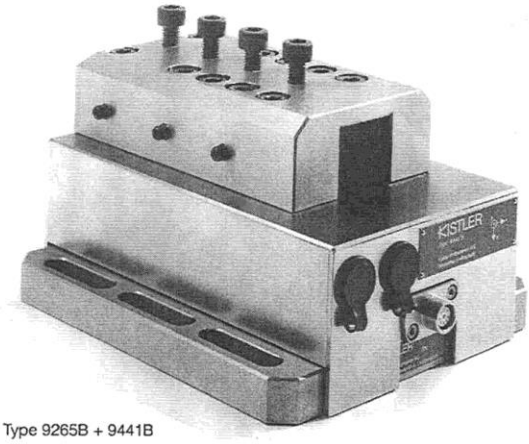

Type 9265B + 9441B

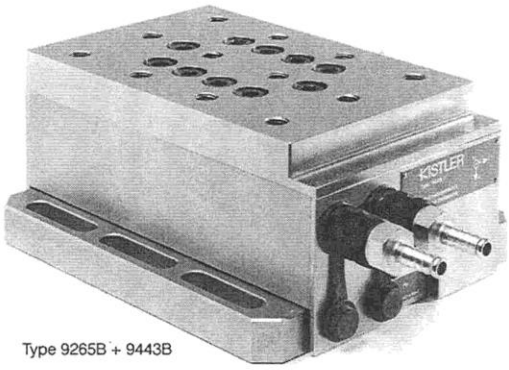

Type 9265B + 9443B

Technische Daten	Données techniques	Technical Data				
Typ	*Type*	*Type*			*9265B +9441B*	*9265B +9443B*
Bereich	**Gamme**	**Range**	F_x, F_y F_z	kN kN	–15 ... 15**) 0 ... 30**)	–15 ... 15*) –10 ... 30*)
Kalibrierter Teilbereich	**Gamme partielle étalonnée**	**Calibrated partial range**	F_x, F_y F_z	kN kN	0 ... 1,5 0 ... 3	0 ... 1,5 0 3
Überlast	**Surcharge**	**Overload**	F_x, F_y F_z	kN kN	–20/20 –12/40	–20/20 –12/40
Ansprechschwelle	**Seuil de réponse**	**Threshold**		N	<0,01	<0,01
Empfindlichkeit	**Sensibilité**	**Sensitivity**	F_x, F_y F_z	pC/N pC/N	≈–8 ≈–3,7	≈–8 ≈–3,7
Linearität, alle Bereiche **Hysterese**, alle Bereiche **Übersprechen**	**Linéarité**, toutes les gammes **Hystérésis**, toutes les gammes **Cross talk**	**Linearity**, all ranges **Hysteresis**, all ranges **Cross talk**		% FSO % FSO %	≤±0,5 ≤0,5 ≤±2	≤±0,5 ≤0,5 ≤±2***)
Steifheit	**Rigidité**	**Rigidity**	c_x, c_y c_z	kN/µm kN/µm	≈0,8 ≈2	≈1 ≈2
Eigenfrequenz (montiert an Flanschen)	**Fréquence propre** (installé sur brides)	**Natural frequency** (mounted on flanges)	f_o (x, y) f_o (z)	kHz kHz	≈1,5 ≈2,5	≈1,7 ≈2,7
Betriebstemperaturbereich **Temperaturkoeffizient** der Empfindlichkeit	**Gamme de temp. d'utilisation** **Coefficient de température** de la sensibilité	**Operating temp. range** **Temperature coefficient** of sensitivity		°C %/°C	0 ... 70 –0,02	0 ... 70 –0,02
Kapazität (pro Kanal) **Isolationswiderstand** (20 °C) **Masseisolation**	**Capacité** (de canal) **Résistance d'isolement** (20 °C) **Isolé à la masse**	**Capacitance** (of channel) **Insulation resistance** (20 °C) **Ground insulation**		pF Ω Ω	≈500 $>10^{13}$ $>10^{8}$	≈500 $>10^{13}$ $>10^{8}$
Schutzart **Gewicht**	**Classe de protection** **Poids**	**Protection class** **Weight**		– kg	IP 67****) 20	IP 67****) 19,8

*) Kraftangriff innerhalb und max. 100 mm oberhalb der Deckfläche.	*) Point d'application de la force au-dedans et max. 100 mm au-dessus de la plaque supérieure.	*) Application of force inside and max. 100 mm above top plate area.
**) Bereich beim Drehen, Kraftangriff bei Punkt A.	**) Gamme lors du tournage, point d'application au point A.	**) Range for turning, application of force at point A.
***) Kraftangriff innerhalb und max. 50 mm oberhalb der Deckfläche.	***) Point d'application de la force au-dedans et max. 50 mm au-dessus de la plaque supérieure.	***) Application of force inside and max. 50 mm above top plate area.
****) Mit Anschlusskabel Typen 1687B5, 1689B5	****) Avec câble de connexion types 1687B5, 1689B5	****) With connecting cable Types 1687B5, 1689B5

1 N (Newton) = 1 kg · m · s^{-2} = 0,1019... kp = 0,2248... lbf; 1 inch = 25,4 mm; 1 kg = 2,2046... lb; 1 Nm = 0,73756... lbft

Kistler Instrumente AG Winterthur, CH-8408 Winterthur, Switzerland, Tel. (052) 224 11 11 Kistler Instrument Corp., Amherst, NY 14228-2171, USA, Phone (716) 691-5100

Beschreibung

Das Dynamometer besteht aus einer Grundeinheit Typ 9265B, auf welche je nach Anwendung ein Stahlhalter Typ 9441B für Drehen (mit Drehwerkzeugen bis zu 32x32 mm bzw. ø32 mm) oder eine Aufspannplatte Typ 9443B für Fräsen, Schleifen usw. aufgeschraubt wird.

Die Grundeinheit besteht aus vier Dreikomponenten-Kraftsensoren, die unter hoher Vorspannung zwischen einer Grundplatte und einer Deckplatte eingebaut sind. Die Krafsensoren enthalten je drei Quarzkristall-Plattenpaare, wovon das eine auf Druck in der z-Richtung und die beiden andern auf Schub in der x- bzw. y-Richtung empfindlich sind. Die Kraftkomponenten werden praktisch weglos gemessen.

Die Ausgänge der vier eingebauten Kraftsensoren sind im Dynamometer so zusammengeschaltet, dass auch Mehrkomponenten-Kraft- und Momentmessungen möglich sind. Die acht Ausgangssignale sind an die 9-polige Flanschdose geführt.

Die vier Sensoren sind masseisoliert eingebaut. Damit werden Erdschleifenprobleme weitgehend ausgeschaltet.

Das Dynamometer ist rostbeständig und gegen das Eindringen von Spritzwasser bzw. Kühlmittel geschützt. Zusammen mit dem Anschlusskabel Typ 1687B5/1689B5 genügt das Dynamometer der Schutzklasse IP 67.

Bei der Konstruktion wurde besonderer Wert auf Unempfindlichkeit gegenüber Temperatureinflüssen beim Zerspanvorgang gelegt. Die Grundeinheit verfügt über eine anschliessbare Wasserkühlung, womit bei sehr kritischen Messungen höchste Stabilität erreicht werden kann.

Die Grundeinheit Typ 9265B wird im Werk sowohl mit dem aufgeschraubten Stahlhalter Typ 9441B wie auch mit der Aufspannplatte Typ 9443B kalibriert. Dadurch können Stahlhalter und Aufspannplatte von Anwender selbst ausgewechselt werden, ohne dass ein Neukalibrieren erforderlich ist.

Description

Le dynamomètre se compose d'un ensemble de base type 9265B sur lequel est vissé selon l'utilisation un porte-outil type 9441B pour le tournage (p.outils de tournage jusqu'à 32x32 mm resp. ø32 mm) ou une plaque de fixation type 9443B pour le fraisage, le rectifiage etc.

L'ensemble de base se compose de quatre capteurs de force à trois composantes montés sous précontrainte élevée entre une plaque de base et une plaque supérieure. Les capteurs de force comprennent chacun trois paires de plaquettes en cristal de quartz; l'une est sensible à la pression selon l'axe z alors que les deux autres sont sensibles au cisaillement selon l'axe x resp. y. Les composantes de la force sont mesurées pratiquement sans déformation.

Les sorties des quatre capteurs de force incorporés sont branchées à l'intérieur du dynamomètre de façon à rendre possible des mesures de forces et moments à plusieures composantes. Les huit signaux de sortie sont disponibles sur la prise femelle à bride et à 9 pôles.

Les quatre capteurs sont montés avec isolement par rapport à la masse. Ainsi les problèmes de circuits de retour par la terre sont largement éliminés.

Le dynamomètre est résistant à la rouille et protégé contre la pénétration de projections d'eau et d'agents refrigérants. Ensemble avec le câble type 1687B5/1689B5 il correspond à la classe de protection IP 67.

Pour la construction, l'accent a été mis en particulier sur l'insensibilité aux influences de la température lors de l'usinage. L'ensemble de base dispose d'un système de refroidissement raccordable par eau qui permet d'obtenir la stabilité la plus élevée en cas de mesures très critiques.

L'ensemble de base type 9265B est étalonné en fabrique aussi bien en fonction du porte-outil vissé type 9441B que la plaque de fixation type 9443B. Ainsi, l'utilisateur peut changer le porte-outil et la plaque de fixation sans avoir recours à un autre étalonnage.

Description

The dynamometer consists of a basic unit Type 9265B to which, depending on the application, either a tool holder Type 9441B (for turning with tools up to 32x32 mm or 32 mm dia) or a clamping plate Type 9443B for milling, grinding etc. is screwed on.

The basic unit consists of four three-component force sensors fitted under high preload between a baseplate and a top plate. Each sensor contains three pairs of quartz plates, one sensitive to pressure in the z direction and the other two responding to shear in the x and y directions respectively. The force components are measured practically without displacement.

The outputs of the four built-in force sensors are connected inside the dynamometer in a way to allow multicomponent measurements of forces and moments to be performed. The eight output signals are available at the 9-conductor flange socket.

The four sensors are mounted ground-insulated. Therefore ground loop problems are largely eliminated.

The dynamometer is rustproof and protected against penetration of splashwater and cooling agents. Together with the connecting cable Type 1687B5/1689B5 it corresponds to the protection class IP 67.

When designing the dynamometer, particular attention was given to minimizing sensitivity to temperature influences during machining. The basic unit features a connectable water cooling unit, which ensures optimal stability during very critical measurements.

The basic unit Type 9265B is calibrated at the works with both the tool holder Type 9441B and the clamping plate Type 9443B. The user can replace both the holder and the clamping plate himself without need for recalibration.

Anwendungsbeispiele

- Dynamisches und quasistatisches Messen der drei orthogonalen Komponenten einer Kraft.
- Schnittkraftmessungen beim Drehen, Fräsen, Schleifen usw. Die hohe Empfindlichkeit und die niedere Ansprechschwelle lassen in Verbindung mit den kalibrierten Teilbereichen auch exakte Messungen an kleinen Werkzeugen und beim Schleifen zu.
- Messungen an Modellen im Windkanal usw.
- Ergonomische Messungen.

Exemples d'application

- Mesures dynamiques et quasistatiques des trois composantes orthogonales d'une force.
- Mesures des efforts de coupe lors du tournage, du fraisage, du rectifiage, etc. La grande sensibilité et le seuil de réponse bas conjointement avec les games de mesure partielles etalonnées permettent des mesures exactes sur de petits outils ou lors du rectifiage.
- Mesures sur des modèles dans canaux aérodynamiques, etc.
- Mesures ergonométriques.

Application Examples

- Dynamic and quasistatic measurement of the three orthogonal components of a force.
- Measuring cutting force when turning, milling, grinding etc. In conjunction with the calibrated partial ranges the high sensitivity and low threshold allow exact measurements on small tools and when grinding.
- Measurements on wind tunnel models, etc.
- Ergonomic measurements.

000-152m-02.91 (DB06.9265Bm)

Dynamometer Typ 9265B

Abmessungen mit montiertem Stahlhalter (Drehen)

Stahlhalter Typ 9441B

Dynamomètre type 9265B

Dimensions avec porte-outil monté (tournage)

Porte-outil type 9441B

Dynamometer Type 9265B

Dimensions with mounted tool holder (turning)

Tool holder Type 9441B

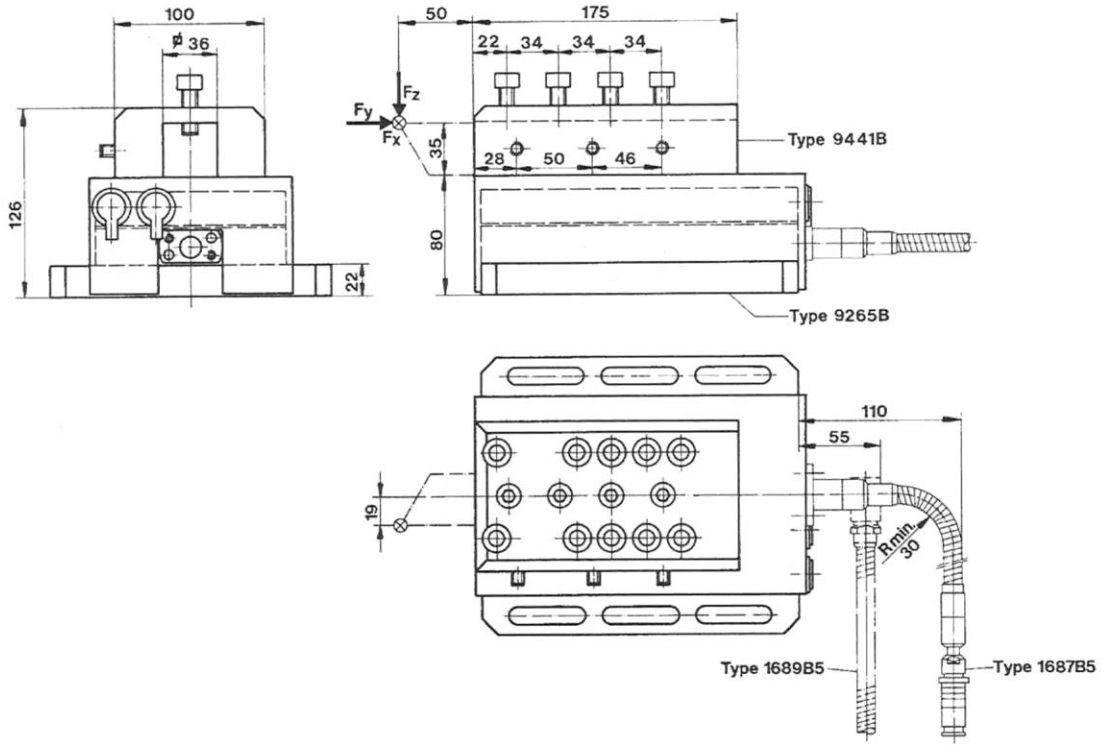

Dynamometer Typ 9265B

Abmessungen mit montierter Aufspannplatte (Fräsen, Schleifen)

Aufspannplatte Typ 9443B

Dynamomètre type 9265B

Dimensions avec plaque de fixation monté (fraisage, rectifiage)

Plaque de fixation type 9443B

Dynamometer Type 9265B

Dimensions with mounted clamping plate (milling, grinding)

Clamping plate Type 9443B

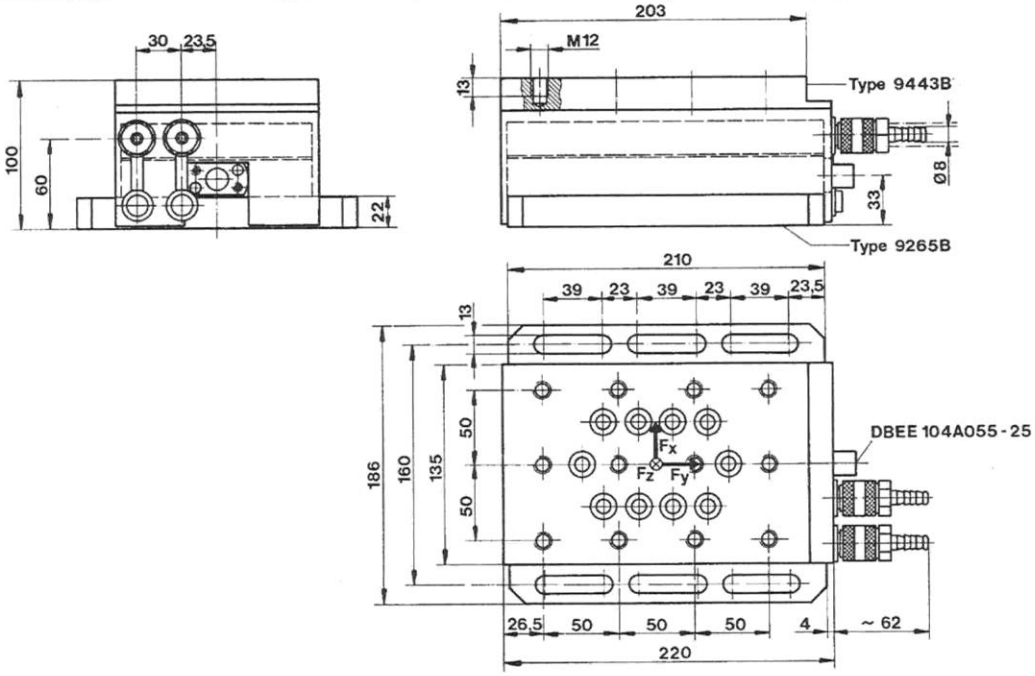

000-152m-02.91 (DB06.9265Bm)

Montage

Das Dynamometer kann mit Schrauben oder Pratzen auf jede plangeschliffene, saubere Montagefläche, wie z.B. auf einen Werkzeugmaschinentisch montiert werden. Es ist zu beachten, dass durch unebene Auflageflächen innere Verspannungen auftreten können, welche die einzelnen Messelemente zusätzlich stark belasten sowie das Übersprechen vergrössern können.

Zum Aufspannen der krafteinleitenden Teile stehen ***zwei Aufsätze*** zur Verfügung:

- Im Stahlhalter Typ 9441B können Drehstähle bis zu einem Schaftquerschnitt von 32x32 mm einwandfrei eingespannt werden.
- In der Deckplatte der Aufspannplatte Typ 9443B stehen 12 Sacklochgewinde M12 zum Aufspannen der krafteinleitenden Teile (Werkstücke) zur Verfügung.

Lieferumfang: siehe Preisliste.

Montage

Le dynamomètre peut être fixé au moyen de vis ou de brides sur toute surface plane rectifiée comme p.ex. sur un plateau de machine-outil. Toutes les inégalités ou irrégularités de la surface de montage peuvent avoir pour conséquence des tensions internes engendrant ainsi des sollicitations supplémentaires sur les divers éléments de mesure ainsi qu'un accroissement du cross talk.

Pour brider les parties introduisant la force, ***deux garnitures démontables*** sont à disposition:

- Dans le porte-outil type 9441B des outils avec une section de 32x32 mm maximum peuvent être montés sans difficulté.
- Dans la plaque supérieure de la plaque de fixation type 9443B 12 filetages M12 dans trous borgnes sont disponibles pour fixer les parties introduisant la force (pièces à usiner).

Etendu de la fourniture: voir Prix-Courant.

Mounting

The dynamometer may be mounted with screws or claws on any clean, face-ground supporting surface, such as the table of a machine tool for example. Uneven supporting surface may set up internal stresses, which will impose severe additional loads on the individual measuring elements and may also increase cross talk.

To clamp the force introducing parts, ***two detachable units*** are available:

- In the tool holder Type 9441B cutting tools with a cross-section of max. 32x32 mm can be clamped without problems.
- In the top plate of the clamping plate Type 9443B 12 blind hole threads M12 are provided to clamp the force introducing parts (workpieces).

Scope of delivery: see Price List.

Lieferformen

Die Grundeinheit Typ 9265B sowie die beiden Aufsätze (Stahlhalter Typ 9441B oder Aufspannplatte Typ 9443B) können separat bestellt und geliefert werden.

Die Grundeinheit darf jedoch ***nicht*** ohne Stahlhalter oder Aufspannplatte zum Messen eingesetzt werden.

Formes de livraison

L'unité de base type 9265B ainsi que les deux garnitures démontables (porte-outil type 9441B ou plaque de fixation type 9443B) peuvent être commandées et livrées séparément.

Toutefois, l'unité de base ne doit *pas* être utilisée pour la mesure sans porte-outil ou plaque de fixation.

Supply forms

The basic unit Type 9265B as well as the both detachable units (tool holder type 9441B or clamping plate Type 9443B) can be ordered and delivered separately.

However, the basic unit may *not* be used for measurements without tool holder or clamping plate.

Zubehör

Für 3-Komponenten-Kraftmessung F_x, F_y, F_z

• Anschlusskabel (3adrig)	Typ 1687B5 Typ 1689B5
• Verlängerungskabel (3adrig)	Typ 1688B5
• Verteilkästchen	Typ 5407A

Für 6-Komponenten-Kraft- und Momentmessung $F_x, F_y, F_z / M_x, M_y, M_z$

• Anschlusskabel (8adrig)	Typ 1677A5 Typ 1679A5
• Verlängerungskabel (8adrig)	Typ 1678A5 Typ 1678A10
• Verteilkästchen	Typ 5405A

Accessoires

Pour mesurer de forces à 3 composantes F_x, F_y, F_z

• Câble de connexion (3 fils)	type 1687B5 type 1689B5
• Câble de rallonge (3 fils)	type 1688B5
• Boîtier de distribution	type 5407A

Pour mesurer de forces et moments à 6 composantes $F_x, F_y, F_z / M_x, M_y, M_z$

• Câble de connexion (8 fils)	type 1677A5 type 1679A5
• Câble de rallonge (8 fils)	type 1678A5 type 1678A10
• Boîtier de distribution	type 5405A

Accessories

For 3-Component Force Measurements F_x, F_y, F_z

• Connecting cable (3 leads)	Type 1687B5 Type 1689B5
• Extension cable (3 leads)	Type 1688B5
• Distribution box	Type 5407A

For 6-Component Force and Moment Measurements $F_x, F_y, F_z / M_x, M_y, M_z$

• Connecting cable (8 leads)	Type 1677A5 Type 1679A5
• Extension cable (8 leads)	Type 1678A5 Type 1678A10
• Distribution box	Type 5405A

Elektronik

Eine Dreikomponenten-Kraftmessanlage benötigt neben dem Dynamometer noch drei Ladungsverstärker, welche die Ladungssignale des Dynamometers in Ausgangsspannungen umwandeln, die proportional zu den auftretenden Kräften sind.

Electronique

Outre le dynamomètre, une installation de mesure de force à trois composantes comprend encore trois amplificateurs de charge qui transforment les signaux de charge du dynamomètre en tensions de sortie proportionnelles aux forces appliquées.

Electronics

Besides the dynamometer, a three-component force measuring system also needs three charge amplifiers, which convert the dynamometer charge signals into output voltages proportional to the forces sustained.

Mehrkomponenten-Messanlagen

Weitere Einzelheiten betreffend Schnittkraft-Messanlagen

siehe Datenblatt IN6.9255/57/65.

Systèmes pour mesurer à plusieurs composantes

D'autres informations concernant des systèmes pour mesurer les efforts de coupe

voir notice technique IN6.9255/57/65.

Systems for Multicomponent Measurements

Further information concerning systems for cutting force measurements

see Data sheet IN6.9255/57/65.

000-152m-02.91 (DB06.9265Bm)

Kistler 5004 Charge Amplifier:

1.2. **Technical data** (Table 1)

1.2.1. Charge amplifier

Scale settings, 12 steps in 1 – 2 – 5 sequence				
Selectable scales, for transducer sensitivity ranges:				
0.01 to 0.11 pC or mV per M.U.	M.U./V	100	to 500,000	a)
0.1 to 1.1 pC or mV per M.U.	M.U./V	10	to 50,000	a)
1 to 11 pC or mV per M.U.	M.U./V	1	to 5,000	a)
10 to 110 pC or mV per M.U.	M.U./V	0.1	to 500	a)
0.1 to 1.1 nC or V per M.U.	M.U./V	0.01	to 50	a)
Accuracy, *Medium* time constant				
of two most sensitive ranges	%	<±5		
of all other ranges	%	<±1		
Linearity, of *Transducer Sensitivity* potentiometer	%	<±0.5		
Calibration input, sensitvity	pC/mV	1 ±0.5%		
Input voltage, absolute maximum, at *Charge input* pulse width <0.5s	V	<±125		
Amplitude linearity	%FS	<±0.05		b)
Frequency response error, *Long* time constant, short input cable				
without filter (direct connection), near DC-100 kHz	%	<±2		
with 180 kHz standard filter; near DC-100 kHz	%	<±5		
with 180 kHz standard filter; near DC-50 kHz	%	-1 to +3		
Low frequency (-5%), approx.	Hz	$\frac{0.5}{\text{Time Constant}}$		
3-dB-frequency, with standard filter 180 kHz, input capacitance up to 1500 pF (approx. 50 ft, 15 m of input cable)	kHz	180 ±10%		
Time constant resistor, setting *Long,* about	Ω	10^{14}		
setting *Medium,* about	Ω	10^{11}		
setting *Short,* about	Ω	10^{9}		
Time constant, $\tau = R_g \times C_g$ setting *Long*	s	up	to 100,000	
setting *Medium*	s	1	to 5,000	
setting *Short*	s	0.01	to 50	
Output, unlimited short circuit proof				
Voltage	V	±10		
Current	mA	±5		
Impedance	Ω	100 ±5		

Noise at the output
10 Hz to 330 kHz, 180 kHz filter, nominal, in μV_{rms}

$$\frac{\text{Input Cap. [pF]} + 50\text{pF}}{0.1 \times \text{Transd. Sens. [pC/M.U.]} \times \text{Scale [M.U./V]}} + \frac{400}{\text{Dial Setting}}$$ a)

typical value, input shielded mV_{rms} 0.1/1 c)

Capacitive input load for 1% attenuation, f< 200 Hz, in pF

$$10^4 \times \text{Scale [M.U./V]} \times \frac{\text{Transducer Sensitivity [pC/M.U.]}}{\text{Dial Setting}}$$ a)

a) M.U. = mechanical unit, e.g. psi, bar, lb, N, g
b) FS = full scale
c) Dial for transducer sensitivity adjustment set to 10-00 resp. 1-00.

DC drift, *Short* time constant			
during 10 hours	mV	<±1/±5	c)
due to line power variations ±20%	mV	<±1/±10	c)
due to temperature variations	mV/°C	<±0.5/±5	c)
Drift, due to leakage current of amplifier (input MOSFET), at 20°C	pC/s	<±0.03	
Input impedance	Ω	70	
Input cable, (coaxial, low noise) insulation resistance, approx.	Ω	10^{14}	

1.2.2. Amplifier used for Piezotron® transducers

Additional error, for *Piezotron* mode	%	<±0.5	
Noise at the output 10 Hz to 330 kHz, 180 kHz filter, nominal, in μV_{rms}		$\frac{40}{\text{Transd. Sens. [pC/M.U.] x Scale [M.U./V]}} + \frac{400}{\text{Dial Setting}}$	a)
typical value	mV_{rms}	0.1/1	c)
Power supply, constant current source	mA	4	
Input voltage range, operational	V	0 to 22	
Input voltage comparator, for LED indicator			
red (short circuit) *See color sheet for 8614A500/8616A500 use.*	V	0 to 4	
green (normal operation)	V	4 to 19	
flashing red/green (open circuit)	V	>19	
Input impedance	kΩ	>100 parallel with 1 nF	
Input cable, (ordinary two-wire or coaxial) insulation resistance	Ω	>100 k	
Capacitive input load, for 1% attenuation, in nF		$\frac{10^6}{\text{Input Signal Amplitude [}V_{pp}\text{] x Frequency [Hz]}} - 1$	

1.2.3. Monitoring circuit

Overload **indicator,** triggered by output voltage at approx.	V	±10.5	
min. Trigger signal duration for rectangular signal	ms	0.1	
Zero **out of Limits indicator,** triggered by output voltage, during *Reset,* at approx.	mV	±20	

1.2.4. Digital inputs and outputs

Connections on *Remote Control* connector on back, for functions and pin designation see 2.3. and 2.4.

a) M.U. = mechanical unit, e.g. psi, bar, lb, N, g
c) Dial for transducer sensitivity adjustment set to 10-00 resp. 1-00

Outputs, open drain, short circuit proof against electronics ground		
"H"-state, minimal output voltage with output current 0.1 mA, with external pull-up resistor 12 kΩ against +15 V (max. +18 V)	V	>12.5
"L"-state, max. output voltage with output current -10 mA	V	<1.3
Inputs, with pull-up resistors, trigger levels		
"H"-state, open inputs taken as "H"	V	>12.5
"L"-state, maximum input voltage with input current -0.8 mA	V	<1.3
protected against continuous voltage up to	V	⩽±85
peak voltages (duration ⩽0.1s) up to	V	⩽±700
Input impedance, with input voltages		
⩽±15 V, approx.	kΩ	20
>±15 V, approx.	kΩ	11
Reset-duration	ms	>5
$\overline{\text{Reset-Overload}}$ **pulse,** duration	ms	>3
+15 V output, maximum current drain	mA	12

1.2.5. General data

Operating temperature range, ambient	°C	0 to +50
Power supply	V	100 to 130
Frequency	Hz	60
Power consumption	VA	8
Connections		
Inputs	Type	BNC neg.
Output	Type	BNC neg.
Remote Control, 6-pole socket, according to DIN 45322, for plug	Model	1564
Power, 3-pole, grounded, according to IEC 320/VI, CEE-22/VI, DIN 49457/1, for cable	Model	1508
Dimensions, with case	in	2.9 W x 5.7 H x 8.3 D
	mm	74 W x 145 H x 210 D
Weight, approx.	lb	3.3
	kg	1.5
Mounting		
Case or rack, 6 units to standard 19" rack, height 5¼" (133.3 mm)		

Polytec PSV 400 Scanning Vibrometer:

PSV-400 *Scanning Vibrometer*

POLYTEC SCANNING VIBROMETERS

- **PSV-400 Scanning Vibrometer**
- PSV-400-3D Scanning Vibrometer
- PSV-400 Accessories
- MSV-400 Microscope Scanning Vibrometer
- MSA-400 Micro System Analyzer

SCANNING & VISUALIZING VIBRATIONS

The PSV-400 Scanning Vibrometer represents state-of-the-art measurement technology for the analysis of structural vibrations. Entire surfaces are rapidly scanned and automatically probed with flexible and interactively created scan grids. The PSV-400 offers technical excellence, ease of use and features designed for resolving noise and vibration issues in the automotive, aerospace, commercial manufacturing and R&D markets.

Measuring Vibrations of Complete Surfaces

Polytec Laser Doppler Vibrometers are used to precisely measure mechanical vibrations, quickly, easily and free from mass-loading or feedback problems. A modular design allows task specific optimization while retaining maximum flexibility and expandability for future needs.

Polytec Vibrometers operate on the Doppler principle, measuring the frequency shift of back-scattered laser light from a vibrating structure to determine its instantaneous velocity and displacement.

The PSV-400 Scanning Vibrometer is a single, automated, turnkey system that offers all the advantages of a laser vibrometer integrated with the speed, ease of use, accuracy and comprehensive data processing and visualization of a dual-axis laser scanner.

Key Features and Benefits

- Easy and intuitive operation and rapid, non-contact vibration measurement
- Digital data decoding available (depending on system configuration)
- Mountable Geometry Scan Unit (optional) allows acquisition of geometry data
- Measuring on imported or directly acquired object geometries or on interactively created scan grids
- Focus position of each sample point can be individually set
- MIMO (Principal Component Analysis)
- Open software platform with standardized programming and data interfaces for perfect integration in the development workflow
- Polytec Signal Processor as an integrated tool used in presentation mode
- Fully upgradeable to the PSV-400-3D 3D measuring Scanning Vibrometer

Users get a quick, easily understood and accurate visualization of a structure's global and local vibrational characteristics. The PSV-400 avoids the necessity of attaching a transducer array to the test sample and then individually collecting and processing each transducer's output.

The PSV-400 Scanning Vibrometer comprises both state-of-the-art hardware and software. It includes a compact sensor head with an integrated scanning unit, a vibrometer controller and a data acquisition and management system. These components are complimented by a powerful software package that controls the scanners, data processing, and visualization of the measurement results.

The PSV-400 series is built upon the combined strength of a proven OFV-5000 Controller and a high-performance OFV-505 Sensor Head featuring auto-focus and focus memory functionality.

The PSV-400 is designed to scan both small (mm^2) and large (m^2) structures. Depending on the chosen configuration, the PSV-400 covers vibration frequencies up to 20 MHz and vibration velocities up to 20 m/s.

The PSV-400 can be upgraded to the fully featured, PSV-400-3D Scanning Vibrometer for three-dimensional measurements. It is also the base for the award-winning Polytec Microscanning Systems.

Technical Data

General Specifications	
Working distance	> 0.4 m (shorter distances accessible by using Close-up Unit)
Laser wavelength	633 nm, visible beam
Laser protection class	Class 2 He-Ne laser, < 1 mW, eye-safe
Sample size	Several mm^2 up to m^2 range
Scan grid	Multiple grid densities and coordinate systems (polar, cartesian and hexagonal) each with up to 512 x 512 points

Configurations		
PSV-400-B	Basic Scanning Vibrometer	2 channels, 40 kHz, 10 m/s
PSV-400-H4	High End Scanning Vibrometer	4 channels, 80 KHz, 10 m/s
PSV-400-H4-S	High Amplitude Scanning Vibrometer	4 channels, 80 KHz, 20 m/s
PSV-400-M2	Wide Bandwidth Dual Channel Scanning Vibrometer	2 channels, 1 MHz, 10 m/s
PSV-400-M4	Wide Bandwidth Four Channel Scanning Vibrometer	4 channels, 1 MHz, 10 m/s
PSV-400-M2-20	20 MHz Scanning Vibrometer	2 channels, 20 MHz, 10 m/s

Accessories	
PSV-A-410 Close-up Unit	For the measurement of small parts and for measurements in close distance to model PSV-I-400 scan unit
PSV-A-420 Geometry Scan Unit	Laser-based distance sensor for the direct acquisition of 3D-geometry data
PSV-A-T18 Vertical Test Stand	For translational positioning of model PSV-I-400 scan heads
PSV-A-T11 pan/tilt head	Motorized pan/tilt head mounted on a heavy duty tripod

PSV-400 Hardware	
Sensor Head PSV-I-400	**Components:** - High sensitivity vibrometer sensor model OFV-505 - High precision scan unit (scanning range ± 20° about X, Y) Angular resolution < 0.002°, angular stability < 0.01° /hr - Color video camera with Auto Focus and 72x Zoom (4x digital, 18x optical) **Features:** - Scan speed < 50 points/s - Individual focusing of each scan point utilizing remote focus control with memory position function - Mountable Geometry Scan Unit for acquisition of test sample geometry (optional) - Working distance > 0.4 m (standard) - Weight 7.5 kg - Dimensions (L x H x W) 365 mm x 160 mm x 190 mm
Vibrometer Controller OFV-5000	- Velocity ranges (digital) general: 1/2/5/10/20/50 [mm/s/V] PSV-400-H: 0.2/0.5/1/2/5/10/20/50 [mm/s/V] PSV-400-B: not available - Velocity ranges (analog) general: 10/100/1000 [mm/s/V] PSV-400-M2-20: 10/100/500*/1000 [mm/s/V] *depending on configuration - Displacement and further velocity ranges dependent on the decoder configuration - Four analog low pass filters with limit frequency 5 kHz, 20 kHz, 100 kHz and 1.5 MHz resp. - RS-232 interface for remote control by the Data Management System
Junction Box PSV-E-400	Interface between PSV-I-400 Sensor Head, OFV-5000 Vibrometer Controller and the Data Management System - Input for 4 analog signals, triggers and gate available on BNC connectors, ICP®-compatible - Output for signal generator available on BNC connectors
Data Management System PSV-W-400	State-of-the-art rack-mountable industrial PC equipped with: - DVD-Recorder - 19" LCD Display - 100 Mb/s Ethernet network connection - Data acquisition: PSV-400-B 2 channels, 40 kHz bandwidth PSV-400-H4 4 channels, 80 kHz bandwidth PSV-400-H4-S 4 channels, 80 kHz bandwidth PSV-400-M2 2 channels, 1 MHz bandwidth PSV-400-M4 4 channels, 1 MHz bandwidth PSV-400-M2-20 2 channels, 20 MHz bandwidth - Signal generator - Operating system Windows® 2000 or Windows® XP (German, English and Japanese version available)
Systems cabinet, rollable (optional)	Houses PC Workstation, Vibrometer Controller, Junction Box and Data Management System
Motorized pan/tilt head (optional)	Maximum panning angle (horizontal): ± 90°, Maximum tilt angle (vertical): ± 84°

PSV-400 Software Features	
Scan grid definition	▪ Manual, interactive definition in the live video image by APS Professional (Advanced Point Selection), allows multiple grid densities and coordinate systems (polar, cartesian and hexagonal) each with up to 512 x 512 points combined in one scan ▪ Data import from CAD- and FEM-systems via Universal File Format (UFF) or ASCII or binary from ME'scope (optional)
Focus control	▪ Manual focussing and Autofocus ▪ Focus Scan and Focus Memory used to determine and save the optimum focus position of each respective scan point
Data acquisition	▪ Simultaneous data acquisition from up to 4 channels (vibrometer signal, 3 reference signals) ▪ Acquisition modes: FFT; zoom-FFT (optional available except for B); fast scan (optional for B); multi frame (optional, only for H); time mode (optional) ▪ Digital filtering and averaging available ▪ Trigger options: external, analog, pre and post trigger
Data quality	Continuous assessment of the S/N ratio in order to improve data quality by Signal Enhancement (increased number of samples used for averaging) and Speckle Tracking
Target data	▪ Velocity is measured; displacement (calculated by integration of velocity) and acceleration (calculated by differentiation) can also be displayed ▪ Data are saved in form of either spectra or time signal (optional for scan data) ▪ Calculation of transfer functions between primary and reference signals: FRF, H1, H2, Coherence, Autopower, Crosspower
Data presentation	Spectral presentation: ▪ Spectrum averaged over all scan points ▪ Spectra of individual points Display of video image overlaid with measured data and various presentation modes of deflection shapes: ▪ 2D: color map presentation of vibration data ▪ 3D: three-dimensional presentation of vibration data ▪ Isolines: equivalent values are interconnected by colored isolines ▪ Scan point: Each scan point is depicted as a square symbol colored according to the measured value Profile representation of section cuts across the test sample which are created interactively
Signal Processor	User interface to the math library included in the PSV software, designed as an easy-to-use spreadsheet
Data export	▪ Windows® Automation Interface: Polytec FileAccess (enables data access utilizing Visual Basic® or C++) ▪ Export of geometry data, spectra, time signals and deflection shapes as ASCII files (Microsoft Excel compatible), UFF (both standard) or ME'scope format (optional) ▪ Export of animated 2D- and 3D-models and profiles as AVI-file
Signal generation	The internal signal generator is used to create specific excitation signals

For more information, please visit our website or contact your local Polytec sales/application engineer.